Applications of Laser Wakefield Acceleration to High-Field Physics and Industrial Radiography

Christopher D. Baird

Doctor of Philosophy

University of York

Physics

November 2019

Abstract

The aim of this thesis is to investigate applications of laser wakefield acceleration to other fields of experimental physics i.e. measurement of strong-field QED effects in electrons, and industrial radiography using a laser-driven bremsstrahlung source. The importance of detector design in each of these cases is also discussed.

Chapter 4 investigates the possibility of direct, on-shot measurement of strong-field effects, namely radiation reaction, in the interaction between a high-intensity laser pulse, and an ultra-relativistic electron bunch. QED-PIC simulations of these interactions indicate that, by incorporating a pre-interaction, mm-scale drift, the signature of radiation reaction can be preserved in a localised region of an electron bunch. Consequently, unaffected regions which retain the original spectral structure can be used as a direct comparison, potentially enabling discrimination between models.

Chapter 5 reports the results of an X-ray source development project. Industrially-relevant, additively manufactured materials were imaged using a bremsstrahlung source driven by LWFA. Making use of a range of converter materials, and by having control of the plasma density in the LWFA source, it is possible to tune the resulting X-ray characteristics for different material properties. The results demonstrate the possibility that such a source, driven by a compact, high-power laser, is a commercially viable solution to industry demands for high-resolution imaging of dense materials.

Chapter 6 shows progress made in the development of caesium iodide-based X-ray detectors for various applications. Small stacks of crystals mounted to a camera, offer a compact method of detecting X-rays with high angular resolution. A large, 2D array is a useful diagnostic in detecting directional X-rays, and offers a means to recover spectral information. Extending this idea, it is possible to capture the three-dimensional structure of an X-ray beam, which may yield quantum signatures in strong-field interactions.

Contents

List of Figures

List of Tables

Declaration

I declare that this thesis is a presentation of original work and I am the sole author. Any contribution to the work by others is acknowledged in the text. This work has not previously been presented for an award at this, or any other, university. All sources are acknowledged as references.

The work presented in Chapter 4 contains work previously published by the author [1].

Acknowledgements

Despite the single name on the cover, a PhD is inevitably a collaborative effort. As such, I would be remiss if I did not acknowledge the numerous people who have given me both scientific and moral support over the last four (and a bit) years, and without whom I would not have reached this stage.

First and foremost I have to thank my supervisor, Dr. Chris Murphy. It has been a genuine pleasure to learn from you. Your knowledge, experience, and keen eye for detail have been invaluable to my development.

All the late nights and early mornings spent in laser labs have been made infinitely more enjoyable by all the talented people I've worked with. To all those at York, Imperial, QUB, and Strathclyde, thank you for making even the most disastrous experiments a great experience.

Finally, I must thank my colleagues at the Central Laser Facility, who were kind enough to offer me a job when my PhD funding ran out. Your unwavering support during the writing of this thesis has been incredible.

Role of the Author

The results in Chapter 4 are derived from simulations which were performed and analysed by the author, using computing resources at the University of York, and the SCARF cluster at the Rutherford Appleton Laboratory.

Chapter 5 details experimental results taken during a short development campaign at the Central Laser facility. The author acted as Deputy Target Area Operator, and was heavily involved in the setup and execution of the experiment. The author performed all analysis pertaining to the results presented. Monte Carlo simulations were performed by C. D. Armstrong and C. I. D. Underwood, and analysed by the author with contributions from the aforementioned.

Chapter 6 contains results from the development of X-ray diagnostics over 3 experiments at the Central Laser Facility. The compact scintillator cameras were designed and built in collaboration with C. D. Murphy and C. I. D. Underwood.

The 3D spectrometer was designed in collaboration with J. M. Cole, S. P. D. Mangles, and E. Gerstmayr.

Chapter 1

Introduction

The applications of energetic beams of electrons to scientific research are numerous. Synchrotron sources such as the Diamond Light Source, accelerate electrons to energies around $2\,\mathrm{GeV}$ to produce bright X-rays for biochemical, medical, and materials research.

The synchrotron light produced by such facilities is often the purpose, rather than a by-product. Particles in circular accelerators radiate with power $P \propto 1/m^4$ for a given energy, so electrons radiate 10^{13} more power than protons. Energy emitted is energy lost, however, and the electrons maximum attainable energy is limited by the radius of the accelerator.

We can overcome this to a large extent by using linear accelerators (linac), since longitudinal acceleration results in negligible radiation losses. Linear accelerator facilities like SLAC (now LCLS) produce some of the most energetic electron beams in the world, up to $50\,\mathrm{GeV}$, which are used to probe subatomic structure. The next iteration of linacs is the International Linear Collider (ILC), due to be constructed in Japan, is expected to reach energies of $250\,\mathrm{GeV}$ [2].

It may be apparent from figure 1.1 that the ILC is not a small facility. In fact, the proposed location for the ILC in Iwate Prefecture is an area around $32\,\mathrm{km}$ long. The reason for this is to avoid a key limitation of linear accelerators: RF breakdown. A linac can only sustain an electric field of around $150\,\mathrm{MV\,m^{-1}}$ before electrons are ripped from the cavity. To increase the energy gain, therefore, we must build ever larger accelerators. This cannot continue indefinitely, and we must eventually look to other means to reach higher energy regimes.
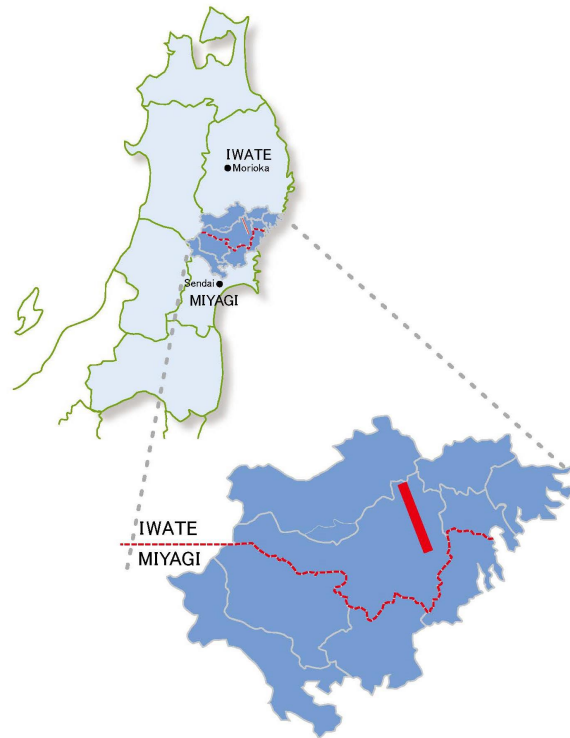
Figure 1.1: Proposed Location of the International Linear Collider in Iwate Prefecture, Japan. Source: JAHEP ILC Steering Panel 2021 Update [3]

1.1 Laser-Plasma Accelerators

A plasma can support electric fields several orders of magnitude larger than a conventional accelerator, and was suggested as an alternative acceleration medium in 1956 by Veksler [4]. The method described charged particles being used to drive oscillations in a plasma, which had sufficient amplitude to accelerate additional charged particles. This technique is referred to as 'plasma wakefield acceleration' (PWFA). A particularly striking example is that published by Blumenfeld *et al.* [5], in which electrons accelerated to $42\,\text{GeV}$ along the $3.2\,\text{km}$ linac at SLAC, were more than doubled in energy in $1\,\text{m}$ of plasma.

Instead of charged particles, the idea of using a laser to drive plasma waves (i.e. laser wakefield acceleration, or LWFA) was first reported by Tajima and Dawson in 1979 [6]. At the time, lasers capable of driving high-amplitude plasma waves were not available. However the invention of chirped pulse amplification (CPA) techniques in 1985 [7] started a revolution in laser technology which granted access to the relativistic intensities required.

Reports of laser-driven plasma waves quickly followed [8], with suggestions elec-

15

tron acceleration as early as 1986 [9]. The standard method at the time was to use copropagating laser pulses of slightly different frequencies, which produced a beatwave corresponding to the resonant frequency of the plasma [10]. Several results in the early 1990's demonstrated electron energy gain beyond 10 MeV [11–13] using this technique, referred to as 'plasma beatwave acceleration' (PBWA).

In 1993, a paper by Krall [14] described an alternative scheme using a single laser pulse. The interaction between a plasma wave and a laser pulse causes a modulation in the latter, decomposing it into a train of shorter pulses which resonantly drive the plasma wave. This 'self-modulated' (SM-LWFA) technique results in enhanced acceleration compared to PBWA [15–17], with energies reaching 94 MeV [18].

Up to this point, LWFA electron beams were broadband in energy, in contrast to the highly controlled beams produced in conventional accelerators. In 2004, however, the outlook changed with the simultaneous publication of three reports showing quasi-monoenergetic electron bunches [19–21]. These results were made possible by advances in CPA which allowed production of laser pulses on the order of 10 fs and intensities exceeding 1×10^{18} W cm^{-2}. Ultra-short, high-intensity pulses which are shorter than the plasma wavelength self-focus as they propagate. By matching the plasma density and focal spot size, this process can be precisely tuned to drive plasma waves to the point where electrons break from the wave in a short, self-terminating burst. This causes the electrons to be (almost) uniformly accelerated, resulting in low energy spread.

Since the 2004 results, there has been a huge push towards understanding the mechanisms for controlling electron beam parameters, by control of laser polarisation [22], plasma composition [23], or density tailoring [24, 25]. Naturally, the most attention-grabbing headlines are related to the maximum energy. The record currently stands at 7.8 GeV [26].

Figure 1.2 shows an aerial view of the Rutherford Appleton Laboratory, home to the Diamond Light source and the Gemini laser facility. Both of these facilities are capable of accelerating electrons to around 2 GeV, clearly demonstrating the potential for laser-driven sources as a compact means of particle acceleration.
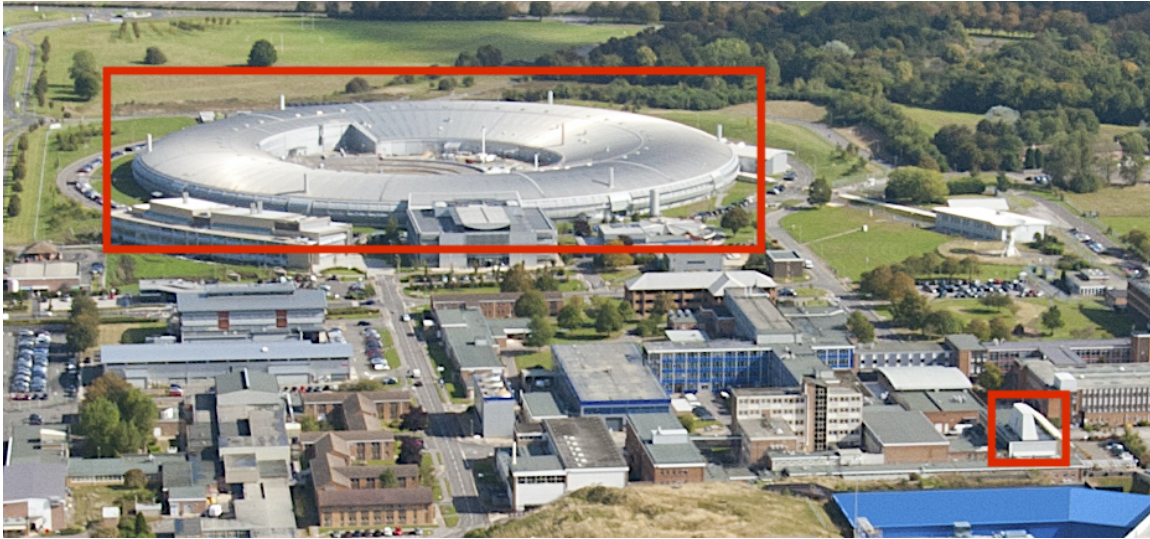
Figure 1.2: Aerial view of the Rutherford Appleton Laboratory. The Diamond Light Source (large red box) and the Gemini Laser (small) are both capable of producing 2 GeV electron beams. Source: https://www.flickr.com/photos/stfcpix/16889192337/. Licensed under Creative Commons BY-SA 2.0

1.2 Applications of Laser-Plasma Acceleration

Much of the research into laser plasma acceleration (LPA) has been focussed on understanding the mechanisms at work, but its value to the broader scientific community hinges on applying this knowledge to develop LPA into a tool for scientific research, rather than the object of it. Over the last five years, several groups have demonstrated techniques based on machine learning to automate control of particle accelerators [27, 28], and laser plasma accelerators alike [29–31].

The purpose of this thesis is to describe in detail some of the key applications of LPA, which make it a useful tool for cutting edge research. The range of possible applications is of course much more extensive than can be covered in this thesis (see figure 1.3). Interested readers should refer to the report published by the Plasma Wakefield Accelerator Steering Committee (PWASC) for a comprehensive overview [32].

Strong-Field QED Measurements

Using high-power lasers to accelerate particles allows for all-optical laser-electron collision experiments. With modern laser systems reaching intensities of $1 \times 10^{22}\,\mathrm{W\,cm^{-2}}$, it is possible to explore regimes where quantum effects dominate [33]. One such effect

17
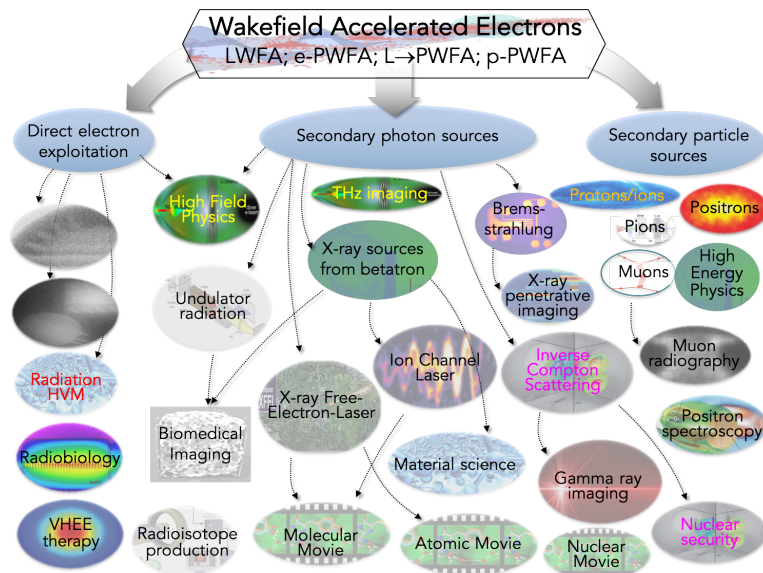
Figure 1.3: Applications of plasma acceleration. Source: [32]

is radiation reaction (RR), which is the force experienced by an electron as it radiates.

RR is a direct consequence of energy conservation, yet it eludes description by classical means. The Lorentz-Abraham-Dirac equation describes the motion of radiating charge, but it is plagued by runaway solutions and non-causal effects (see Chapter 2). Some of these undesirable characteristics can be overcome: Landau and Lifshitz [34] derived a self-consistent relativistic equation, but its validity is limited to low field strength. Others [35–37] have developed their own equations, but there is currently no consensus supporting any of them. For a particularly fiery exchange, see [38, 39].

More recent attempts to solve this problem invoke strong-field QED [40], but again there is little consensus as to the correct approach [41]. To resolve this, we turn to experiment.

The first evidence of RR effects in laser-plasma interactions was published in 2018 by Cole *et al.* and Poder *et al.* [42, 43]. They showed that RR could be measured by colliding electrons accelerated by LWFA with tightly focussed laser pulses. RR effects have also been observed in collisions between high-energy electrons produced in a linac and crystals (Wistisen *et al.* [44]). Both of these results rely on the interaction of electrons with high-intensity fields, the first from a laser, the second from nuclei. The results of Wistisen *et al.* show that linear accelerators still have an advantage over laser driven techniques, but this method is limited fundamentally by both the size of the accelerator facility, and the fixed nuclear field. An all-optical inverse Compton

approach has the potential to exceed these limits in the near future.

Hard X-ray Sources

Continuing the theme of bashing conventional particle accelerators, the development of laser-driven X-ray sources has the potential to fill a 'gap in the market' for compact, high-energy radiography facilities. In recent years, additive manufacturing has become a strong contender to replace traditional manufacturing techniques, due to reduced waste production and the ability to 'print' complex structures.

In cases where reliability of parts is paramount, e.g. aircraft, satellites, etc. the use of X-ray radiography to characterise materials is particularly beneficial. The ability to see through an object without dismantling it is critical for quality control, and enables detection of structural flaws which may be catastrophic.

X-rays can be produced in laser-plasma accelerators by several methods. Betatron radiation [45], which occurs as a result of transverse electron oscillations inside plasma waves, is typically on the order of 10 keV. Its low energy makes it useful for imaging low-density materials such as bone [46] and carbon fibre [47]. Betatron emission is also highly coherent, enabling phase-enhanced contrast imaging [48–50].

For imaging of heavier materials, i.e. metals, bremsstrahlung emission is more appropriate due to its higher energy. A laser plasma accelerator can be made into a bremsstrahlung source simply by placing a converter material such as aluminium in the path of the electron beam. The potential of such sources for radiography has been demonstrated by several groups [51–54].

Inverse Compton scattering (ICS) sources have the potential to combine the coherence of betatron with the energy of bremsstrahlung. By scattering a counter-propagating laser pulse from accelerated electrons, ultra-short X-ray pulses with MeV-scale energy can be generated [55–57]. As described above, ICS is also a useful technique for studying QED effects. One might not imagine that the areas of strong-field QED and industrial radiography intersect, but ICS sources are of relevance to both: The development of high-energy inverse Compton sources for imaging of dense materials requires understanding of the fundamental processes at work, as pair production at high-intensities will degrade the efficiency of the source [58].

Detectors

Efficient characterisation of X-rays is critical for applications. The penetrating power of a source depends on its spectral composition, and its usefulness in high-resolution radiography relies on both the size of the source and the divergence angle.

Low energy sources, such as betatron sources are relatively straightforward to characterise. Image plate, or X-ray cameras, can directly detect incident photons, and a multi-layered filter can be used to extract the spectral characteristics. For simple radiography, image plate provides high resolution and dynamic range, although it must be scanned and wiped after each shot.

For X-rays with energy above $100\,\mathrm{keV}$, detection requires a scintillator material capable of absorbing the photons. Commonly used materials are caesium iodide (CsI) and LYSO. Using arrays of scintillator crystals it is possible to characterise X-ray sources of hundreds of MeV [59, 60].

1.3 Thesis Outline

Chapter 2: Laser-Plasma Fundamentals

Key concepts relating to the results are outlined, including electron motion in electromagnetic fields, laser-wakefield acceleration, and radiation from accelerated charges.

Chapter 3: Apparatus and Methodology

Presentation of the main experimental methods and diagnostics relevant to the results. This chapter discusses electron spectrometry, interferometry, the operating principles of scintillators, and some image processing techniques for data analysis.

Chapter 4: Single-Shot Measurements of Radiation Reaction

Simulation results from EPOCH3D exploring the possibility of measuring radiation reaction effects in laser-electron collision experiments. We use a pre-interaction drift to induce a phase-space correlation between electron beam position and momentum $(x - p_x)$, which preserves the depletion zone after interaction with a laser pulse. The depletion zone is used to characterise the degree of energy loss. We find that this effect

should be measurable using currently available techniques, by careful engineering of the electron beam characteristics. Expands upon work published by the author [1].

Chapter 5: Bremsstrahlung Imaging of Industrial Materials

Application of laser-wakefield accelerated electrons to drive a bremsstrahlung source capable of imaging industrially-relevant materials. In particular we describe how the source can be tuned for different materials by modification of a few key parameters. Imaging capability using scintillators achieves detector-limited resolution of $150\,\mu\text{m}$, with $> 20\,\%$ contrast. The results presented here are based on work published by the author [61].

Chapter 6: Scintillators as High-Energy X-ray Detectors

Explores the use of caesium iodide crystals as high-energy X-ray detectors for a range of applications, including characterisation of angular distribution, spectral content of bremsstrahlung sources, and observation of quantum effects in laser-electron collisions.

Chapter 2

Laser-Plasma Fundamentals

Plasma physics is not your friend. – Anonymous

The interaction between a high-powered laser and a plasma is the foundation of an enormous body of research, spanning fields from astrophysics to quantum electrodynamics. As such, to cover the entire range of applications would be time-consuming and tedious for the reader (and the author). We must therefore restrict ourselves to the 'hot takes'. In this chapter, we will develop the theory of laser-plasma interactions as it relates to the results presented in Chapters 4, 5, and 6.

2.1   High-Power Lasers

Laser pulses can be amplified in stages to produce extremely high-energies. But non-linear effects in the gain medium will degrade the quality of the pulse, and eventually damage or destroy the medium itself. Beyond a certain intensity, Kerr lensing effectively prohibits further amplification. This is the reason for the several year plateau in laser intensity before 1985 (Figure 2.1).

The simplest solution to this problem is to reduce the intensity of the pulse by expanding it in the transverse direction, increasing the area. Unfortunately, this requires the optics and gain medium to be large enough to accommodate it. In general it is impractical to construct lasers with large optical elements.

Ultimately, the solution to this problem is to expand the pulse temporally. The frequency components of the pulse can be dispersed to produce a 'chirped pulse' of several nanoseconds. The chirped pulse is then amplified as normal, and then recompressed to
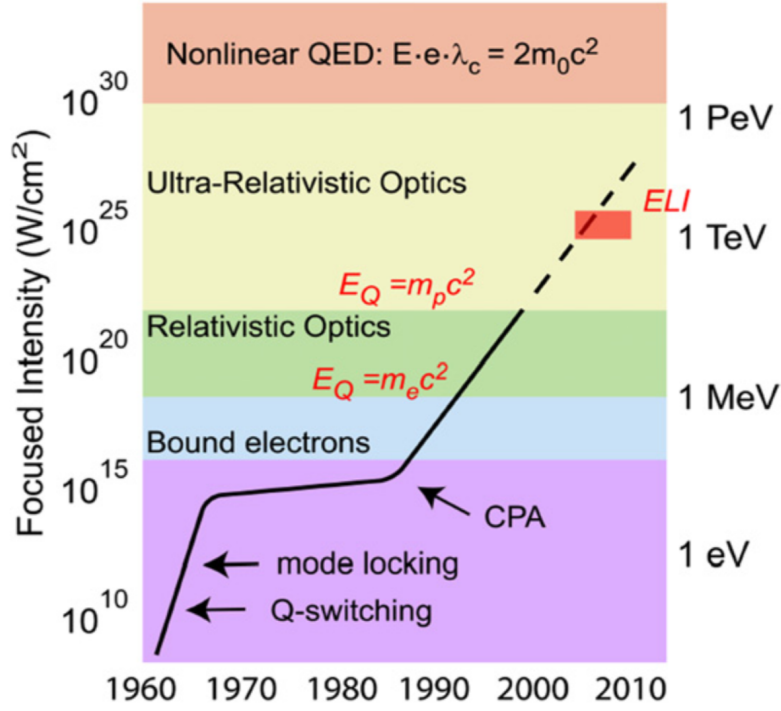
Figure 2.1: Increase in peak laser intensity since 1960. The invention of CPA enabled access to the relativistic regime. Image Source: Mourou *et al.* 2007 [62]

its original length. The advent of Chirped Pulse Amplification (CPA) [7] revolutionised laser technology and continues to facilitate the ever-increasing peak power of modern laser systems.

Figure 2.2 shows the principle of CPA. A short pulse is spatially and temporally dispersed by a pair of reflective gratings; the stretcher. The pulse may pass through the stretcher again to undo the spatial chirp, leaving only a temporal chirp.

After amplification, the pulse is compressed by a complementary pair of gratings; the compressor. The final result is an amplified, short pulse[1].

2.2 Charged Particle Motion in Laser Fields

For a charged particle of mass m and charge e in a field described by 4-potential A_μ, the action S is given by the integral [34],

$$S = \int -\frac{mc^2}{\gamma} - \frac{e}{c}A_\mu dx^\mu.,\tag{2.1}$$

---

[1] As well as undamaged optics and a greatly reduced burden on the taxpayer.

23
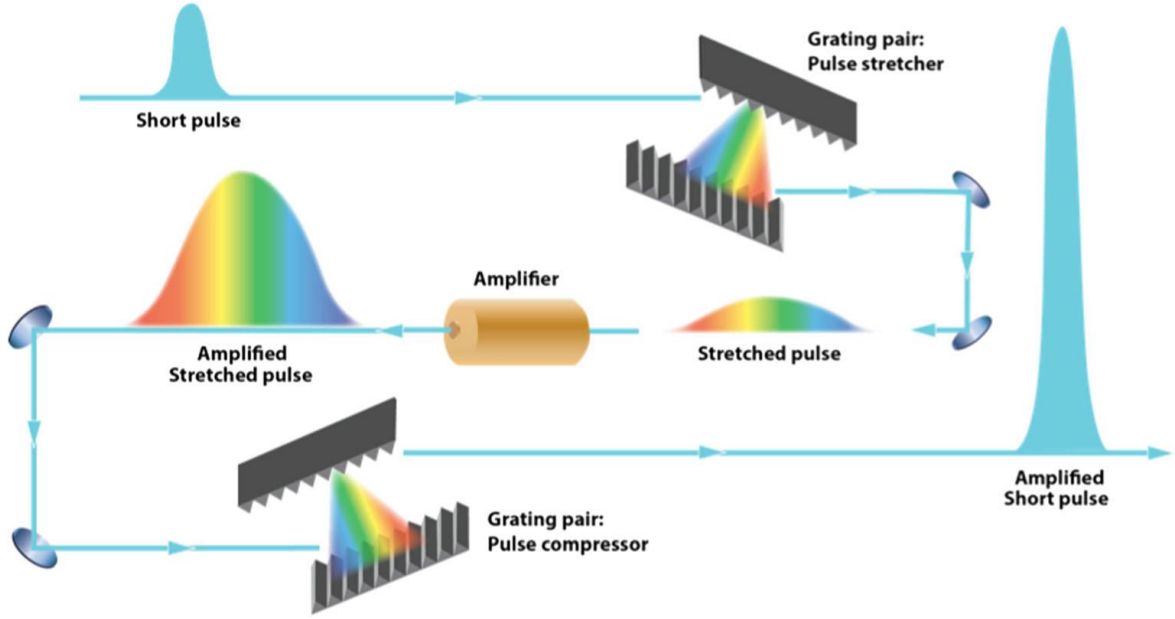
Figure 2.2: Principle of chirped pulse amplification. Image Source: Asplund *et al.* [63].

where

$$A^\mu = (\phi, \ \boldsymbol{A}). \tag{2.2}$$

From this we obtain the Lagrangian,

$$L = -\frac{mc^2}{\gamma} + \frac{e}{c}\boldsymbol{A} \cdot \boldsymbol{v} - e\phi. \tag{2.3}$$

Applying the Euler-Lagrange equation [64],

$$\frac{d}{dt}\left(\frac{\partial L}{\partial \boldsymbol{v}}\right) = \frac{\partial L}{\partial \boldsymbol{r}} \tag{2.4}$$

We find the equation of motion for the particle is,

$$\frac{d\boldsymbol{p}}{dt} = -\frac{e}{c}\frac{\partial \boldsymbol{A}}{\partial t} - e\nabla\phi + \frac{e}{c}\boldsymbol{v} \times \nabla \times \boldsymbol{A}. \tag{2.5}$$

Expressing (2.5) in terms of measurable quantities, we obtain the well-known Lorentz force equation,

$$\frac{d\boldsymbol{p}}{dt} = e\left(\boldsymbol{E} + \frac{\boldsymbol{v}}{c} \times \boldsymbol{B}\right) \tag{2.6}$$

where the electric field, $\boldsymbol{E}$, and magnetic field $\boldsymbol{B}$ are,

$$\boldsymbol{E} = -\frac{1}{c}\frac{\partial \boldsymbol{A}}{\partial t} - \nabla\phi;$$
$$\boldsymbol{B} = \nabla \times \boldsymbol{A}$$

(2.7)

Laser Strength Parameter

The momentum $\boldsymbol{p} = \gamma m_e \boldsymbol{v}$ of an electron in an oscillating field can be characterised by the so-called laser strength parameter a_0. Assuming an electromagnetic wave described by $\boldsymbol{A} = A_0 \sin(\phi)\,\hat{\boldsymbol{x}}$, where $\phi = (kz - \omega t)$, interacts with a single electron, the equation of motion is

$$\frac{d\boldsymbol{p}}{dt} = -\frac{e}{c}\frac{\partial \boldsymbol{A}}{\partial t}.$$

(2.8)

Note that here we assume the particle is non-relativistic, and so the v/c term can be neglected.

Differentiating $\boldsymbol{A}$ with respect to time, and integrating (2.8) to find the momentum yields,

$$\boldsymbol{p} = \frac{eA_0}{c}\sin(\phi)$$

(2.9)

We now normalise the electron momentum to $m_e c$ to find,

$$a = a_0 \sin(\phi)$$
$$a_0 = \frac{eA_0}{m_e c^2}$$

(2.10)

In an electromagnetic field with $a_0 = 1$, an initially stationary electron will be accelerated to $v \simeq c$ within a single cycle. The field is therefore described as being 'relativistically intense'. For a laser with $\lambda = 1\,\mu\text{m}$, this occurs for $I = cE^2/8\pi \gtrsim 1.4 \times 10^{18}\,\text{W}\,\text{cm}^{-2}$.

Particle Motion

From the momentum equation (2.6), and an equation for the particle energy,

$$\frac{d(\gamma mc^2)}{dt} = -e\,(\boldsymbol{v} \cdot \boldsymbol{E}),$$

(2.11)

the orbit of an electron in a linearly polarised field is found to be [65]

$$x = -a_0 \cos \phi \tag{2.12a}$$

$$y = 0 \tag{2.12b}$$

$$z = \frac{a_0^2}{4} \left[\phi + \tfrac{1}{2}\sin 2\phi \right] . \tag{2.12c}$$

We see from (2.12c) that the electron will experience a drift in the z direction. In the average rest-frame of the electron, the motion follows the well-known 'figure-of-eight' pattern, described by

$$
\begin{aligned}
x &= \frac{a_0^2}{8\gamma_0^2} \sin 2\phi \\
y &= \frac{a_0}{\gamma_0} \sin \phi
\end{aligned}
\tag{2.13}
$$

Ponderomotive Force

By expanding the total time derivative from the Lorentz force equation into its partial and convective terms,

$$\frac{d\boldsymbol{p}}{dt} = \left(\frac{\partial}{\partial t} + \boldsymbol{v} \cdot \nabla \right) \boldsymbol{p} \tag{2.14}$$

and using the vector identity [66]

$$(\boldsymbol{v} \cdot \nabla)(\gamma m \boldsymbol{v}) = \nabla \left(\gamma m c^2 \right) - v \times \left[\nabla \times (\gamma m \boldsymbol{v}) \right] \tag{2.15}$$

we can rewrite the equation of motion (2.6) as follows,

$$\frac{\partial}{\partial t}(\gamma m \boldsymbol{v}) = e \left(\nabla \phi + \frac{1}{c}\frac{\partial \boldsymbol{A}}{\partial t} - \frac{v}{c} \times \nabla \times \boldsymbol{A} \right) + \boldsymbol{v} \times \left[\nabla \times (\gamma \boldsymbol{v}) \right] - \nabla \left(\gamma c^2 \right) . \tag{2.16}$$

We then take the curl of this equation, and collect terms to obtain

$$\frac{\partial}{\partial t}\left[\nabla \times \left(\gamma m \boldsymbol{v} - \frac{e\boldsymbol{A}}{c} \right) \right] = \nabla \times \left[\boldsymbol{v} \times \left[\nabla \times \left(\gamma m \boldsymbol{v} - \frac{e\boldsymbol{A}}{c} \right) \right] \right] \tag{2.17}$$

From above, we can see that if $\Omega = \nabla \times (\gamma m \boldsymbol{v} - e\boldsymbol{A}/mc)$ is zero at some initial time, then it will remain zero for all future times. Ω may be referred to as the 'generalised vorticity' [67], by analogy with the expression in classical fluid mechanics ($\omega = \nabla \times \boldsymbol{v}$). The final expression is then,

26

$$\frac{\partial}{\partial t}\left(\gamma m \boldsymbol{v}\right) = e\left(\nabla\phi + \frac{1}{c}\frac{\partial \boldsymbol{A}}{\partial t}\right) - \nabla\left(\gamma mc^2\right), \tag{2.18}$$

where the last term on the RHS is the ponderomotive force contribution. The consequence of the result in (2.18) is clearer in the non-relativistic case. For $v \ll c$, the ponderomotive contribution becomes

$$f_{pond} = -\frac{m}{2}\nabla v^2. \tag{2.19}$$

In the case of an oscillating laser field, $E = E_0\sin\phi$, we find that

$$f_{pond} = -\frac{e^2\nabla E_0^2}{4m\omega^2}, \tag{2.20}$$

implying that the particle experiences a force away from regions of high field strength. For a Gaussian laser pulse, then, electrons are driven away from the central region. This effect is crucial in the formation of wakefields, which will be discussed later.

2.3 Plasmas

Often called the fourth state of matter, plasma is the most common observable state of matter in the universe. A plasma is characterised by its collective behavior and electromagnetic properties, which allow it to support high electric and magnetic fields.

2.3.1 Plasma Oscillations

Here we examine the response of electrons in a plasma to a small spatial displacement from equilibrium. To illustrate the general behaviour, it is sufficient to consider a 1D system where the ions are stationary on account of their larger mass.

Starting with an intially quasi-neutral plasma, we displace a 'slab' of electrons a small distance x from equilibrium. Poisson's equation then gives the potential as,

$$\phi = 2\pi en_e x^2 \tag{2.21}$$

The resulting force on the electron slab is given by the equation of motion

$$m_e \frac{d\boldsymbol{v}}{dt} = -e\nabla\phi$$
$$\frac{d^2x}{dt^2} = -\frac{4\pi e^2 n_e}{m_e}x \tag{2.22}$$

This result is a second-order ODE, corresponding to simple-harmonic motion with a characteristic frequency ω_p.

$$\ddot{x} = -\omega_p^2 x \tag{2.23}$$

Where the plasma frequency ω_p is given by,

$$\omega_p = \sqrt{\frac{4\pi n_e e^2}{m_e}} \tag{2.24}$$

This equation can be generalised for relativistic electron velocity by including the Lorentz factor γ, such that $m_e \to \gamma m_e$.

In the cold plasma approximation, the maximum amplitude of plasma oscillations is determined by the cold wave-breaking limit, as shown by Dawson [68],

$$E_0 = \frac{m\omega_p v_p}{e}. \tag{2.25}$$

Above this limit, the oscillation breaks down as 'sheets' of charge overlap. Dawson's model is non-relativistic, and must be modified for the case of relativistic plasma oscillations. Katsouleas and Mori [69] derive the relativistic wavebreaking limit, in this case for a 'warm' plasma,

$$E_{WB} = \sqrt{2\left(\gamma_p - 1\right)}E_0, \tag{2.26}$$

where γ_p is the lorentz factor of the plasma wave.

2.3.2 Electromagnetic Waves in Plasmas

Electromagnetic waves propagate in plasmas according to the dispersion relation,

$$\omega_L^2 = \omega_p^2 - k^2 c^2. \tag{2.27}$$

from which we can calculate the phase velocity[1] v_p and group velocity v_g as,

$$v_p = \frac{\omega_L}{k} = c\left(1 - \frac{\omega_p^2}{\omega_L^2}\right)^{-1/2}$$
$$v_g = \frac{\partial \omega}{\partial k} = c\left(1 - \frac{\omega_p^2}{\omega_L^2}\right)^{1/2}.$$
(2.28)

The bracketed term in (2.28) is the refractive index of the plasma,

$$\eta = \left(1 - \frac{\omega_p^2}{\omega_L^2}\right)$$
(2.29)

From the dispersion relation, it can be seen that if the laser frequency ω_L is equal to the plasma frequency, the wavenumber vanishes, i.e. the wave does not propagate in the plasma. The value of ω_L for which this occurs is associated with a plasma density n_{crit} given by

$$n_{crit} = \frac{m_e \omega_L^2}{4\pi e^2}.$$
(2.30)

This quantity is referred to as the 'critical density' and is the density for which electron oscillations in the plasma match the electric field oscillations of the incident wave, cancelling them out.

The plasma refractive index can be rewritten in terms of the critical density as follows,

$$\eta = \left(1 - \frac{n_e}{n_{crit}}\right).$$
(2.31)

It can be seen from eq. 2.28 and eq. 2.31 that the velocity of EM waves in a plasma depends on the ratio n_e/n_{crit} which will prove important for wakefield acceleration.

Self-Focussing

The density perturbations caused by plasma waves cause changes in the local refractive index. For the particular case of a laser pulse propagating through a plasma, the low density region around the pulse generates a refractive index gradient directed away from the centre of the pulse [71]. The result of this is that the laser pulse 'self-focusses' as it moves through the plasma. Matching the plasma density to the laser intensity allows the pulse to be guided for long distances through the plasma.

---

[1]Notice that the phase velocity is strictly greater than c, which precludes the emission of Cherenkov radiation in plasmas.
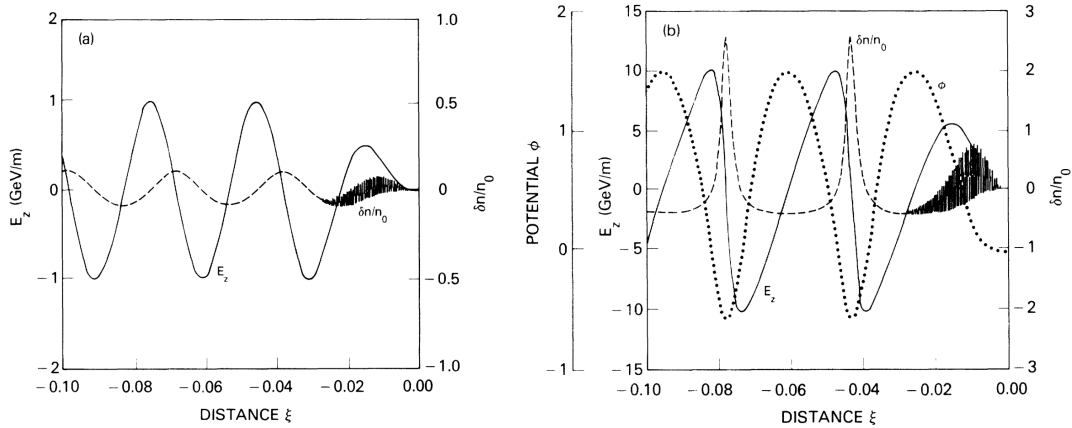
Figure 2.3: Plasma waves in the linear and non-linear regimes. Left: Electron density ($\delta n/n_0$) and electric field profile (E_z) for driving laser with $a_0 = 0.5$. Right: Density and electric field for driver $a_0 = 2$. Potential ϕ also shown. Image source: Sprangle *et al.* 1990 [70].

2.4 Laser Wakefield Acceleration

Particle acceleration by laser-driven wakefields is a product of various plasma effects described in the previous section, and is one (albeit rare) example which contradicts the pessimistic outlook portrayed by the quote at the start of this chapter. In this section we will discuss the generation of wakefields by intense lasers and the physics of electron acceleration.

2.4.1 Wake Generation

In the previous sections, we discussed several nonlinear effects which occur when lasers interact with plasmas. Under the proper conditions, these effects work synergistically to accelerate electrons to high energies, forming the basis of a laser-plasma accelerator. The process of laser-wakefield acceleration relies on the generation of electron-plasma waves, which can trap and accelerate electrons.

An intense laser pulse propagating in a plasma will tend to drive electrons away from its path due to the ponderomotive force. This creates an area of low electron density behind the pulse[1]. The electric field established by the charge separation produces a restoring force on the electrons, and causes them to oscillate at the plasma frequency.

The wave structure behind the laser pulse resembles that of a wake generated by a boat moving along a river, as seen in Figure 2.3. In the linear regime, that is where

---

[1]We assume that the much heavier ions remain stationary over the interaction time.

$\delta n / n_0 \ll 1$, the shape of the plasma wave is a sinusoid with frequency ω_p, and is described by the following expression [65],

$$\left(\frac{\partial^2}{\partial t^2} + \omega_p^2 \right) n = \frac{n_0}{2} \frac{\partial^2 a^2}{\partial x^2}. \tag{2.32}$$

By driving the wave more strongly, we increase the relative size of the density perturbation and the shape becomes more complex. The non-linear plasma wave represents a departure from the linear oscillation frequency in Section 2.3.1. The sharp peaks in electron density, shown in Figure 2.3, result in a sawtooth-shaped electric field structure, with an amplitude exceeding E_0 (Eq. 2.25).

This plasma wave propagates at the same velocity as the laser pulse (i.e. $c - v_g$), and the high electric field gradient can trap and accelerate electrons to extremely high energies. The plasma wave can sustain field gradients of over $100 \, \mathrm{GV \, m^{-1}}$, three orders of magnitude greater than that of a conventional accelerator [6].

2.4.2 Wavebreaking and Injection

Driving the wave above the wavebreaking limit, E_{WB} (eq. 2.26), will cast electrons into the low density regions in a process known as 'wavebreaking injection' or 'self-injection' [72]. As electrons break from the wave, the density peak decreases and the field drops below E_{WB}, preventing further injection. This process was exploited to produce the first reported monoenergetic electron beams [19–21].

Generating consistent electron beams via self-injection is challenging since the density perturbations depend non-linearly on the intensity of the driving laser pulse, which is subject to fluctuations. There are several techniques in use which facilitate greater control over the injection process, and allow tuning of the electron beam characteristics.

Ionisation Injection

LWFA experiments commonly use helium gas due to its low ionisation potential[1], so that the plasma will be fully ionised by the foot of the laser pulse. An alternative method is to use a gas which will not be fully ionised by the driver, and trigger further ionisation by external means. Chen *et al.* [73] describe a technique in which a wakefield

---

[1]A helium atom will be fully ionised at around $8.8 \times 10^{15} \, \mathrm{W \, cm^{-2}}$.

is driven in a partially ionised neon plasma. Injection is then stimulated by a second laser pulse of sufficient a_0 to ionise the remaining electrons. The delivery of the second beam is timed to cause injection in the positively charged region of the wakefield, maximising acceleration potential.

A similar effect can also be achieved with a single laser pulse. In plasma generated from mixed gases, e.g. helium mixed with a small fraction of nitrogen, the inner electrons of the dopant will not be liberated from the nucleus until they encounter the highest intensity region of the driving pulse [23, 74]. This effectively enables electrons to be injected directly into the accelerating region. Electron beams generated via this method are typically broadband, with the energy spread scaling with a_0, since electrons are continually injected as the pulse propagates through the plasma. This continuous injection also results in higher charge electron beams than those produced by self-injection, which can limit the acceleration potential due to beam-loading [75].

Shock Injection

Injection can be stimulated by introducing a density perturbation by way of a shock front in the plasma. This is achieved experimentally by placing a razor blade, or similar sharp objects such as cleaved crystals, into the gas. As the plasma wave passes the density ramp, the sudden change in plasma wavelength displaces trapped electrons relative to the density peaks. These electrons then find themselves in the accelerating region. Density-ramp injection, or shock-injection has been shown to produce stable, narrow bandwidth electron beams [24, 76] of up to $1\,\mathrm{GeV}$ [77].

Trojan Horse Method

Electron beams generated by LWFA can themselves drive wakefields in a process known as 'Plasma Wakefield Acceleration' (PWFA). These can be combined in a two-stage accelerator scheme known as 'Trojan Horse'. An electron bunch generated by LWFA is used to drive a wakefield in a plasma which is not fully ionised. A co-propagating laser pulse is then focussed into the accelerating region of the wake structure, ionising the remaining electrons. By using a fast-focussing pulse, the injection can be precisely timed, resulting in very low energy spread bunches with low divergence [78].

2.4.3 Energy Gain and Dephasing

Once trapped in the low density region behind the pulse, the electrons are accelerated in the longitudinal direction by the surrounding net positive charge. As they do so, they quickly approach the speed of light and begin to catch up to the driving pulse. An electron which moves a distance of $\lambda_p/2$ from the peak of the wake will experience a decelerating force and begin to 'dephase' from the wakefield. In the lab frame, the distance an electron must travel before it dephases is the 'dephasing length' and is related to the plasma and laser parameters by [79],

$$L_{dph} \sim \frac{\lambda_p^3}{\lambda_0^2} a_0 \tag{2.33}$$

The maximum energy attainable by an electron in a wakefield is given by [6]

$$W_{max} \simeq 2 m_e c^2 \frac{n_c}{n_e} \tag{2.34}$$

2.5 Radiation from Moving Charges

As a consequence of the finite speed of electromagnetic waves, a charge in accelerated motion will radiate energy according to the Larmor formula [80],

$$P = \frac{2e^2}{3c^3} \dot{v}^2 \tag{2.35}$$

where P is the radiated power of the charge. For relativistic motion, eq. (2.35) generalises to

$$P = \frac{2e^2}{3m^2c^3} \left(\frac{dp^\mu}{dt} \frac{dp_\mu}{dt} \right) \tag{2.36}$$

For a highly relativistic particle accelerated along the direction of motion, i.e. $\boldsymbol{\beta} \times \dot{\boldsymbol{\beta}} = 0$, the radiated power is given by

$$\frac{dP}{d\Omega} = \frac{e^2}{4\pi c^3} \left(\frac{dv}{dt} \right)^2 \frac{\sin^2\theta}{(1 - \beta\cos\theta)^5} \tag{2.37}$$

where θ is the angle of emission with $\theta = 0$ corresponding to the direction of motion.

A similar equation is obtained for perpendicular motion,

$$\frac{dP}{d\Omega} = \frac{e^2}{4\pi c^3} \left(\frac{dv}{dt}\right)^2 \frac{1}{(1 - \beta \cos\theta)^3} \left[1 - \frac{\sin^2\theta \cos^2\phi}{\gamma^2 (1 - \beta \cos\theta)^2}\right] \tag{2.38}$$

The denominator in each case indicates that the radiation will be emitted preferentially in the propagation direction. This is a consequence of the 'relativistic beaming' effect caused by a Lorentz transformation into a relativistic frame. As a result, the emitted radiation is approximately confined to a cone with opening angle

$$\theta \sim \frac{1}{\gamma}. \tag{2.39}$$

2.5.1 Thomson Scattering

Electromagnetic waves, e.g. from a laser, interact with electrons by inducing oscillations. As a result, the electron emits dipole radiation. This process can be interpreted as the electron scattering incident radiation, and is known as Thomson scattering.

If we consider a monochromatic, linearly-polarised plane wave interacting with an initially stationary electron, the induced dipole moment is

$$\boldsymbol{d} = \frac{e^2 E_0}{m\omega^2} \boldsymbol{\epsilon} \sin\omega t. \tag{2.40}$$

Averaging over the laser cycle, we obtain the time-averaged emitted power per unit solid angle,

$$\frac{dP}{d\Omega} = \left(\frac{e^2}{mc^2}\right)^2 I \sin^2\theta \tag{2.41}$$

where we have substituted the intensity $I = cE_0^2/8\pi$. The bracketed term in eq. 2.41 is the squared electron radius ($r_0 = e^2/mc^2$) and has units of area. Defining the differential cross-section as

$$\frac{dP}{d\Omega} = I\frac{d\sigma}{d\Omega}, \tag{2.42}$$

and integrating over solid angle, we obtain the Thomson cross-section, σ_T

$$\sigma = \frac{8\pi}{3} r_0^2. \tag{2.43}$$

The differential cross-section can be generalised for unpolarised incident radiation (see
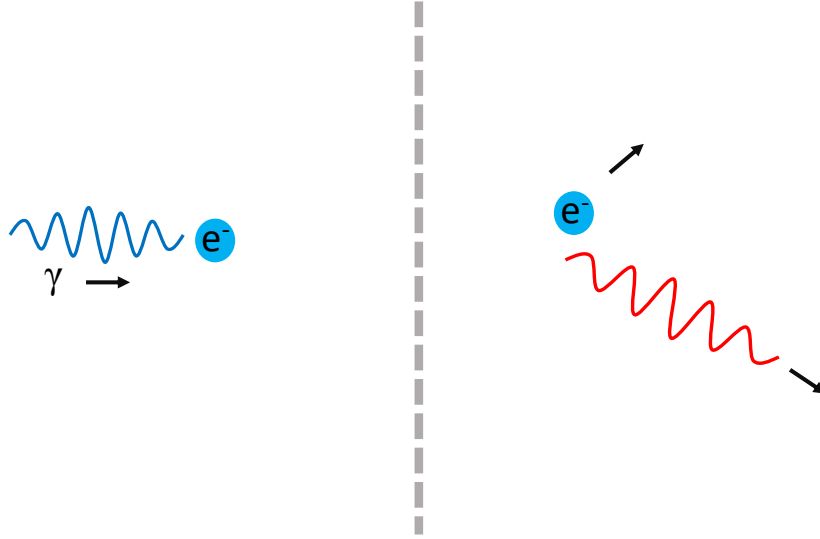
Figure 2.4: Compton scattering from electron. Incident photon transfers momentum to the electron, and is redshifted.

[80, 81]), whereby we find

$$\frac{d\sigma}{d\Omega} = r_0^2 \frac{1}{2} \left(1 + \cos^2\theta\right).$$ (2.44)

Upon integration, we obtain eq. (2.43).

2.5.2   Compton Scattering

In the previous section, we considered the radiation emitted by an electron in the field of a plane wave. In this case the frequency of the radiation is identical to that of the incident radiation, as no net momentum transfer occurs.

We now consider the interaction of a photon of energy $\hbar\omega_0$ with a stationary electron from a kinematic perspective.

A schematic of the interaction is portrayed in Fig. 2.4. Conservation of 4-momentum gives the Compton scattering formula for the energy of the scattered photon,

$$\hbar\omega_1 = \frac{\hbar\omega_0}{1 + \frac{\hbar\omega_0}{mc^2}\left(1 - \cos\theta\right)}$$ (2.45)

Rewriting eq. (2.45) as,

$$\lambda_1 = \lambda_0 + \lambda_c \left(1 - \cos\theta\right)$$ (2.46)

gives the Compton wavelength, defined as $\lambda_c = h/mc$. In the limit where $\lambda \gg \lambda_c$ the
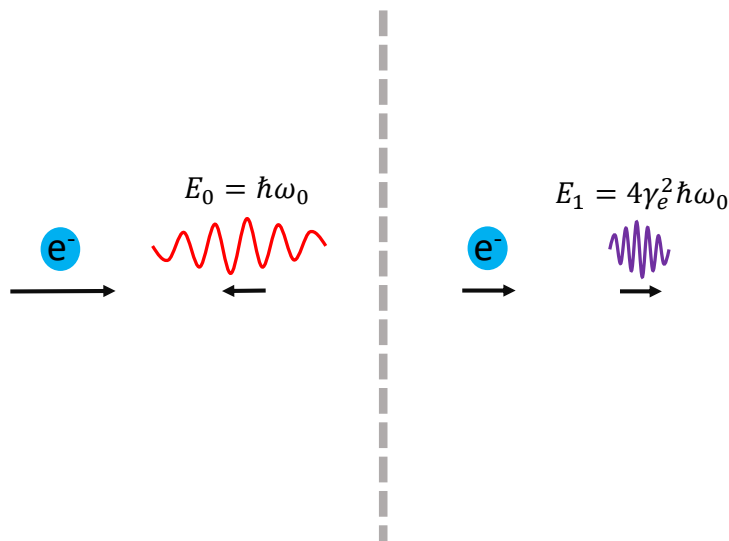
Figure 2.5: Inverse Compton Scattering. Photon energy is upshifted after scattering from electron in motion. In the lab frame, the photon energy is increased by $\gamma_e^2 (1 - \cos\theta)^2$.

change in energy is negligible, i.e. the collision is elastic. Thus Thomson scattering is simply Compton scattering in the low energy limit.

Inverse Compton Scattering

The derivation of Compton scattering began with an electron at rest. We now consider the more general case of an electron in motion. This is quite straightforward, since the principle of relativity allows us to transform into the rest frame of the electron. The interaction therefore reduces to Compton scattering by Lorentz transformation.

Relative to the lab frame, the energy of the photon in the electron's rest frame is Doppler shifted by a factor of $\gamma(1 - \cos\theta)$. Assuming the resulting energy is low, such that $\lambda \gg \lambda_c$, we can use the approximation of Thomson scattering to find the resulting photon energy $\hbar\omega_1 \simeq \hbar\omega_0$. Transforming back into the lab frame requires an additional Doppler shift of $\gamma(1 - \cos\theta)$, giving the observed photon energy as

$$\hbar\omega_1 = \hbar\omega_0\gamma^2 (1 - \cos\theta)^2 . \tag{2.47}$$

It is clear from eq. (2.47) that the maximum upshift occurs for an incident angle of 180°, which results in an increase of $4\gamma^2\hbar\omega_0$.

This is an important result. In principle, the double Doppler shift allows the pro-

duction of X-rays by scattering visible light from relativistic electrons.

Non-linear Effects

For the simple case of a single photon scattering from a single electron, the energy upshift is as described by equation 2.47. However, the interaction of a high-intensity laser with an electron (relativistic or not) requires some additional considerations. An electron interacting with an EM field of $a_0 > 1$ will be accelerated to relativistic velocities, therefore its mass will increase [82]:

$$m = m_0 \sqrt{1 + a_0^2}. \tag{2.48}$$

A high a_0 also means a high photon density, which increases the probability of multi-photon scattering, resulting in harmonic generation.

Taking these effects into account, equation 2.47 then becomes [83],

$$\hbar\omega_1 = \frac{n\hbar\omega_0\gamma^2 \left(1 - \cos\theta\right)^2}{1 + \frac{n\hbar\omega_0\gamma^2(1-\cos\theta)^2}{m_e c^2} + a_0^2}. \tag{2.49}$$

Here, $n \in \mathbb{Z}$ is the number of scattered photons, and thus also the harmonic number.

The consequence of eq. 2.49 for high-intensity laser-electron interactions is that, as we increase a_0 beyond 1, the spectrum of emitted radiation broadens and the fundamental wavelength increases. For $a_0 \gg 1$, the spectrum becomes quasi-continuous [84, 85].

Quantum Effects

The Compton wavelength λ_c can be interpreted as a quantum-mechanical scale length below which the classical wave description of electromagnetic radiation is no longer valid. In our discussion of Compton scattering, we took a kinematic approach, implicitly modelling photons and electrons as rigid spheres[1]. Unfortunately, this is too simplistic and ultimately results in an incorrect value for the cross-section. To find the correct description we require a fully quantum-mechanical treatment which accounts for the spin of the electron. The derivation is outside the scope of this work, so we shall

---

[1]This is essentially the route taken by Compton himself in his derivation [86]

simply state the result and refer the interested reader to Klein *et al.* [87] or Heitler [88]. The differential cross-section is given by the Klein-Nishina formula,

$$\frac{d\sigma}{d\Omega} = \frac{r_0^2}{2} \left(\frac{\omega}{\omega_0} \right)^2 \left(\frac{\omega}{\omega_0} + \frac{\omega_0}{\omega} - \sin^2\theta \right) \tag{2.50}$$

2.5.3 Bremsstrahlung
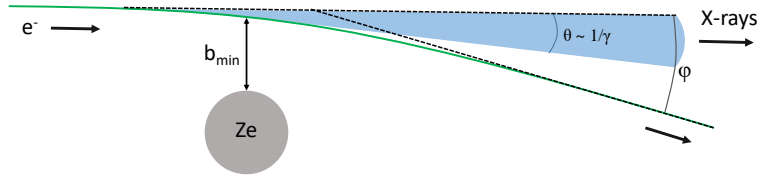
Figure 2.6: Schematic of bremsstrahlung emission. Electron is accelerated by the nuclear charge, resulting in emission of radiation in a cone of angle $1/\gamma_e$.

An electron passing close to an atomic nucleus will have its trajectory altered by the interaction with the Coulomb field. The change in trajectory amounts to an acceleration, and therefore by Larmor's formula we expect the electron to radiate. Bremsstrahlung (braking-radiation) occurs when charged particles in motion are slowed or deflected by external electric fields. For the purposes of this thesis, we will only consider the scattering of relativistic electrons from atomic nuclei (free-bound), although bremsstrahlung is also generated by electron-electron, electron-ion, or ion-ion collisions.

The schematic in Figure 2.6 illustrates the bremsstrahlung process: An electron on an intial trajectory encounters a nuclear field at a minimum distance b_{min} (the impact parameter) and is deflected by an angle ϕ, resulting in the emission of a photon. For highly relativistic electrons, the radiation is concentrated in a cone in the forward direction with opening angle $\theta \sim 1/\gamma$, as is typical.

For a relativistic electron colliding with a nucleus of charge Ze, the cross-section for the emission of a photon with energy in the range $\hbar\omega$ to $\hbar(\omega + d\omega)$ is [82],

$$\frac{d\sigma}{d\omega} = 4Z^2\alpha r_e^2 \frac{1}{\omega}\frac{\gamma'}{\gamma}\left(\frac{\gamma}{\gamma'} + \frac{\gamma'}{\gamma} - \frac{2}{3}\right)\left(\ln\frac{2\gamma'\gamma}{m\omega} - \frac{1}{2}\right), \tag{2.51}$$

where the primed quantities denote the post-interaction conditions.

2.5.4 Synchrotron Radiation

In Sec. 2.5.1 we discussed the emission of radiation by electrons oscillating in electric fields. We now discuss the related case of electrons undergoing circular motion in magnetic fields. The emission in this case is known as cyclotron radiation, and has a frequency equal to that of the circular motion.

For highly relativistic particles, the radiation is beamed according to eq. 2.39 and the frequency spectrum becomes broadband. The energy emitted per unit frequency is given by [80],

$$\frac{dW}{d\omega} = \frac{\sqrt{3}e^2}{c}\gamma\frac{\omega}{\omega_c}\int_{\omega/\omega_c}^{\infty} K_{5/3}(x)dx. \tag{2.52}$$

Here $K_{5/3}$ is a modified Bessel function and ω_c is the critical frequency, defined for motion in a circle of radius R as [89],

$$\omega_c = \frac{3}{2}\gamma^3\frac{c}{R} \tag{2.53}$$

2.6 Radiation Reaction Effects

Energy loss by electrons as they are accelerated is key to the radiative processes discussed above. That energy should be conserved in such an interaction is among the least controversial requirements one could impose. However, the consequences of this —at least in the classical regime— are quite the opposite, as we shall see in this section.

Also in this section we will discuss how the model of radiation and its reaction on charged particles can be improved with quasi-classical considerations.

2.6.1 Classical Radiation Reaction

We can derive a simple relation describing the reaction force on an electron as it radiates starting with the assumption that energy is conserved during the process. To (2.6) we add an additional term F_r describing the reaction force such that,

$$\frac{d\boldsymbol{p}}{dt} = e\left(\boldsymbol{E} + \frac{\boldsymbol{v}}{c}\times\boldsymbol{B}\right) + F_r. \tag{2.54}$$

We start by making the bold assertion that the work done on the particle by this force is equal to the energy radiated, i.e.,

$$- \int F_r dx = \int P dt, \tag{2.55}$$

where P is the radiated power described by Larmor's formula (Sec. 2.5),

$$P = \frac{2e^2}{3c^3} \frac{dv^2}{dt}. \tag{2.56}$$

After a change of variables on the LHS

$$\int F_r v_\mu dt = \frac{2e^2}{3c^3} \int \frac{dv^2}{dt} dt \tag{2.57}$$

the RHS is integrated by parts to give

$$\text{RHS} = \frac{2e^2}{3c^3} \left(\frac{dv^\mu}{dt} v_\mu \Big|_{t1}^{t2} - \int v^\mu \frac{d^2 v_\mu}{dt^2} dt \right). \tag{2.58}$$

The boundary term vanishes, and we are left with the following,

$$\int F_r v^\mu dt = \frac{2e^2}{3c^3} \int v^\mu \frac{d^2 v_\mu}{dt^2} dt. \tag{2.59}$$

Since the region of integration is the same, the integrands are equal, thus

$$F_r = \frac{2e^2}{3c^3} \frac{d^2 v_\mu}{dt^2}. \tag{2.60}$$

The full equation of motion for a radiating particle is therefore,

$$\frac{dv^\mu}{dt} = \frac{e}{mc} F^{\mu\nu} v_\nu + \frac{2e^2}{3c^3} \frac{d^2 v^\mu}{dt^2} \tag{2.61}$$

If we recast this equation in terms of Newtonian mechanics, i.e. replacing 4-vectors by their 3-vector equivalents, we obtain the Lorentz equation for the damping force on a non-relativistic particle[1]. The Lorentz equation is known to admit some unphysical solutions, such as runaway acceleration due to self-interaction, and acausal interaction

---

[1] Although in this case the boundary term in the integration vanishes by requiring that the acceleration be zero at $t1$ and $t2$

with applied forces.

However, within the framework of special relativity, this equation is inconsistent. Since $v_\mu a^\mu = 0$ (4-velocity and 4-acceleration are orthogonal), we can eliminate the LHS of the force equation by multiplying through by v_μ.

$$F^{\mu\nu}v_\nu v_\mu + \frac{2e^2}{3c^3}\frac{d^2v^\mu}{dt^2}v_\mu = 0 \tag{2.62}$$

The first term is zero, since $F^{\mu\nu} = -F^{\nu\mu}$ and $v_\nu v_\mu = v_\mu v_\nu$. Thus when the components are summed over (per convention), the positive and negative terms all cancel, and F is zero along the diagonal.

We are left with

$$\frac{2e^2}{3c^3}\frac{d^2v^\mu}{dt^2}v_\mu = 0 \tag{2.63}$$

which implies that $F_r = 0$, and is therefore inconsistent. Moreover, since F_r is a force and therefore proportional to an acceleration term, we require that $F_r^\mu v_\mu = 0$ to be consistent with relativistic mechanics.

The radiation damping force was rederived by Dirac [90] in the context of special relativity. This equation is known as the Lorentz-Abraham-Dirac (LAD) equation[1]

$$F_r = \frac{2e^2}{3c^3}\left(\frac{d^2v^\mu}{dt^2} + \frac{dv^\mu}{dt}\frac{dv_\mu}{dt}\frac{v^\nu}{c^2}\right) \tag{2.64}$$

which, when contracted with v^μ, vanishes as it should.

Despite Dirac's efforts, the LAD equation still suffers from pathological solutions (for an in depth discussion see [91]). The equation has been modified by several others, including Rohrlich [39], Ford and O'Connell [37], and most notably Landau and Lifshitz [34], to eliminate these solutions. The standard approach is to expand the LAD equation in powers of τ_0, dropping terms which are second order or higher. In each case, however, the results are equivalent to first order in τ_0 [91, 92]. The Landau & Lifshitz result is,

$$\frac{dp^\mu}{dt} = F^{\mu\nu}u_\nu + g^\mu, \tag{2.65}$$

---

[1]Abraham actually derived this result before Dirac, but assumed a finite electron radius, which is problematic under Lorentz transformation. Dirac's result is based on a point-like electron.

where the damping term is

$$g^\mu = \frac{2e^3}{3mc^3} \frac{\partial F^{\mu\nu}}{\partial x^\sigma} v_\nu v^\sigma - \frac{2e^4}{3m^2c^5} F^{\mu\sigma} F_{\nu\sigma} v^\nu + \frac{2e^4}{3m^2c^5} \left(F_{\nu\sigma} v^\sigma\right) \left(F^{\nu\tau} v_\tau\right) v^\mu \qquad (2.66)$$

For highly relativistic particles, this can be simplified by noting that the first term contains the 4-velocity squared, the second term 4-velocity, and the final term contains the 4-velocity cubed. Thus in the relativistic limit, the damping force can be approximated as

$$g^\mu = \frac{2e^4}{3m^2c^5} \left(F_{\nu\sigma} v^\sigma\right) \left(F^{\nu\tau} v_\tau\right) v^\mu \qquad (2.67)$$

Expanding the field components for a particle moving in the x-direction gives

$$g_x = -\frac{2e^4}{3mc^2c^4} \gamma^2 \left(E_y - B_z\right)^2 + \left(E_z + B_y\right)^2 \qquad (2.68)$$

The γ^2 term indicates that the damping force on the particle is proportional to the square of its energy. This is a key characteristic of radiation damping in the classical regime. In essence, particles of higher energy radiate energy more rapidly in the presence of an electromagnetic field, resulting in a reduction in energy spread.

2.6.2   Quantum Corrections

In preparation for the discussion of quantum effects, we first rewrite the classical equations for synchrotron radiation, and the power emitted by an accelerated electron, in terms of some important quantities [93]:

$$P = \frac{2}{3} \frac{\alpha_f}{\tau_C} \eta^2 mc^2. \qquad (2.69)$$

Here we have introduced the Compton time, $\tau_C = \lambda_c/c = \hbar/mc^2$, and the quantum nonlinearity parameter η.

The value of η is defined as

$$\eta = \frac{e\hbar}{m^3c^4} |F_{\mu\nu} p^\nu|, \qquad (2.70)$$
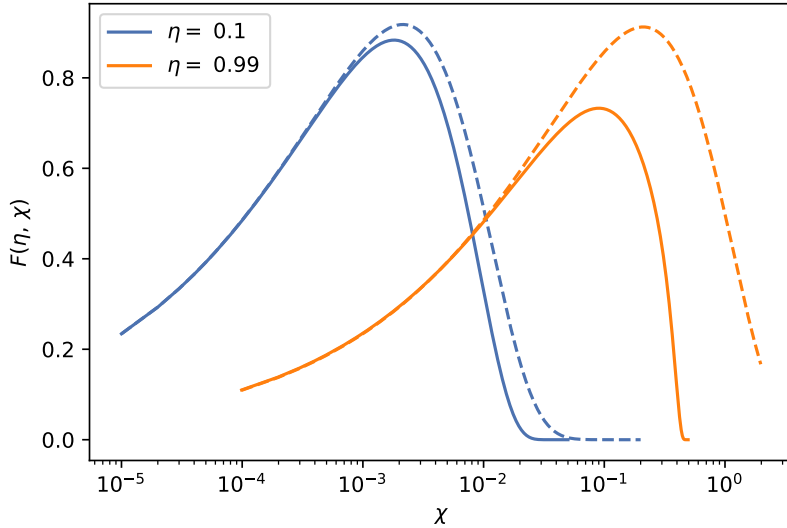
Figure 2.7: Synchrotron spectra for two values of η in classical (dashed) and quantum (solid) models. As $\eta \to 1$, the classical synchrotron power overestimates the emitted power, particularly at high energies.

which, for relativistic electrons, can be expressed in terms of the field quantities as,

$$\eta = \gamma \frac{|\boldsymbol{E} + \boldsymbol{v} \times \boldsymbol{B}|}{E_{Sch}}, \tag{2.71}$$

where $E_{Sch} = e\hbar/m^2c^3$ is the Schwinger critical field [94]. η can be interpreted as a measure of the importance of quantum effects in interactions between electrons and radiation fields [95]. For $\eta \ll 1$ we should expect purely classical behaviour, whereas for $\eta \geq 1$, interactions are dominated by quantum effects, such as stochastic emission, and prolific pair production [96].

It is well-known from quantum electrodynamics that the synchrotron power is reduced compared to the classical case, most notably for high field strengths; $\eta \sim 1$. The reason for the classical overestimate is that the energy of the electron as it emits is not taken into consideration, and as such radiation (i.e. photons) may be emitted with energy higher than that of the electron. In Figure 2.7, the different predictions are illustrated.

For $\eta \ll 1$, the classical expression is valid, and for larger values the QED result can be approximated by including a Gaunt factor $g(\eta)$, such that,

$$P_{QED} = P\,g(\eta) \tag{2.72}$$

η	g
0.01	0.95
0.1	0.66
0.99	0.18

Table 2.1: $g(\eta)$ for some example values of η
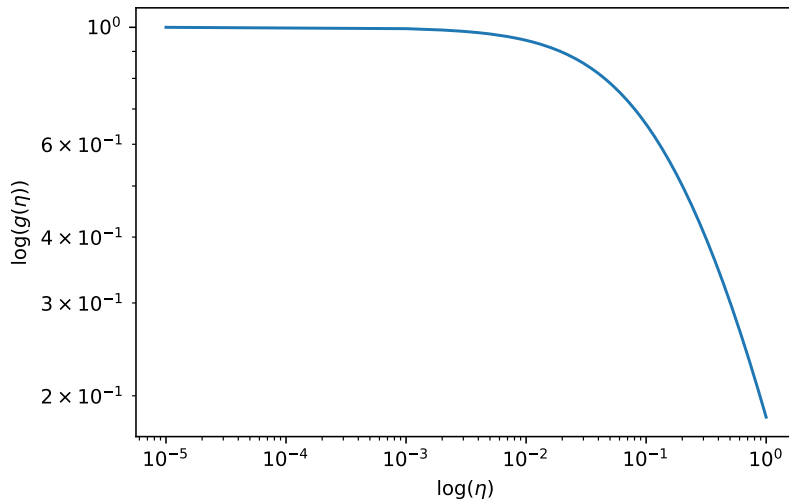
Figure 2.8: Plot of $g(\eta)$. The power radiated is modified by a factor in the range [0,1].

The expression for $g(\eta)$ is [93, 97]

$$g(\eta) = \frac{9\sqrt{3}}{8\pi} \int_0^\infty dy \frac{2y^2 K_{5/3}(y)}{(2+3\eta y)^2} + \frac{36\eta^2 y^3 K_{2/3}(y)}{(2+3\eta y)^4}. \tag{2.73}$$

Despite its complexity, the effect of $g(\eta)$ is straightforward: the power radiated is modified by a correction factor in the range $[0, 1]$. Some illustrative examples are shown in Table 2.1.

Effect of $g(\eta)$ on the Radiation Reaction Force

The modification of the radiated power by $g(\eta)$ affects the radiation damping force. Since the RR force is derived from the radiated power, the corrected force term is simply the classical value multiplied by $g(\eta)$.

2.6.3 Stochastic Emission

While the modification of the classical synchrotron function correctly predicts the radiated power, it does not account for the quantum nature of the process. In the quantum

44
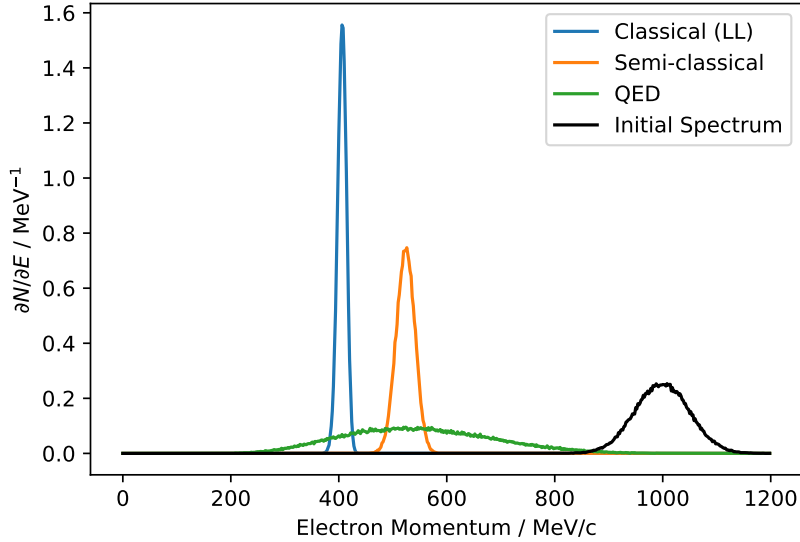
Figure 2.9: Energy loss due to RR in different regimes for a $1\,\mathrm{GeV}$ electron bunch. Both the classical and semi-classical models result in compression of the spectrum. The QED result has the same mean as the semi-classical, but is broader than the initial spectrum on account of the stochasticity. Plot generated using epoch1D.

regime, electrons do not emit continuously, but rather stochastically. Furthermore, unlike in the classical case, the electron's initial energy merely sets an upper bound on the energy of the emitted photon; the photon energy is not deterministic.

In the interaction of a laser with a relativistic electron, the laser pulse typically has a Gaussian intensity profile, which means that the value of η in the centre of the pulse will be higher than the edges. Classically, the electron encounters the front of the pulse first and begins to radiate immediately. In the quantum picture, however, the electron may chance upon the centre of the pulse without radiating at all. In this case, the electron experiences a higher η than it would classically and moreover may emit a photon of much higher energy. This process is called 'straggling' [98].

2.6.4 Radiation Reaction in Laser-Plasma Interactions

The validity of the various models of RR discussed above are still very much in question. Although these results are derived from a well-established framework, approximations are required to render the calculations tractable. Whether such approaches are valid can therefore only be determined by the ultimate arbiter of truth: Experimental investigation.

Radiation Dominated Regime

Historically, radiation reaction effects have been largely ignored due to their relatively small effect on electron motion. Under certain conditions, however, the damping force makes a contribution comparable to the Lorentz force, i.e. $F_{RR} \sim F_L$. This regime, described by Bulanov *et al.* [99], occurs when electrons encounter sufficiently high-fields. Specifically, by equating the Lorentz and radiative terms in the LAD equation, Bulanov estimates that the 'radiation dominated regime' (RDR) occurs when $a_0 \simeq 440$. For comparison, the record intensity achieved by the Hercules laser corresponds to $a_0 \simeq 97$.

However, with the goal of measuring RR in mind, the requirement that the RR force be equal in magnitude to the Lorentz force is too strict. Koga *et al.* [100] and Thomas *et al.* [92] define the RDR to occur when 'significant' energy loss has occurred. For the following discussion we shall use the definition of Thomas[1].

For a relativistic electron interacting with a counterpropagating gaussian pulse of duration t_L, the total energy lost due to damping forces is

$$\frac{\Delta\gamma}{\gamma_0} = \frac{\sqrt{\pi/2}\,\tau_0\omega_0^2\gamma_0 a_0^2 t_L}{1 + \sqrt{\pi/2}\,\tau_0\omega_0^2\gamma_0 a_0^2 t_L}, \tag{2.74}$$

from which we define a parameter ψ,

$$\psi = 10\sqrt{\pi/2}\,\tau_0\omega_0^2\gamma_0 a_0^2 t_L t_{rad}. \tag{2.75}$$

Here, the term t_{rad} refers to a characteristic timescale for radiation damping. Choosing this to be the laser period $2\pi/\omega_0$, we find that

$$\frac{\Delta\gamma}{\gamma_0} = \frac{0.1\psi(t/t_{rad})}{1 + 0.1\psi(t/t_{rad})}. \tag{2.76}$$

For $t = t_{rad}$, then, the electron loses around 10% of its energy within a laser cycle.

From this definition, $\psi \geq 1$ corresponds to the RDR. For a laser with $\lambda = 800\,\mathrm{nm}$, ψ can be described by a convenient engineering formula:

$$\psi = 0.12\left(\frac{\gamma_0}{1000}\right)\left(\frac{a_0}{10}\right)^2, \tag{2.77}$$

---

[1]The work by Thomas *et al.* is based on experiments conducted using laser and electron parameters achievable with Gemini or Hercules, and therefore the definition of the RDR used here is more appropriate to the results in chapter 4.

Thus, for electrons of $500\,\mathrm{MeV}$, the RDR occurs when $a_0 \geq 29$.

2.7 Summary

In this chapter we have explored the basic properties of plasmas and how they can be exploited to accelerate electrons using laser-wakefield acceleration. We have also discussed the primary mechanisms by which radiation is emitted by electrons undergoing acceleration. The means of acceleration, e.g. scattering from electrons, nuclei, etc., determines what we call the process, but the underlying concepts are the same.

The emission of radiation by accelerated charges is accompanied by a loss of energy, termed 'Radiation Reaction'. Despite the simple concept, we have seen that modelling RR accurately remains at the cutting edge of research.

Chapter 3

Apparatus and Methodology

3.1 High-Power Lasers

3.1.1 The Gemini Laser

Commissioned in 2008, the Gemini laser (Figure 3.1) was built upon the pre-existing Astra system at the Central Laser Facility. Gemini is a petawatt-class, titanium-sapphire (Ti:S) system consisting of, as the name suggests, two independent beamlines. Each beam delivers up to 15 J at 800 nm (the bandwidth is approximately 35 nm [101]). Although the system was designed to produce 15 J in 30 fs for each beam, the minimum pulse length upon commissioning was 45 fs [102]. Presently, the typical operating pulse length on Gemini is 45 fs to 55 fs.

Astra and Gemini are fed by a single oscillator, and share the first 3 amplification stages. The output from the third amplifier is nominally 1.2 J at a repetition rate of 10 Hz. A rotating waveplate acts as a pulse switcher, sending every alternate pulse to the Astra target area (ATA2).

Pulses sent to the Gemini laser area are split and sent into a fourth amplification stage, producing 25 J of laser energy. The pulses are then compressed, and delivered to the target area (TA3). Due to energy loss in the compression process, around 15 J of energy is delivered to the target area in each beam.
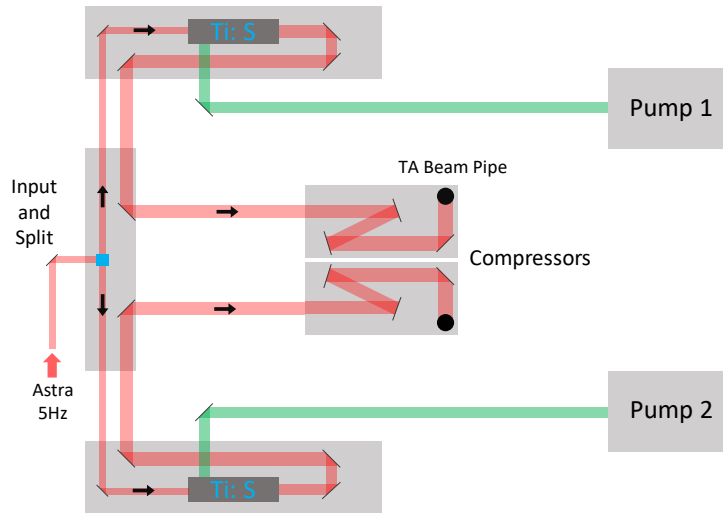
Figure 3.1: Schematic of the Gemini laser system. The stretched Astra beam is split in two and passed into Ti:Sapphire amplifiers, increasing the energy in each beam to around 25 J. The beams are separately compressed and directed into the target area below via beam pipes.

3.1.2 Pulse Modification and Laser Diagnostics

Laser-plasma phenomena, e.g. LWFA are extremely sensitive to the properties of the driving laser pulse, thus it is crucial to control —and measure— pulse parameters as accurately as possible.

Wavefront Sensing and Adaptive Optics

The quality of a focal spot, i.e. the Strehl ratio, may be degraded by various factors. Imperfect optical elements along a beamline will alter the spatial structure of the beam; thermal lensing in the amplifiers creates 'hotspots'. In order to achieve a high-quality focal spot, aberrations in the wavefront must be corrected.

A Shack-Hartmann sensor measures the pointing of small regions of the beam with an array of lenses, thereby inferring the relative phase across the wavefront. By pairing the sensor with an adaptive optic (AO), the phase aberrations can be corrected.

An AO is a deformable mirror with an array of actuators that displace local regions of the surface to compensate for phase offsets. To correct the wavefront, the degree of offset is first measured by the sensor. Each of the actuators is then moved in turn to establish the effect on the wavefront. Finally, the required pattern of actuator motion is calculated, and the corrections applied to the AO.

Energy Calibration

The energy contained in the laser pulse can be measured directly using a calorimeter. However, it is rarely practical to include such a device in the experimental setup. Instead it is sufficient to calibrate a CCD camera using the leakage behind an optic such that the relationship between the integrated pixel counts and the pulse energy is known. In the Gemini system, a beam profile monitor serves this purpose. Energy loss in the compressor is measured during maintenance, and a correction factor applied to the integrated image. This method allows unobtrusive, on-shot measurement of the energy in the pulse.

Pulse-Shaping

The pulse duration in a CPA laser system is set by the arrangement of the compressor gratings. An optimally compressed pulse in Gemini is around 44 fs (FWHM). For LWFA applications, the pulse length should be chosen for a given plasma wavelength (i.e. electron density). Adjusting the compressor gratings is a time-consuming and delicate process, and so this is not a suited to the high repetition rate required for electron acceleration experiments. The temporal shape of the laser pulse can be adjusted in the front-end of the system by using an Acousto-Optic Programmable Dispersive Filter (AOPDF) [103]. Despite its catchy title, the AOPDF used in Gemini is referred to by its brand name, the *Dazzler*[1]

Pulse Length Measurement

Optical pulses as short as 100 ps can be detected and characterised by photodiodes. However, the characterisation of femtosecond pulses can only be done by optical means.

A single-shot autocorrelator [104] splits the pulse with a beamsplitter, then recombines the light inside an SHG crystal. As the pulses pass through the crystal, second-harmonic light is produced where they overlap, which is then detected by a camera. The autocorrelation process effectively encodes the temporal characteristics of the pulse into a spatial representation which can be measured directly. An important caveat is that the temporal shape of the pulse does not uniquely determine the autocorrelation signal, and so an initial pulse shape must be assumed.

---

[1] *Dazzler* is a trademark of Fastlite.
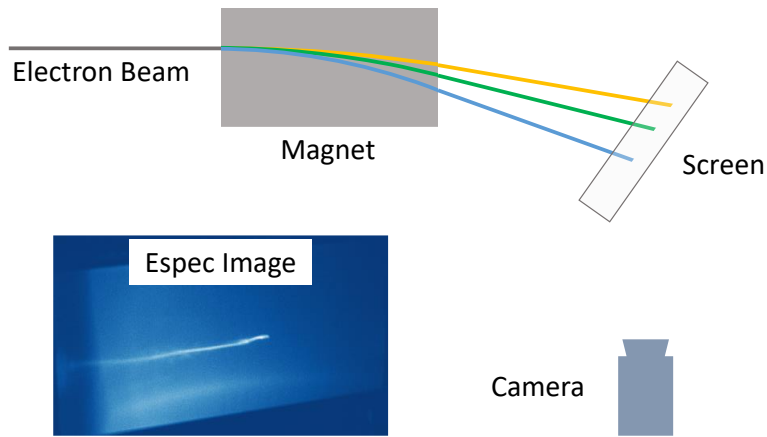
Figure 3.2: Dispersion of electrons by dipole magnet. High energy electrons are deflected less than low energy ones, enabling energy discrimination at the screen.

In addition to the temporal shape of the pulse, the spectral phase can also be recovered by a technique known as 'Frequency-Resolved Optical Gating' (FROG) [105]. The FROG technique combines a single-shot autocorrelator with a dispersive element, such as a grating, to obtain the frequency components of the pulse. The resulting 2-dimensional image encodes the temporal information along one axis, and the spectral components along the other. Recovering the pulse shape from this data is quite involved, however. See [106] for a detailed discussion.

3.2 LWFA Diagnostics

Whether LWFA is the object of research, or used to generate an electron source for other applications (e.g. X-ray sources), it is important to make quantitative measurements of the electron beam properties. In the following sections, we will describe the main diagnostic techniques which apply to the results in Chapters 4 and 5.

3.2.1 Electron Spectrometry

Knowledge of the electron energy distribution is often crucial, particularly for secondary sources such as bremsstrahlung, as the resulting X-rays depend strongly on the incident electron spectrum.

The standard approach in laser-plasma experiments is to disperse the electrons with a dipole magnet. By placing a scintillating screen in the path of the particles, the energy spectrum can be obtained using a calibrated optical camera. Figure 3.2 is

a schematic of a typical electron spectrometer.

The most common technique for detecting electrons is to use an inorganic, scintillating screen such as Lanex (Gd_2O_2S:Tb) which emits light at $546\,nm$ ($5\,nm$ FWHM) when struck by electrons [107]. For electrons above around $1\,MeV$, the energy deposited in the Lanex is constant, thus the light emitted is directly proportional to the charge [108, 109]. The camera imaging system can then be calibrated by comparing the images to data taken from image plate in front of the Lanex, which also has linear charge-to-signal response above $3\,MeV$ [110, 111].

To calculate the trajectory of the electrons through the magnet, we can use the Lorentz force equation derived in Chapter 2 (2.6) which describes the motion of charged particles in electromagnetic fields. For a purely magnetic field, as in a dipole magnet, the equation of motion becomes

$$F = -\frac{e}{c}\boldsymbol{v} \times \boldsymbol{B} \tag{3.1}$$

The work done on the particle, dW, by the magnetic field over a distance $d\boldsymbol{x}$ is

$$dW = \boldsymbol{F} \cdot d\boldsymbol{x} = \boldsymbol{F} \cdot \frac{d\boldsymbol{x}}{dt}dt = -\frac{e}{c}\boldsymbol{v} \cdot (\boldsymbol{v} \times \boldsymbol{B}) = 0. \tag{3.2}$$

Thus the energy of the particle remains constant in the magnetic field, and only the direction of propagation is affected. By solving (3.1) for the particle trajectories, we find that the motion is cicular with a characteristic radius (the *gyroradius*) given by,

$$r_G = \frac{\gamma m v_\perp}{eB_0}, \tag{3.3}$$

where $v_\perp$ is the velocity component perpendicular to $\boldsymbol{B}$, and $B_0 = |\boldsymbol{B}|$.

Since the gyroradius scales with the particle momentum $\boldsymbol{p} = \gamma m\boldsymbol{v}$, the energy of an electron passing through a dipole magnet can be determined from the deflection angle.

By considering the geometry of the magnet in question, the intersection of dispersed electrons with the scintillating screen can be calculated analytically [112], however, this assumes an idealised magnet with a uniform field between the poles, and no fringe fields. Experimentally, the spectrometer calibration is carried out by first generating a field map using a Hall probe. The magnetic field profile is then used in a particle tracking
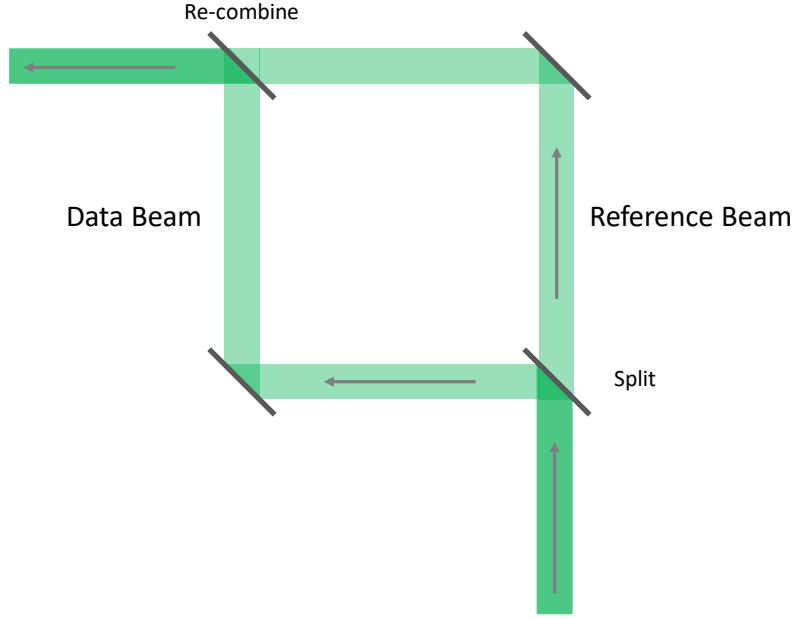
Figure 3.3: Schematic of a Mach-Zehnder interferometer. The input beam is split by a beamsplitter, with one line used as a reference. The data and reference lines are recombined to produce an interference pattern.

simulation which gives the trajectories of the dispersed electrons.

3.2.2 Plasma Density Measurement

The electron density inside a plasma channel is a quantity of interest for LWFA, and can be diagnosed by transverse optical probing of the gas target during the interaction. A direct measurement of the density can be obtained by interferometry, which exploits the variation in refractive index, and therefore optical path, across the channel.

A simple interferometer consists of a beam of incident light which is split into two components of equal intensity, and then recombined after some distance. One of the beams passes through the region of interest, while the other does not. Upon recombination, the two beams produce an interference pattern as a result of the varying path length. Figure 3.3 shows a schematic of a Mach-Zehnder style of interferometer.

A change in refractive index in the plasma will cause a localised fringe shift in the image (Figure 3.4), which corresponds to a phase shift $\Delta\phi$,

$$\Delta\phi = \frac{\omega}{c} \int \left[\left(1 - \frac{n_e}{n_c} \right)^{1/2} - 1 \right] dl \tag{3.4}$$

The mathematical procedure of electron density reconstruction lies outside the scope
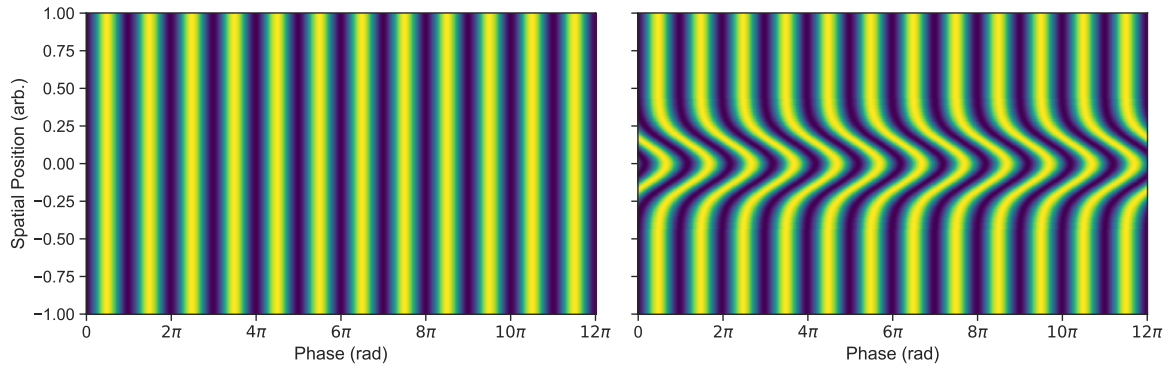
Figure 3.4: Simulated interferogram of plasma channel. The phase shift is related to the electron density in the channel by eq. 3.4.
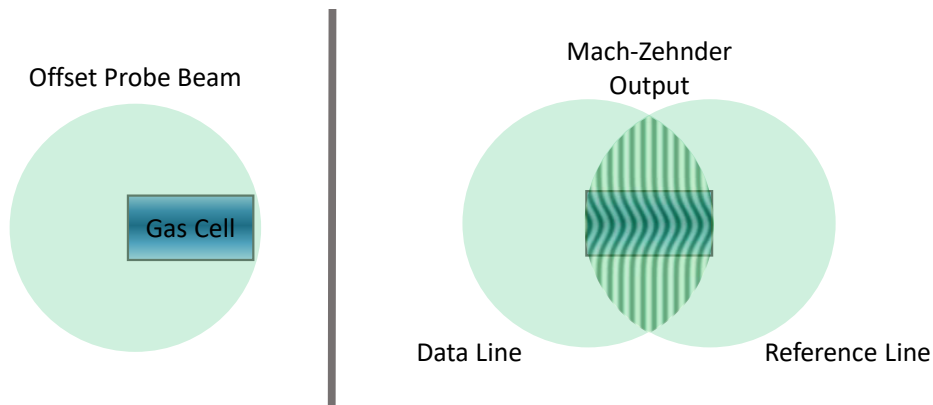
Figure 3.5: Interferometry using an offset probe. The probe beam is offset from the target, such that only part of the beam passes through the plasma. The remainder of the beam is used as a reference.

of this thesis, however the general principles can be found in [113]. For a detailed discussion of the process, see [112].

A convenient modification to the Mach-Zehnder interferometer for LWFA experiments is to place the entire setup after the gas target. This results in two identical images of the target. Provided the plasma channel does not fill the field of view of the incident probe beam, the images can be offset slightly to obtain a single image of the plasma as before (see figure 3.5). The main advantages of this approach are that it vastly reduces the size of the diagnostic, and also makes it considerably easier to match the timing between the arms of the interferometer.

3.3 Image Processing Techniques

Experimental data from LWFA is often collected by way of optical systems. For example, an electron spectrometer might consist of a scintillating screen imaged by a CCD camera. To translate camera images into quantitative data usually requires some post-processing in order to compensate for background noise, optical aberrations, or perspective.

3.3.1 Kernel Convolution

The term 'Kernel Convolution' refers to a class of operations designed to modify images for the purpose of filtering noise, or enhancing features such as edges. Essentially, the value of each pixel in the image is recalculated based on the values of its immediate neighbours.

We achieve this by convolving a matrix, or kernel, with the image. The values contained in the kernel are specific to the desired operation. As an example, consider the following operation: A kernel, $\boldsymbol{A}$ of size 3×3 is convolved with an image, $\boldsymbol{B}$ of size 5×5,

$$\boldsymbol{A} = \begin{bmatrix} 0 & 0 & 0 \\ 0 & \frac{1}{2} & 0 \\ 0 & 0 & 0 \end{bmatrix} ; \; \boldsymbol{B} = \begin{bmatrix} 2 & 2 & 2 & 2 & 2 \\ 2 & 2 & 2 & 2 & 2 \\ 2 & 2 & 2 & 2 & 2 \\ 2 & 2 & 2 & 2 & 2 \\ 2 & 2 & 2 & 2 & 2 \end{bmatrix}. \tag{3.5}$$

Each entry in the resulting image is calculated by first overlapping the centre of the kernel with the target pixel. The kernel is then multiplied elementwise with the region of the image it overlaps, and the resulting values summed. The target pixel value is then replaced with the result of this sum. Using the examples above, each new pixel value is calculated as follows:

$$c_{ij} = [8 \times (0 \times 2)] + \left(\frac{1}{2} \times 2 \right) = 1. \tag{3.6}$$

Thus the pixel values in our 'image' $\boldsymbol{B}$ are reduced by half.
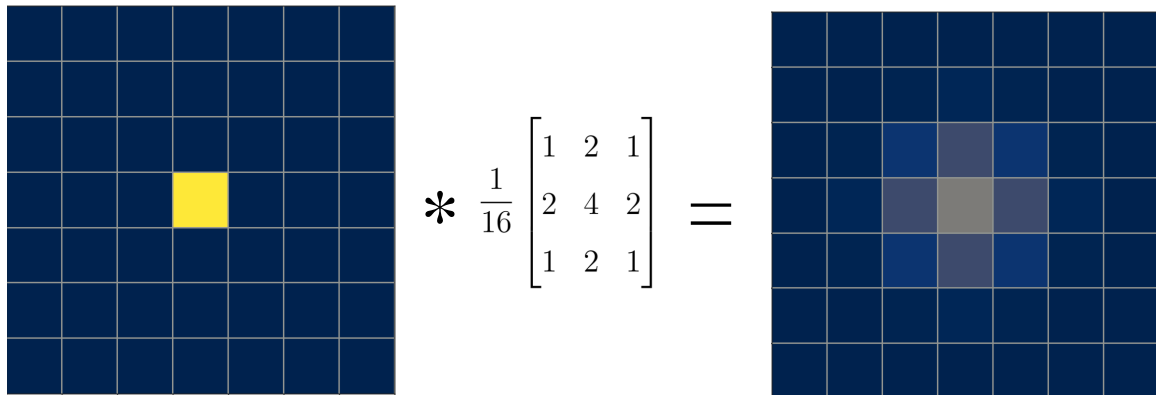
Figure 3.6: Effect of Gaussian Blur.

Gaussian Filter

A more interesting kernel is the Gaussian filter (or Gaussian blur), in which the values are weighted according to a normal distibution. For example, a 3×3 Gaussian filter kernel may be constructed as follows[1]:

$$\boldsymbol{G} = \frac{1}{16} \begin{bmatrix} 1 & 2 & 1 \\ 2 & 4 & 2 \\ 1 & 2 & 1 \end{bmatrix} \tag{3.7}$$

The effect of this kernel when applied to an image is to redistribute the value of each pixel among its neighbours, as illustrated in figure 3.6. This smooths out prominent features of the image, such as hard edges. A Gaussian filter is useful for removing background noise from an image, which can obscure data. As an example, consider the image on the left of figure 3.7. We imagine that this represents a signal we wish to measure, e.g an X-ray beam profile (see Chapter 5 for a real example). An experimental measurement of this signal may look more like the middle image, in which the signal is masked by a large amount of background noise. To the human eye, the original signal is still apparent, but quantifying the signal is difficult. The height and position of the peak are ambiguous, for instance.

Applying a Gaussian filter to the middle image we remove almost all of this noise without sacrificing the original signal. The image on the right and its corresponding lineout are slightly degraded compared to the true signal, however the key features can

---

[1]The values used here are not exact, and only for illustration.
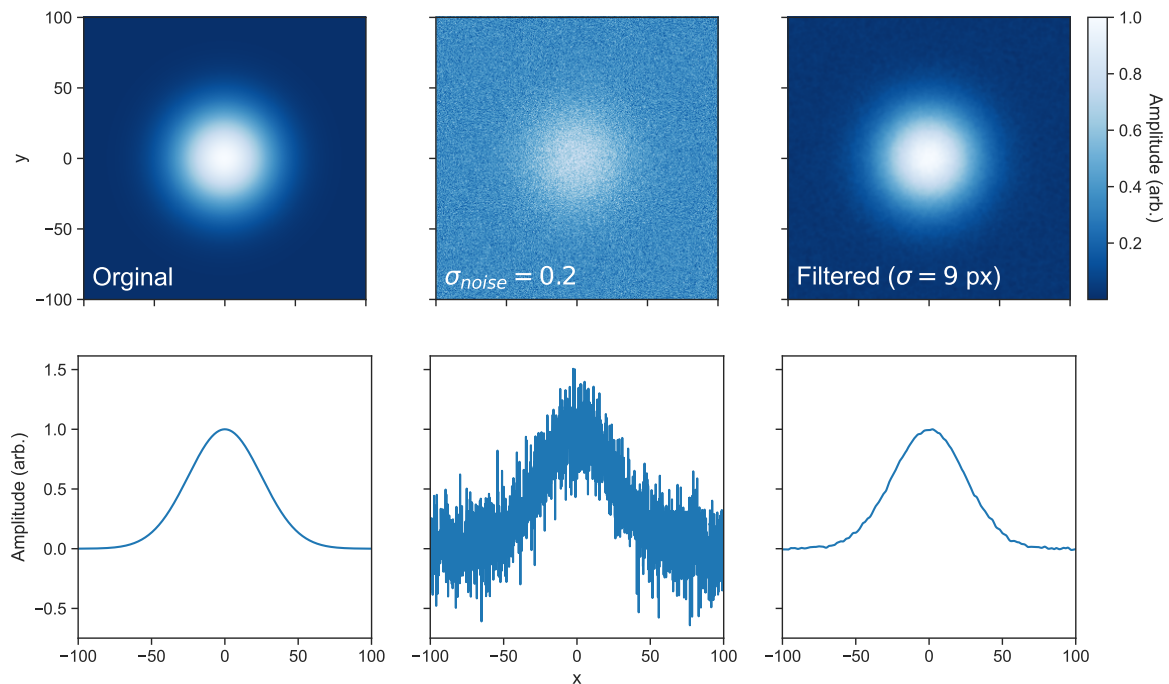
Figure 3.7: Example of signal recovery using Gaussian filter.

be extracted with very little error.

Median Filter

Another useful filtering technique is the median filter. Although not strictly a kernel convolution, the process is similar enough to justify including it here. To operate on an image, rather than a pre-defined kernel, we use a window of a chosen size. For each pixel in the image, we overlap the window and replace the target pixel with the median of its neighbours, including itself (Eq. 3.8).

$$a_{ij} \rightarrow \text{median} \begin{bmatrix} \ddots & \cdots & \\ \vdots & a_{ij} & \vdots \\ & \cdots & \ddots \end{bmatrix} \tag{3.8}$$

Median filtering is particularly useful for processing data from laser-plasma experiments, since we often encounter large numbers of 'hot-pixels' on camera images. Unlike the background noise generated by the camera electronics, these occur when the camera chip is struck by high energy particles such as electrons or X-rays. They are typically quite diffuse, having the appearance of salt and pepper scattered on the image. Also unlike the previous example, hot pixels are often of comparable magnitude
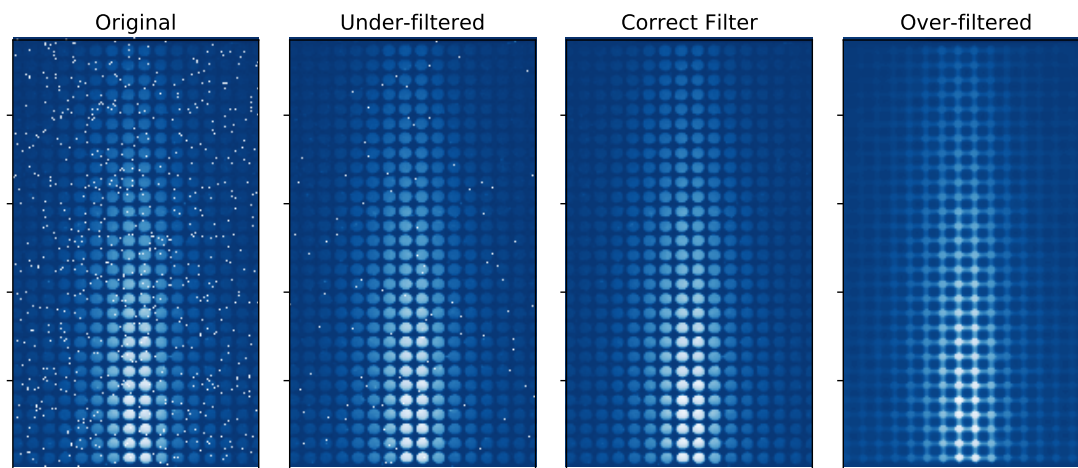
Figure 3.8: Effect of different levels of median filter on image.

to the signal we are trying to measure, and may even saturate regions of the sensor.

Using a Gaussian filter would be ineffective in this case, as we would simply be spreading the value of the hot pixel over a larger area, while also degrading our signal. Instead, since they usually consist of a single pixel (or a few pixels), we can remove them entirely by median filtering. With a filter size of 3×3, for example, we would have 8 dark pixels and one bright pixel, the median of which is one of the dark pixels. This democratic method of noise removal has the added bonus of only minimally affecting the rest of the data.

Care must be taken, however, to choose the right size of median filter for the image. The window size (in pixels) should be much smaller than any features we wish to preserve. An example of this is shown in figure 3.8. Applying a filter which is too small does not effectively remove all the hot-pixels, whereas a large filter degrades the signal by generating artefacts.

3.3.2 Projective Transformation

Often in experimental situations we rely on camera images to gather data. For example, an electron spectrometer like the one described above (Sec. 3.2.1) uses Lanex which is imaged by a CCD camera. It is not always possible to place the camera such that the screen is viewed at normal incidence, and so we must deal with perspective effects.

The rectangular shape of a Lanex screen maps to a trapezoid on the camera sensor, which distorts the shape of any data as well. This can be overcome by applying a
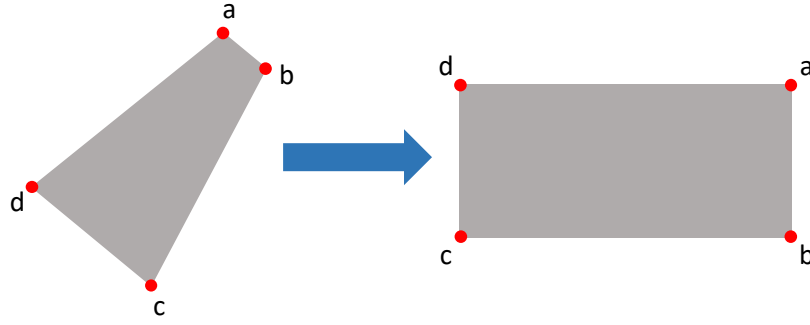
Figure 3.9: Projective transform to correct for camera angle

projective transform to the image, to effectively 'undo' the perspective change caused by camera placement.

A projective transformation of a point in 2D space (x, y) to a new point (u, v), is conveniently represented by use of homogeneous coordinates, i.e.

$$\begin{bmatrix} x \\ y \end{bmatrix} \rightarrow \begin{bmatrix} x \\ y \\ 1 \end{bmatrix} ; \quad \begin{bmatrix} u \\ v \end{bmatrix} \rightarrow \begin{bmatrix} u \\ v \\ 1 \end{bmatrix} \tag{3.9}$$

This allows us to encode all possible 2D operations[1] in a single 3×3 matrix, and the transformation becomes,

$$\begin{bmatrix} x \\ y \\ 1 \end{bmatrix} = \lambda \begin{bmatrix} a & b & c \\ d & e & f \\ g & h & 1 \end{bmatrix} \begin{bmatrix} u \\ v \\ 1 \end{bmatrix} . \tag{3.10}$$

The 8 parameters $a...h$ define the transformation. For each point in the camera plane and its corresponding point on the Lanex we obtain two equations in terms of $a...h$,

$$x = \frac{au + bv + c}{gu + hv + 1}; \quad y = \frac{du + ev + f}{gu + hv + 1}. \tag{3.11}$$

With 8 unknowns, we require an additional 6 equations to find a unique solution, thus we must know the coordinates of 4 points in the Lanex plane and the matching points on the image.

---

[1] translation, rotation, scale, shear, and projection

We then rearrange the 8 equations into a matrix equation as follows:

$$
\begin{bmatrix}
u_1 & v_1 & 1 & 0 & 0 & 0 & -x_1 u_1 & -x_1 v_1 \\
0 & 0 & 0 & u_1 & v_1 & 0 & -y_1 u_1 & -y_1 v_1 \\
u_2 & v_2 & 1 & 0 & 0 & 0 & -x_2 u_2 & -x_2 v_2 \\
0 & 0 & 0 & u_2 & v_2 & 0 & -y_2 u_2 & -y_2 v_2 \\
u_3 & v_3 & 1 & 0 & 0 & 0 & -x_3 u_3 & -x_3 v_3 \\
0 & 0 & 0 & u_3 & v_3 & 0 & -y_3 u_3 & -y_3 v_3 \\
u_4 & v_4 & 1 & 0 & 0 & 0 & -x_4 u_4 & -x_4 v_4 \\
0 & 0 & 0 & u_4 & v_4 & 0 & -y_4 u_4 & -y_4 v_4
\end{bmatrix}
\begin{bmatrix}
a \\ b \\ c \\ d \\ e \\ f \\ g \\ h
\end{bmatrix}
=
\begin{bmatrix}
x_1 \\ y_1 \\ x_2 \\ y_2 \\ x_3 \\ y_3 \\ x_4 \\ y_4
\end{bmatrix}
\tag{3.12}
$$

Finding the inverse of the 8×8 matrix gives the transformation constants.

Computer vision packages such as *OpenCV* have robust implementations of the projective transformation which allow for straightforward analysis of images, so it generally not necessary to perform these calculations manually.

3.4   Radiation Detection

In section 3.2.1 we discussed electron spectrometry as a key diagnostic for laser-plasma experiments. As well as electrons, we typically generate copious quantities of X-rays in such experiments, either by Compton scattering as in Chapter 4, or by bremsstrahlung as in Chapter 5[1]. Detecting this radiation possible using either passive or active means.

3.4.1   Image Plate

Passive detection of X-rays using silver bromide film, or more recently[2] phosphor-based image plate, relies on incident X-rays effecting a chemical change inside a material. In AgBr film, incident light stimulates recombination of Ag^+ ions with electrons, producing metallic silver.

Image plate (IP) takes advantage of a process called 'photostimulated luminescence' (PSL) in which electrons are excited to a metastable state, where they become 'trapped'. Illumination by visible light then stimulates electron transition back to the

---

[1]LWFA sources also produce betatron radiation, which is typically in the $1\,\text{keV}$ to $10\,\text{keV}$ range.
[2]Not *that* recently [114].
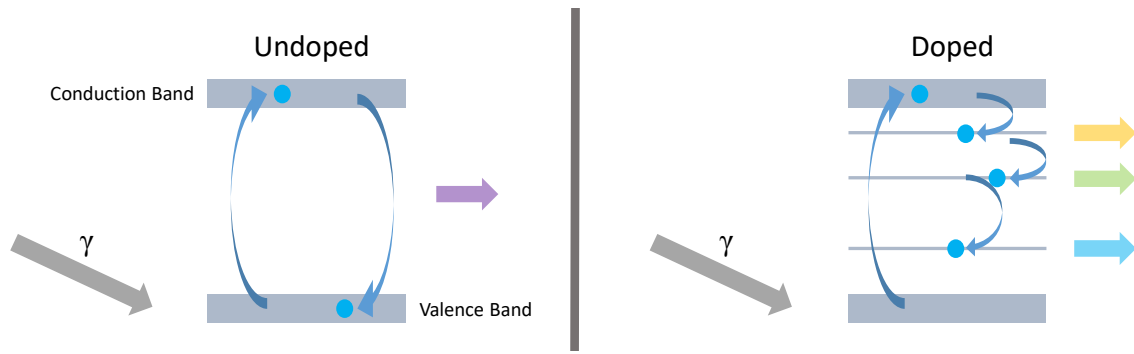
Figure 3.10: Scintillation process in doped vs. undoped inorganic crystal (e.g. CsI, LYSO).

ground state, emitting visible light in the process. The main advantage of IP over film is that it is reusable: By exposing it to bright light, all electrons return to the ground state and the information is wiped. It also offers a larger dynamic range than both film and X-ray CCDs [115], making it a useful diagnostic tool despite it being comparatively 'low-tech'.

IP typically consists of an active layer of barium fluorobromide (BaFBr) doped with Eu^{2+}, which is ionised to Eu^{3+} by incident radiation, providing electrons for trapping. The active layer is sandwiched between a magnetic backing layer and a protective top layer such as mylar. The thickness of the active layer is varied between types of image plate to modify the sensitivity to particular energy ranges, and the protective layer is absent in the 'TR' variant to increase sensitivity to low energy ($\leq 2\,\text{keV}$) X-rays and protons [116].

3.4.2 Scintillators

Scintillators are a class of material which emit light in response to incident radiation. In inorganic scintillators, such as CsI, LYSO[1], or Lanex, electrons absorb photons and are excited into the conduction band. Photons are then emitted upon de-excitation.

The light emitted from pure scintillators is normally in the EUV region, and so not particularly easy to detect. This can be overcome by including impurities, or dopants, which introduce intermediate energy bands between the valence and conduction bands to temporarily 'trap' electrons. De-excitation from these levels causes emission of photons in the visible range (figure 3.10). Caesium iodide, for example can be doped

---

[1]Lutetium Yttrium Oxyorthosilicate
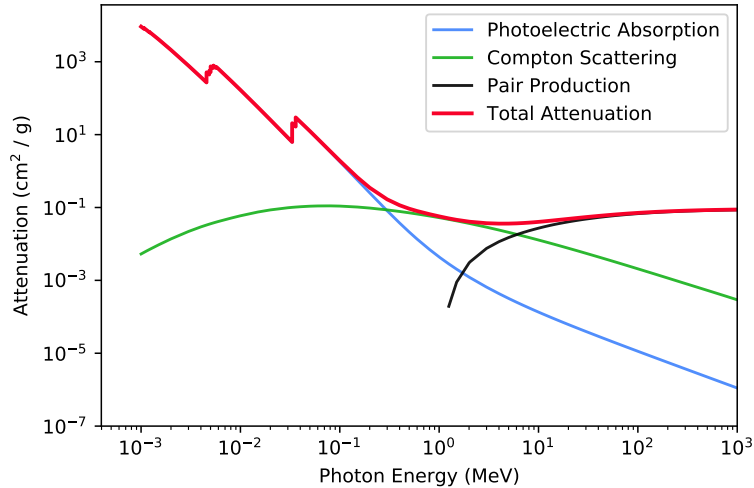
Figure 3.11: X-ray absorption mechanisms in CsI:Tl.

with thallium to produce CsI:Tl, which emits a spectrum of light centred around 550 nm
[117].

Key characteristics of scintillators include the brightness, measured in photons/MeV;
the decay time, i.e. how long the material 'glows' for after irradiation; and the attenu-
ation profile, which determines the energy range the material is useful for. All of these
parameters depend on the exact quantities of the dopant used, which varies between
manufacturer (and is considered a trade secret). Therefore, values quoted in literature
may be inconsistent.

Absorption Mechanisms

X-rays incident on a scintillator material will be attenuated according to the Beer-
Lambert law. For an initial, mono-energetic X-ray beam of intensity I_0, the transmitted
intensity I is,

$$I = I_0 e^{-\mu x}, \tag{3.13}$$

where x is the length of material in the propagation direction, and μ is the attenu-
ation coefficient. The value of μ for a given material and photon energy has contri-
butions from several processes, namely photoelectric absorption, Compton scattering
(Sec. 2.5.2), and pair production.

The relative contributions from each process are illustrated in figure 3.11. All of
these processes produce secondary electrons which are themselves able to cause further

excitation in the material. The result of this is that a single photon may generate many scintillation events.

Values of μ are tabulated for many common materials and can be found using online resources such as the NIST XCOM database [118]. This makes it straightforward to estimate how much scintillating material is necessary for a particular X-ray source.

Spectral Retrieval Using Scintillators

Often we wish to measure the spectral characteristics of an X-ray source to diagnose a laser-plasma interaction. In Chapter 4 we will discuss measurement of radiation reaction effects, and in Chapter 5 we will see how a bremsstrahlung source may be used to radiograph industrial samples. Both of these cases require knowledge of X-ray radiation spectra. We can achieve this using scintillators, with some caveats.

Unlike electron spectrometry, where we can easily determine the energy of electrons by observing how they are deflected, X-ray absorption is stochastic. This means that we cannot simply observe a length of scintillator material and obtain the energy of incident photons by the penetration depth. We can, however, make use of a Monte Carlo simulation package such as GEANT4 [119], which enables the user to accurately model the response of a detector to incident radiation.

A major challenge of this approach is that we generally require quantitative information about the interaction which produces the X-rays. For example, in generating a bremsstrahlung source with LWFA electrons, we need to know the spectral characteristics of the electrons in order to retrieve the X-ray spectrum. However, we cannot directly measure the electron beam on-shot as we must disrupt it in order to generate the X-rays in the first place. This will be discussed further in Chapters 5 and 6.

3.5 Particle-in-Cell Simulations

Modelling of laser-plasma interactions is challenging since the conditions are often far from thermal equilibrium, which necessitates a kinetic approach. The large number of particles involved ($\sim 10^{18}$ for LWFA) makes it infeasible to simulate the motion of individual particles computationally in even one dimension. In fact, we are often
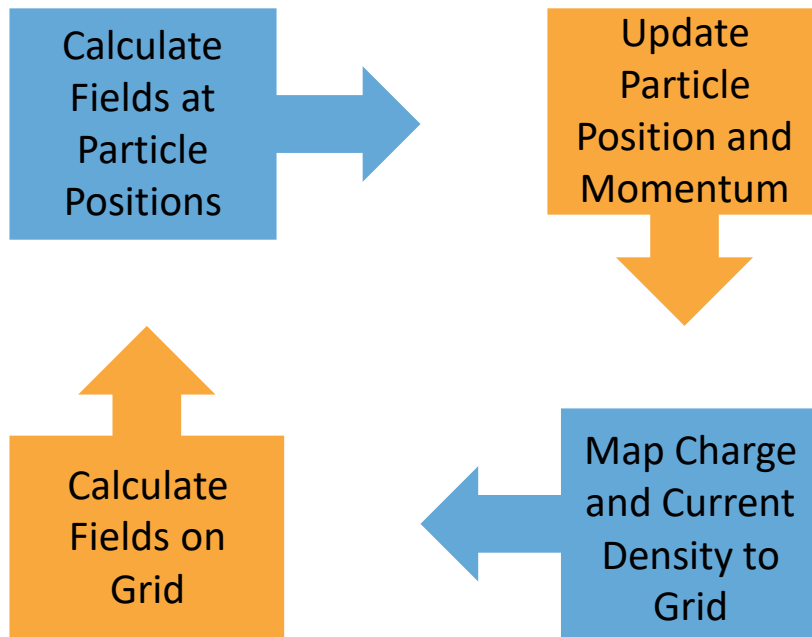
Figure 3.12: Particle in Cell method of plasma simulation

interested in a full 3D3V[1] description of the evolution of the system. We can however approximate the behaviour by noting that the Lorentz force governing the motion depends only on the charge-to-mass ratio. Thus we can simulate a much smaller number of 'macro-particles', each of which represents a potentially-large number of 'real' particles.

As for the fields, they are calculated on a grid of points, or nodes, using Maxwell's equations in a discretised form, i.e. temporal derivatives are replaced with division by a finite element such that,

$$\frac{\partial x}{\partial t} \rightarrow \frac{x_{t+1} - x_t}{t_1 - t_0} = \frac{\Delta x}{\Delta t} \tag{3.14}$$

This approach of simulating macro-particles in an array of grid points is known as the 'particle-in-cell' (PIC) method.

In Chapter 4, the simulations were conducted using the open-source PIC code, EPOCH [120]. The implementation details are broadly similar between codes, and so the following discussion will apply to PIC codes in general, but with some details specific to EPOCH.

The PIC method consists of a series of steps which are followed at each timestep: First the fields at each grid point are calculated from the particle positions and velocities. Next, the forces on the particles due to the fields are evaluated, and the particles

---

[1]3 spatial and 3 velocity (momentum)

are moved accordingly. This phase is usually referred to as the 'particle push' and in EPOCH uses the Boris method [121]. Having updated the positions and velocities of the particles, the new field configuration is calculated, and the process repeats.

The electromagnetic fields in EPOCH are calculated using the FDTD method [122], where the electric and magnetic fields are evaluated on separate grids separated by half a cell width. Such a configuration is chosen to improve numerical stability. In this scheme, the fields are calculated at each *half* timestep.

3.5.1 Choosing a Timestep

To maintain numerical stability of the simulation, the timestep Δt must be chosen appropriately. Specifically, information cannot propagate through the simulation domain at a rate of more than one grid cell per timestep. In the case of EM waves, this means the (1D) grid size Δx must be strictly greater than $c\Delta t$. In 3D, this condition is

$$\sqrt{(\Delta x^2) + (\Delta y^2) + (\Delta z^2)} > c\Delta t. \tag{3.15}$$

The timestep constraint is known as the Courant-Friedrich-Lewy (CFL) condition [123]. Typically, end-users of PIC codes do not need to account for this, as the appropriate timestep is calculated for the specified grid size.

3.5.2 Numerical Dispersion

An unfortunate consequence of discretising Maxwell's equations is that electromagnetic waves do not obey the correct dispersion relation[1]. Rather, a given numerical scheme will have its own relation which is derived from the discretised equations. In the case of the FDTD (Yee) method, the dispersion relation is [124]

$$\begin{aligned}
\left(\frac{1}{c\Delta t}\right)^2 \sin^2\left(\frac{\omega\Delta t}{2}\right) &= \left(\frac{1}{\Delta x}\right)^2 \sin^2\left(\frac{k_x\Delta x}{2}\right) \\
&+ \left(\frac{1}{\Delta y}\right)^2 \sin^2\left(\frac{k_y\Delta y}{2}\right) \\
&+ \left(\frac{1}{\Delta z}\right)^2 \sin^2\left(\frac{k_z\Delta z}{2}\right)
\end{aligned} \tag{3.16}$$

---

[1]An analogous effect occurs for diffusion in fluid simulations.
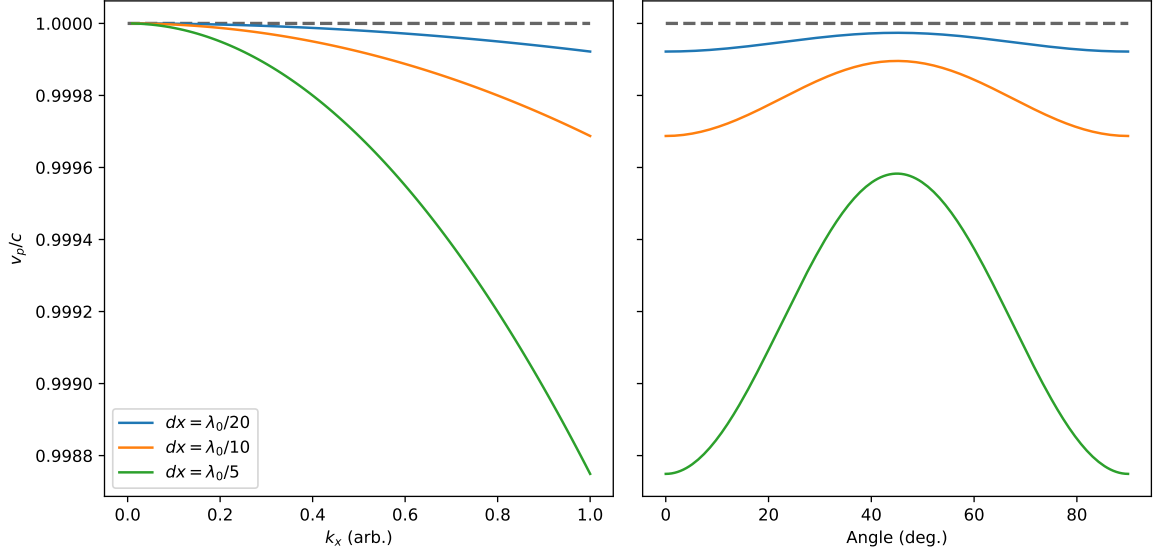
Figure 3.13: Numerical dispersion relation for various grid resolution values. Dotted line is the correct relation.

It is clear that (3.16) reduces to the standard vacuum expression $\omega^2 = c^2 |\boldsymbol{k}|^2$ in the limit $\Delta x = \Delta t \to 0$.

The effect of numerical dispersion on the propagation of EM waves is illustrated in Figure 3.13. High frequency waves in particular travel with a velocity $v < c$. Additionally, the angle of wave propagation with respect to the grid affects the dispersion. A 45° angle minimises the effect of numerical dispersion for given values of dx and k. In general however, unless computational power is at a premium, increasing spatial resolution is a better way to mitigate numerical dispersion than changing the angle of incidence.

3.5.3 Electron Beams in EPOCH

Typically EPOCH is used to simulate plasma effects such as LWFA, and as such the simulation domain is filled with electrons and ions[1]. It is also possible to simulate a custom distribution of particles, such as a beam of electrons moving through vacuum (see Chapter 4), by using the manual particle loader. An example can be found in the EPOCH user manual [125].

---

[1]To save computation power, a neutralising background is often used in place of the ions, which are generally assumed to be stationary over short (fs) timescales.

3.5.4 Implementation of QED Effects

Quantum effects such as photon emission, pair-production, and radiation reaction are implemented in EPOCH (and other codes [126]) using a Monte Carlo approach. For the purposes of this thesis, we shall neglect the discussion of pair production, but the implementation strategy is similar to that of other quantum processes. The following discussion of the Monte Carlo method draws on the work of Duclous *et al.* [127]. A description of the implementation in EPOCH specifically is given by Ridgers *et al.* [128].

An electron in a weak, locally-constant[1] electromagnetic field emits photons at a rate given by [95, 97]

$$\frac{d^2 N}{d\chi dt} = \frac{\sqrt{3}}{2\pi\tau_C}\alpha_f\frac{\eta}{\gamma}\frac{F(\eta,\ \chi)}{\chi} \tag{3.17}$$

where $F(\eta,\ \chi)$ is the quantum synchrotron function.

To account for the stochasticity of the emission, that is the straggling effect (Sec. 2.6.3), the probability P of photon emission is described in terms of an optical depth term, τ,

$$P = 1 - e^{-\tau}. \tag{3.18}$$

An electron at the start of the simulation is assigned an optical depth of zero, and a pseudo-randomly generated *final* optical depth, τ_f. As it propagates, the optical depth is updated at each timestep according to the equation,

$$\frac{d\tau}{dt} = \int_0^{\eta/2}\frac{d^2 N}{d\chi dt}\left(\eta,\ \chi\right)d\chi. \tag{3.19}$$

When $\tau = \tau_f$, a photon is emitted with an energy given by

$$\hbar\omega = \frac{2m_e c^2 \chi_f \gamma}{\eta}, \tag{3.20}$$

where the value of χ_f is found from the following relation,

$$\xi = \frac{\int_0^{\chi_f}(F(\eta,\ \chi)/\chi)d\chi}{\int_0^{\eta/2}(F(\eta,\ \chi)/\chi)d\chi}. \tag{3.21}$$

Here, $\xi \in [0, 1]$ is a uniformly-distributed pseudo-random value generated at the time of

---

[1]The precise meaning of these terms is defined below.

emission. The value of χ_f is found from pre-calculated lookup tables for computational efficiency.

Range of Validity

The method described relies on two approximations to simplify calculation. The first is that the background field, i.e. the laser, is slowly varying compared to the interaction time (e.g. photon emission). This allows the laser field to be treated as constant at the location of the interaction, and corresponds to the condition [93]

$$a_0 \gg 1. \tag{3.22}$$

The second approximation made is that the probabilities associated with photon emission and pair production depend only on η. For arbitrary field strengths, the probabilities depend not only on η, but also on the field invariants [34]

$$
\begin{aligned}
F &= \frac{E^2 - B^2}{E_{crit}^2}; \\
G &= \frac{|\boldsymbol{E} \cdot \boldsymbol{B}|}{E_{crit}^2}.
\end{aligned}
\tag{3.23}
$$

However, in the limit $F, G \ll 1$, and $\eta^2 \gg \mathrm{Max}(F, G)$, this dependence may be neglected [95].

3.5.5 Summary

In this chapter we have discussed various techniques used to diagnose laser-wakefield accelerators, as well as some useful analysis techniques. We have also seen how the particle-in-cell method allows for simulation of laser-plasma interactions, and in particular the implementation of QED effects into PIC codes such as EPOCH.

The main results of the thesis will be presented in the following three chapters.

Chapter 4

Single-Shot Measurements of Radiation Reaction

"...the problem of radiation reaction effects emerges like a lost relative expecting an inheritance. We are the nervous relatives gathered about, not sure what to do with him. In the past, he was sometimes considered a curiosity, the importance of whom obviated by his unreachability. But now he is at our doorstep, knocking, and we must admit this unwelcome visitor and let him enter into our equations and into our labs." - R. T. Hammond EJTP 7, No. 23 (2010) p222

4.1 Introduction

Improvements in laser technology such as CPA and parametric amplification have accelerated the drive towards higher peak intensities. Along the way several significant applications have been realised, for example, compact acceleration of electrons (LWFA), ion acceleration, and high-brightness photon sources. Modern lasers are capable of recreating conditions found in the depths of space in the laboratory, allowing detailed investigation of astrophysical phenomena: Brown dwarf stars, pulsars, and supernovae, to name a few.

Electrons are accelerated by the electromagnetic field of a laser, resulting in the emission of synchrotron radiation. By conservation of energy, the emission of radiation by an electron must result in a corresponding change in its own kinetic energy.

This can be described as a recoil, or reaction force on the electron, and is commonly termed 'radiation reaction' (RR). Despite the solid foundation of energy conservation, a physically consistent description of RR proved elusive for almost a century. Efforts by Abraham, and later Dirac, proved problematic, with solutions predicting runaway acceleration and acausality.

In all but the most intense laser fields, RR is insignificant compared to the Lorentz force and can be safely ignored. However, in strong electric fields, where the field in the electron's rest frame approaches the Schwinger limit, radiated photons can carry off an appreciable fraction of the electron energy. In this case, the RR force becomes comparable to the Lorentz force and must be taken into account. The laser intensities currently available ($\sim 10^{21}\,\mathrm{W\,cm^{-2}}$) are insufficient to reach this regime when interacting with stationary targets, although new systems such as ELI [129, 130] and Apollon [131, 132] are expected to operate at intensities approaching, or even exceeding $10^{23}\,\mathrm{W\,cm^{-2}}$. Electron motion at this intensity will be dominated by recoil forces, necessitating a precise description of RR in order to fully understand the interactions.

Radiation reaction effects have been shown to interfere with processes like ion acceleration and X-ray production that would otherwise scale positively with intensity [58, 133]. Compton backscattering sources, for example, would be depleted by RR effects as laser energy is lost to pair cascades. Similarly, the energy of ions accelerated, and the efficiency of the process overall, is reduced by such effects [134, 135].

Since the significance of RR effects is determined by the electric field in the rest frame of the electron, the relativistic Doppler effect can be exploited to reach a regime where RR is important with a much lower intensity. The geometry of inverse Compton scattering is ideal for maximising RR effects: In a recent experiment on Astra-Gemini, Cole *et al.* observed electron energy loss after collision with a laser pulse of intensity $5 \times 10^{20}\,\mathrm{W\,cm^{-2}}$ [42]. However, pointing fluctuation in both the electron beam and colliding laser conspired to limit the successful collisions to just four. A detailed statistical analysis confirmed the observation of radiation reaction, but there was insufficient data to compare the classical and quantum predictions.

In order to improve upon the results of Cole *et al.*, two options present themselves immediately: The first is to mitigate the pointing fluctuation of the laser, to increase the collision probability. Since these results were published, a beam stabilisation system
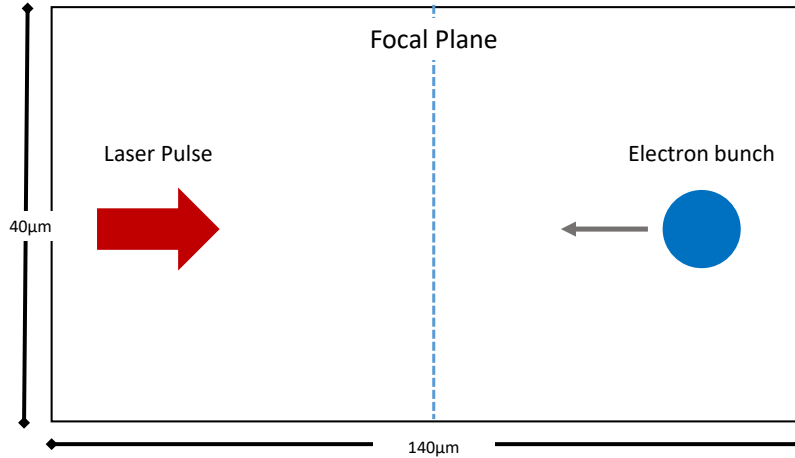
Figure 4.1: Schematic of the interaction in the simulation domain. An electron bunch collides with a counterpropagating laser pulse in the focal plane.

has been implemented in Gemini at the Central Laser Facility. As of writing, its effectiveness in QED experiments has yet to be tested.

The second is to attempt an on-shot measurement of the electron energy loss, obviating the statistical analysis in favour of a direct comparison of the electron spectrum before and after the collision. This chapter will detail a study into the feasibility of such single-shot measurements of RR using the Gemini system (or one similar, such as Hercules) by using an electron bunch which is larger than the colliding laser pulse, such that regions of the bunch remain unperturbed after the interaction.

The results presented were obtained from simulations using the 3D3V particle-in-cell code, EPOCH (Sec. 3.5) (Version 4.17.12). Simulations presented here were run using the Viking HPC cluster based at the University of York, and the SCARF HPC cluster at the Rutherford Appleton Laboratory.

4.2 Simulation Setup and Initial Conditions

The simulation domain was set up to replicate an inverse Compton scattering geometry at $180°$ angle of incidence, in the same manner as the experiment described in Cole *et al.* (figure 4.1). The initial conditions of the simulations were chosen to represent those attainable on the Astra Gemini laser.
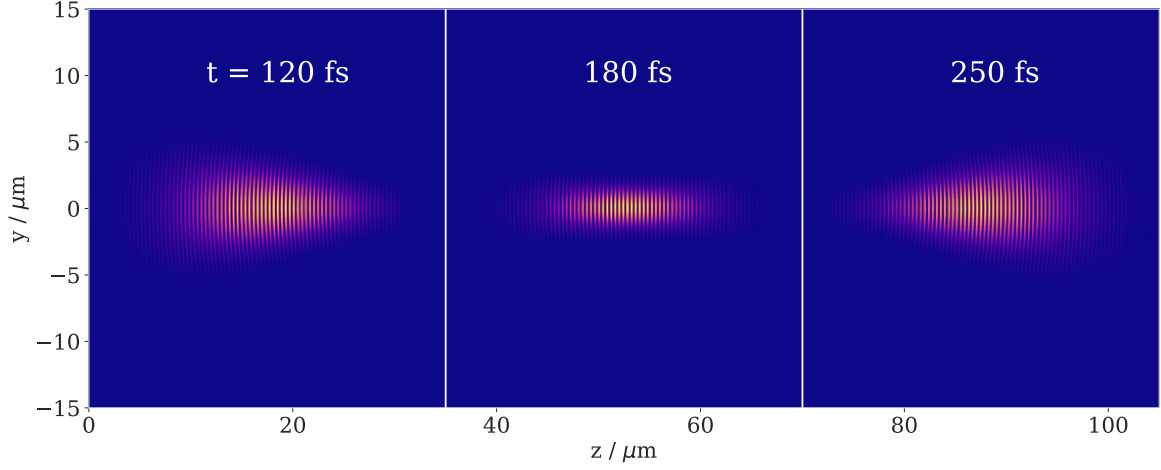
Figure 4.2: Temporal evolution of the laser pulse.
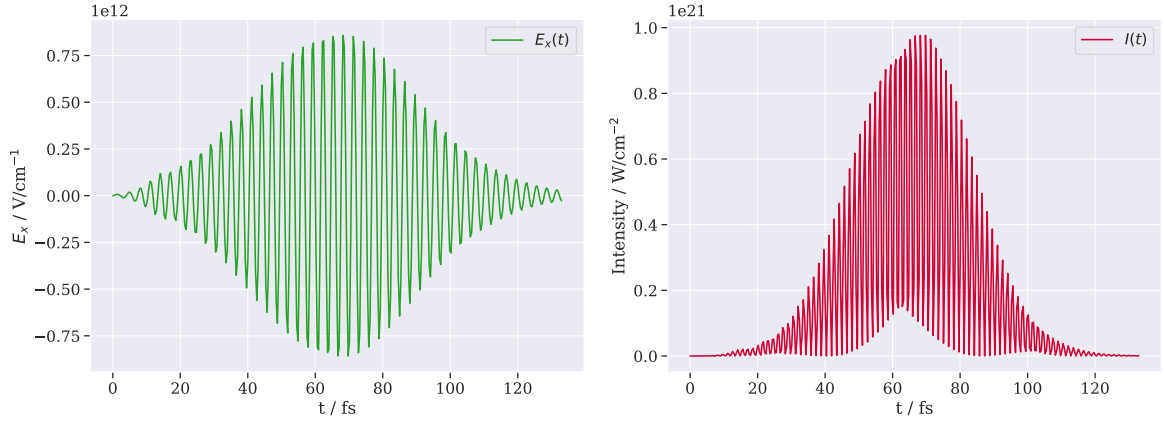
Figure 4.3: Temporal shape of the laser pulse. Left: Component of electric field in polarisation direction. Right: Corresponding intensity profile. The pulse duration (defined by the FWHM width) is 44 fs.

4.2.1 Laser Pulse

The laser pulse was chosen to be an 800 nm wavelength, Gaussian (TEM-00) mode focussed to a spot size of 2 µm (i.e. the diffraction limit of an F/2 focusing optic), with a peak intensity of 1×10^{21} W cm^{-2} ($a_0 \simeq 21$) in the focal plane, and polarised along the x direction. The initial pulse was defined to propagate into the simulation domain from the edge corresponding to z_{min}, focussing 40 µm from the edge. Fig. 4.2 shows the evolution of the pulse width and peak intensity as a function of propagation distance z.

A Gaussian profile of width 44 fs (FWHM) was chosen to represent the temporal shape of the pulse. The normalised intensity of the pulse is shown in Fig. 4.3. Laser

parameters were held constant for all results presented in this chapter.

4.2.2 Electron Bunch
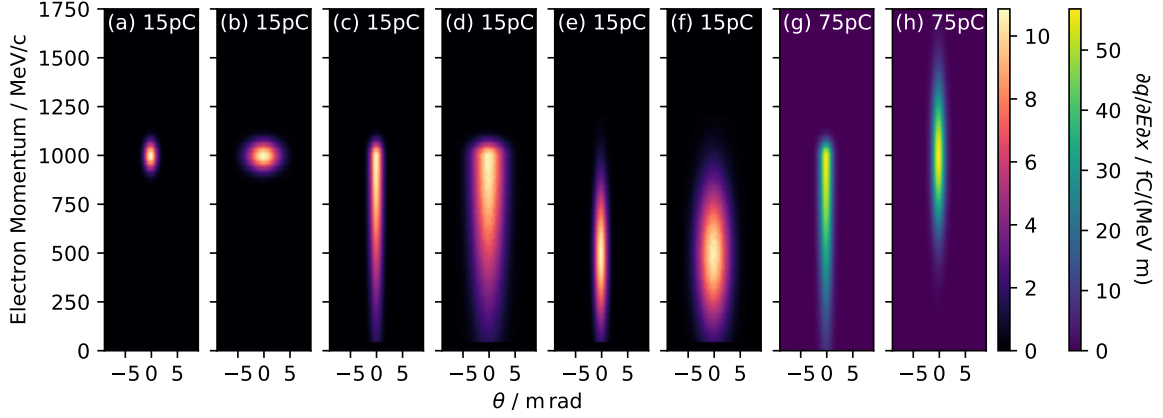
Figure 4.4: Synthetic screens showing the range of electron beams used for this work. Beams in (g) and (h) contain higher charge, and so are represented on a separate colour scale.

The parameter space of possible electron bunch characteristics is far too broad to fully explore, so instead we have chosen eight 'styles' of electron beam which represent those commonly observed under experimental conditions. These are shown in Figure 4.4 (a)-(h), and described in more detail in Table 4.1. In all cases, the electrons are spatially distributed in a 3D Gaussian shape with FWHM of 5 μm in all directions.

	E_0	σ ($\sigma_{low} : \sigma_{high}$)	N (q)	θ_{div}	Description
(a)	$1.0\,\mathrm{GeV}$	$50\,\mathrm{MeV}$	1×10^8 (15 pC)	$2\,\mathrm{mrad}$	Narrow GeV (2mrad)
(b)	$1.0\,\mathrm{GeV}$	$50\,\mathrm{MeV}$	1×10^8 (15 pC)	$5\,\mathrm{mrad}$	Narrow GeV (5mrad)
(c)	$1.0\,\mathrm{GeV}$	$(50 : 500)\mathrm{MeV}$	1×10^8 (15 pC)	$2\,\mathrm{mrad}$	Tail GeV (2mrad)
(d)	$1.0\,\mathrm{GeV}$	$(50 : 500)\mathrm{MeV}$	1×10^8 (15 pC)	$5\,\mathrm{mrad}$	Tail GeV (5mrad)
(e)	$0.5\,\mathrm{GeV}$	$250\,\mathrm{MeV}$	1×10^8 (15 pC)	$2\,\mathrm{mrad}$	Broad 500 MeV (2mrad)
(f)	$0.5\,\mathrm{GeV}$	$250\,\mathrm{MeV}$	1×10^8 (15 pC)	$5\,\mathrm{mrad}$	Broad 500 MeV (5mrad)
(g)	$1.0\,\mathrm{GeV}$	$(50 : 500)\mathrm{MeV}$	5×10^8 (75 pC)	$2\,\mathrm{mrad}$	Tail GeV (75pC)
(h)	$1.0\,\mathrm{GeV}$	$250\,\mathrm{MeV}$	5×10^8 (75 pC)	$2\,\mathrm{mrad}$	Broad GeV (75pC)

Table 4.1: Summary of electron beam parameters used in this chapter. (c), (d), and (g) are asymmetric in p_z, so the σ values both above and below the 'mean' are given. The labels in the "Description" column will be used as a convenient reference to each parameter set throughout.
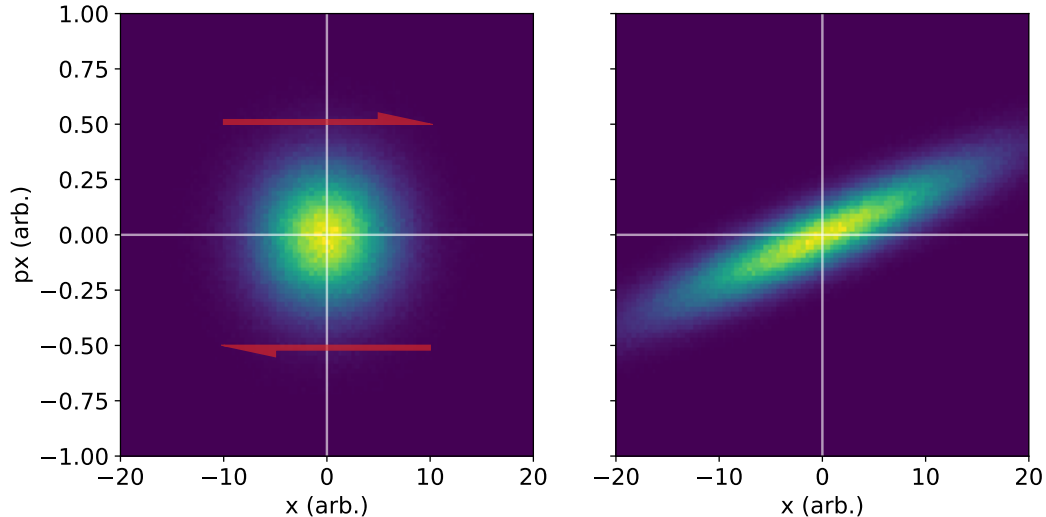
Figure 4.5: Phase space correlation of electrons increases as they propagate. Left: Initially uncorrelated $x - p_x$ phase space. Right: After propagation.

4.2.3 Pre-Interaction Propagation

The following results are based on varying the distance the electron beam travels before collision with the laser pulse. This could be achieved directly by changing the size of the simulation domain, however the computational cost would be prohibitive. An alternative method is to extrapolate each particle's trajectory and reposition it according to its momentum, with the result that those particles with the largest transverse momentum (i.e. the largest divergence angle) are positioned towards the edges (in doing this, we are ignoring space-charge effects which are negligible on such timescales for highly-relativistic particles. See Sec. 4.5.4).

To calculate the new position of the particle, we take its current position and the angle of its momentum vector and extrapolate using similar triangles, i.e.,

$$x_{new} = x_{old} + d\frac{p_x}{p_z}. \tag{4.1}$$

One consequence of this propagation, or 'drift', is a correlation in the electron phase space between x, the particle position, and p_x, the transverse momentum[1]. As illustrated in Figure 4.5, the particles with the largest transverse momentum tend towards the edges of the bunch. In the limit of infinite propagation, the phase space becomes

---

[1]The same occurs in the y-axis.

perfectly correlated. We shall now see how this approach affects the measurement of radiation reaction effects.

4.3   Results and Analysis
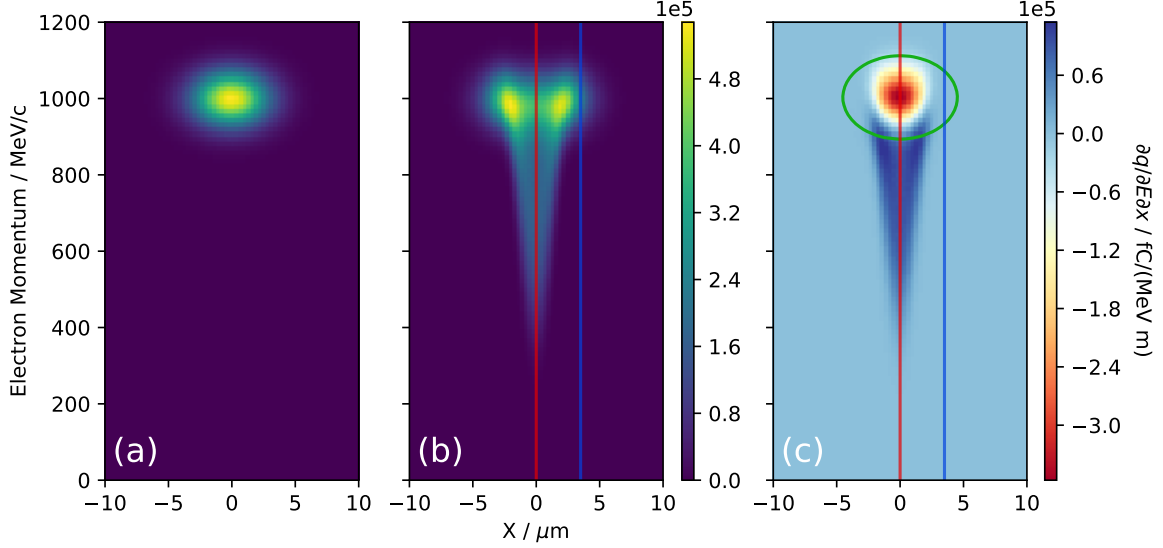
Figure 4.6: Electron beam showing signature of RR. Vertical axes show electron forward momentum p_z. Horizontal axes indicate spatial scale in x-direction. (a) Pre-interaction bunch. (b) Post-interaction. The central profile (red) shows the strongest signature of RR, whereas the edge (blue) is outside the interaction zone and so remains unchanged. (c) Difference between post- and pre- interaction plots $((b) - (a))$ Highlighting where electrons have been displaced.

Each of the electron beams described above was used in a simulated collision with a laser pulse to elicit radiation reaction. We start with our "Narrow GeV" beam.

Using synthetic spectrometer screens allows us to determine the effect on the electron beam properties. In Figures 4.6 (a) and (b) we see the state of the electron bunch immediately before, and immediately after the collision. The region in the centre of the bunch has interacted most strongly with the pulse, with energy shifts down to around 300 MeV. On either side of the central portion we observe energy loss to a lesser degree, due to the transverse intensity gradient of the laser pulse. Finally, at the extreme edges there is little to no energy loss. Figure 4.6 (c) is the difference between the previous two figures $(I_{(a)} - I_{(b)} = I_{(c)})$, and highlights regions where electrons have been displaced. With the shape of the original bunch overlaid in green, it can be seen that the edge regions retain the original characteristics.

75
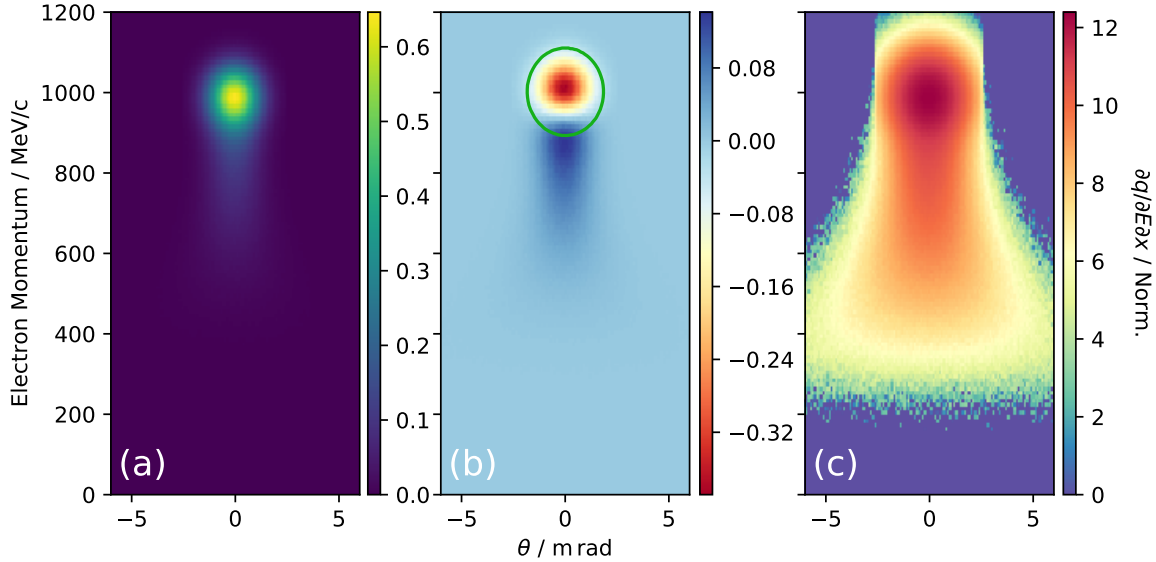
Figure 4.7: Effect of 1 m post-interaction propagation. Horizontal axes now represent angle, rather than spatial position. (a) Synthetic spectrometer screen. Electron beam shows faint tail as a result of laser interaction. (b) Difference between (a) and a 'control' bunch with no laser interaction. Green circle shows outline of original bunch and indicates that no 'edge' region containing the original spectrum remains. (c) Same as (a) on logarithmic colorscale to emphasise displacement of electrons, and absence of useful edge regions.

These two key regions of the bunch contain the spectral information before *and* after the interaction. This is precisely what we require to assess the effect of radiation reaction. But first we have to measure it.

One of the key experimental diagnostics for RR experiments is an electron spectrometer (Sec. 3.2.1): Electrons are dispersed by a magnetic field and strike a scintillating screen. The dispersion process is what enables us to resolve the spectral components of the electron bunch, and requires a substantial post-interaction distance (typically on the order of 1 m). In order to detect RR experimentally, the spatial structure observed in the simulation must be preserved as the electrons propagate to the screen.

Using the same propagation method outlined in the previous section, we can calculate the evolution of the x-p_z phase space using the individual particle positions and momentum components. At a distance of 1 m the electron bunch bears only a slight resemblance to its post-interaction state. Figure 4.7 (a) shows the electron beam with a faint tail extending to around 600 MeV, and without the characteristic 'V' shape observed in Fig. 4.6 (b). The adjacent plot 4.7 (b) is the difference between interacted electron beam and its pre-interaction counterpart where we again see that electrons

76

have been displaced into lower energy parts of the phase space. Crucially, however, the well-defined centre and edge regions we identified earlier are no longer present. With the original beam shape overlaid in green, we see that no part of the propagated bunch contains the original spectrum. Figure 4.7 (c) shows (a) on a logarithmic scale for clarity. Here it is apparent that the electrons which have interacted with the laser have been shifted to lower energies, but also given a lateral 'kick' into the edges of the phase space.

As an aside, we note that this angular spreading of electrons is itself a signature of radiation reaction [136], however it does not allow us to recover the original spectrum, which is our main objective.

4.3.1 Effect of Drift

We saw above that propagating the electron beam to the spectrometer blurred out the signature of RR such that we could no longer recover the original spectrum. The reason for this is that the position (x, y) of the particles and their transverse momenta $(p_x, p_y \propto \theta_{div})$ are uncorrelated, meaning their trajectories intersect as they travel in z. Put another way, the particles in the centre of the bunch, i.e. where the laser passes, do not remain there. Since they have the same distribution of momenta as the rest of the bunch, they end up spread across the entire angular range at large distances.

If we can introduce a correlation into the x-p_x space, the electrons in the interaction zone will remain there as they propagate. Equally, those outside the interaction region will not intrude on it at the spectrometer screen. A pre-interaction drift is precisely the way to do this. As we saw above, it is useful to look at the difference between the post-interaction and pre-interaction electron bunches. The resulting 2-dimensional map shows clearly where electrons have been displaced, where they end up, and where they do *not* end up.

With no initial drift, we see from Figure 4.8 (top) that electrons are shifted into lower energy regions where they were not present before (We are still working with the "Narrow GeV (2 mrad)" configuration). Figure 4.8 (bottom) shows the 1D charge density along the corresponding lines in the top plot. We see a lower, but non-zero, signal 1 mrad from the centre.

The next step is to include a millimetre-scale pre-interaction drift and look at the
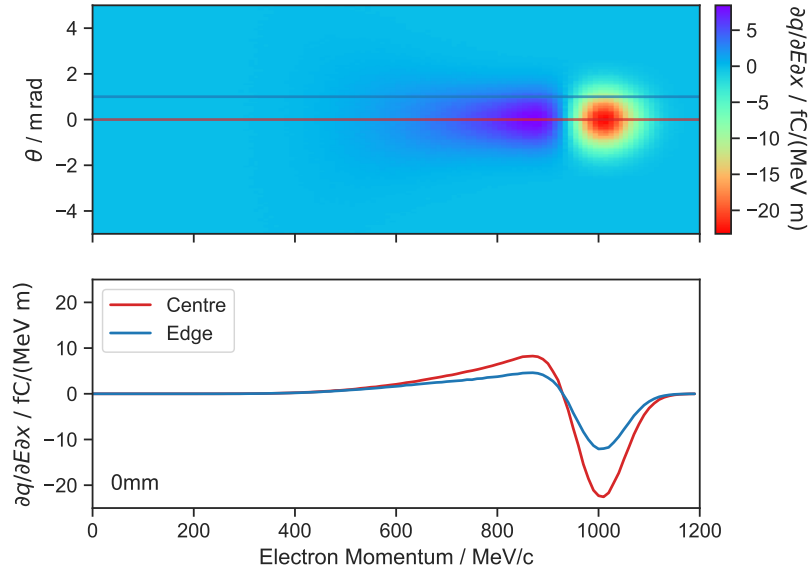
Figure 4.8: Electron displacement with 0 mm drift. Top: Difference between 'test' and 'control' conditions, i.e. 'laser on', and 'laser off'. Centre (red, 0 mrad) and edge (blue, 1 mrad) sampling areas marked. Bottom: Plot of sampling areas marked above. Both centre and edge retain signature of RR.

same centre and edge regions as before. Figure 4.9 shows the effect for 2 mm, 5 mm, and 10 mm. Along the top, the three 2D difference maps show a progressively narrowing region of displacement as the drift distance increases. Additionally, with the plots on the same intensity scale, we can see that there is an overall decrease in signal level with longer drifts. This is clearer in the bottom row, again on the same scale, where the difference between the 'test' bunch and its 'control' decreases with drift distance.

The key observation here is that between 5 and 10 mm the width of the displacement zone is less than 1 mrad, where we took our edge measurement. In Figure 4.9 (c) the signal at the edge is zero everywhere, indicating that this region is identical to the original spectrum.

If we increase the drift further, we expect that the signal at the centre will also drop to zero, making measurement impossible. We should therefore expect that there is some optimum drift distance which will maximise the signal in the centre, while preserving the original spectrum at the edges. To find this optimum, and moreover to make some quantitative predictions, we must first address some experimental factors which we have ignored thusfar.
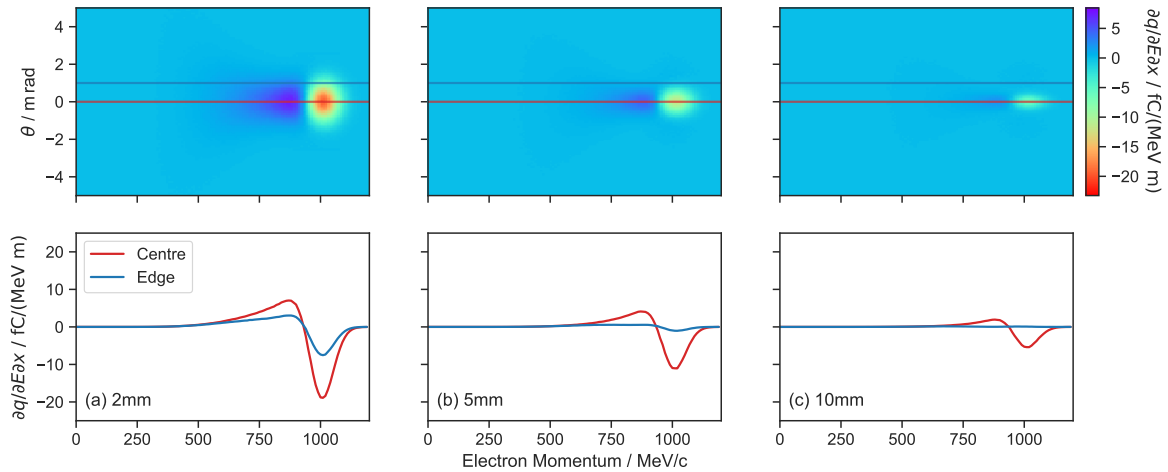
Figure 4.9: Effect of drift on sampling regions. Top: Test vs. control with sampling areas marked. Bottom: Sampling area profiles for (a) 2 mm, (b) 5 mm, (c) 10 mm. Edge signal at 10 mm indicates that it retains original, pre-interaction spectrum.

4.3.2 Further Experimental Considerations

So far we have explored the effect of including a drift to the electron bunch before the interaction. To successfully measure this experimentally we must consider some possible limitations.

A typical electron spectrometer setup for LWFA relies on a scintillating screen made of phosphor-coated plastic (Lanex). Light emitted by the screen upon exposure to charged particles is then captured by an imaging system. Both the light yield from the screen itself and the collection efficiency of the imaging system contribute to a minimum signal level that can be detected by the system. It is impossible to quantify the collection efficiency of an arbitrary imaging system, so we will neglect this for now, and consider only the detection capabilities of the scintillator.

Work by Buck *et al.* [107] explores the charge sensitivity of a range of phosphor-based scintillators. The most sensitive has a minimum detection threshold of $10\,\mathrm{fC\,mm^{-2}}$. We shall use this reference value going forward. The geometry of the spectrometer itself is also important. Parameters such as magnetic field strength, length of the magnet, distance to the screen, and the angle of the screen all influence the signal. Increasing the field strength, for example, increases the dispersion angle and so improves energy resolution. Consequently, the charge density at a particular energy will decrease, how-ever. Figure 4.10 shows how the vertical position on a scintillating screen varies with electron energy. We assume here that the screen is oriented vertically with respect
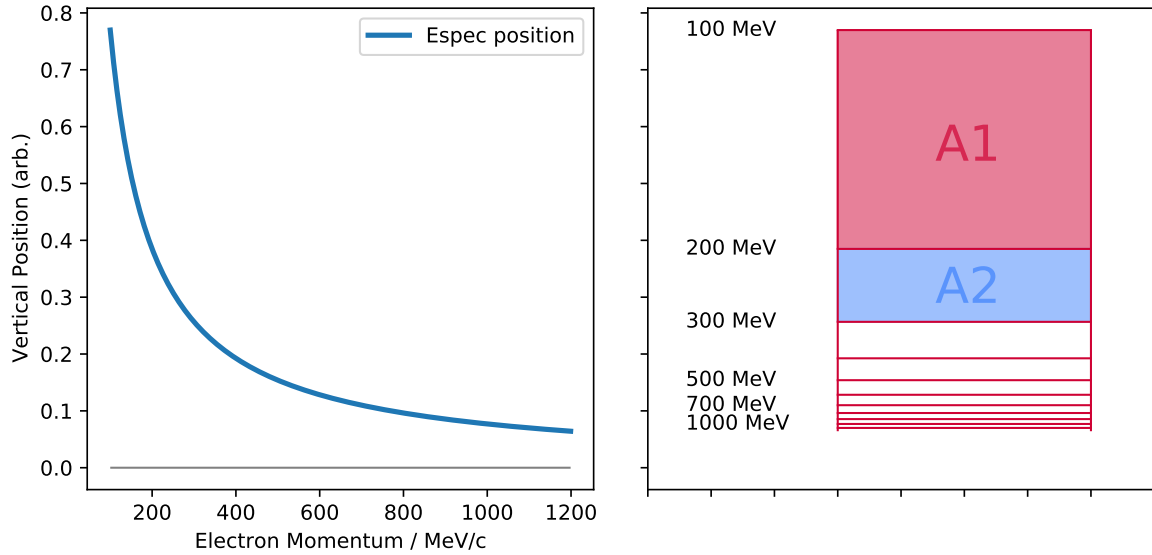
Figure 4.10: Electron spectrometer calibration (idealised). Left: Vertical position as a function of electron energy. $y \propto 1/p_z$. Right: 2D schematic of spectrometer screen. Energy bin sizes increase towards lower energy. Areas marked 'A1' and 'A2' have the same width in energy, but different spatial scales. Areal charge density in each bin will be lower in 'A1' for the same overall charge. Detection is therefore more difficult for lower energy electrons.

to the incoming electron beam (pre-dispersion), and also that the magnetic field is uniform between the poles, and zero elsewhere.

The position on the screen is inversely proportional to the energy, and so the area of each energy bin (Fig. 4.10 right) decreases with electron energy. If we wish to detect electrons at low energies, we therefore require more charge to do so.

In the following analysis, we will consider how this finite detection threshold impacts our ability to measure radiation reaction effects.

4.3.3 Effect of Electron Beam Divergence

We have identified that the charge density in the electron beam is a factor in whether RR effects can be measured. In particular, due to the reciprocal behaviour of electron dispersion, signal will be harder to detect in lower energy regions of the spectrum.

The divergence of the electron beam is also important to consider. There are two reasons for this. First, for a given beam charge, a more divergent electron bunch will be dimmer on a Lanex screen. Secondly, the x-p_x phase-space correlation we seek will develop more quickly in divergent beams. A shorter drift distance should then
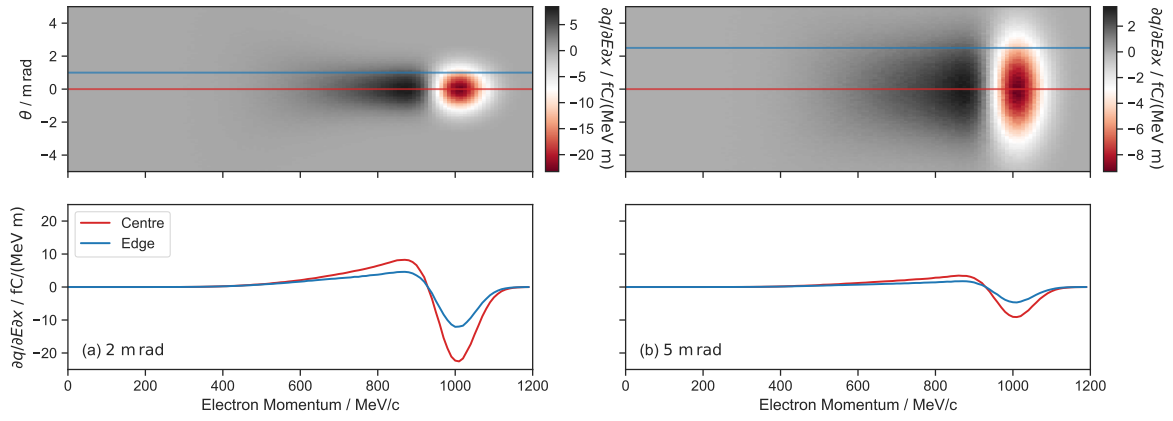
Figure 4.11: Narrow GeV beam with (a) 2 mrad and (b) 5 mrad FWHM divergence. Top: Test vs. control with 0 mm drift. Bottom: Signal in sampling regions. Edge is sampled at (a) 1 mrad and (b) 2.5 mrad.
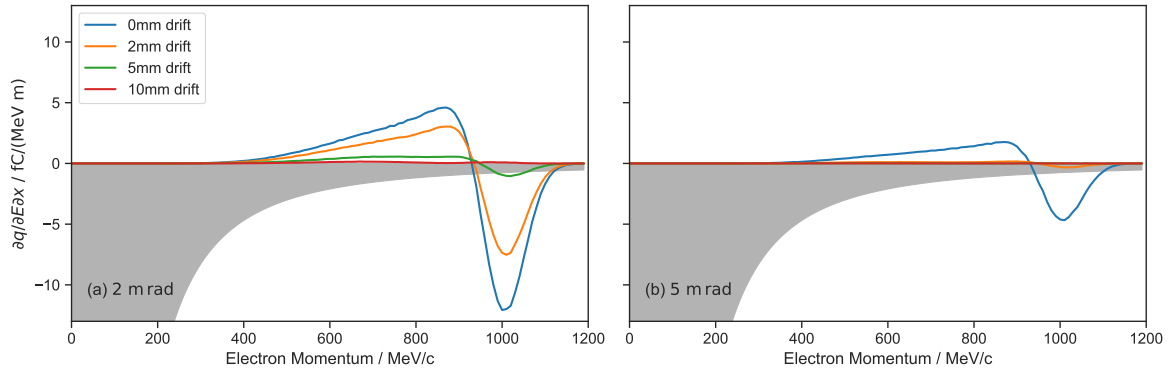
Figure 4.12: Edge signal levels for various pre-interaction drift values. (a) 2 mrad. (b) 5 mrad. Edge level drops below detection threshold between 5 mm and 10 mm drift in 2 mrad case. Overall signal level is lower in the 5 mrad case for all values of drift, and drops below detector limit between 0 mm and 2 mm. Detector limit (grey region) calculated from electron spectrometer calibration described in previous section, and sensitivity measurements taken by Buck *et al.*

be required to isolate the displacement region in the centre. Figure 4.11 shows the difference between "Narrow GeV" configurations of 2 and 5 mrad. In both cases we take 1D samples at the centre and at the edge position corresponding to the half-max of the initial bunch, i.e. 1 mrad and 2.5 mrad. This comparison at 0 mm drift suggests already that the more divergent beam will be harder to measure. The signal at the centre is around half that of the 2 mrad case, and the centre and edge signals are closer in magnitude. Looking only at the edge regions, and including the detection threshold of $10 \, \mathrm{fC \, mm^{-2}}$, we see in Figure 4.12 that the edge signal drops below the detector limit between 5 and 10 mm in the 2 mrad case. In the 5 mrad bunch, this occurs between 0 and 2 mm, consistent with our expectations.
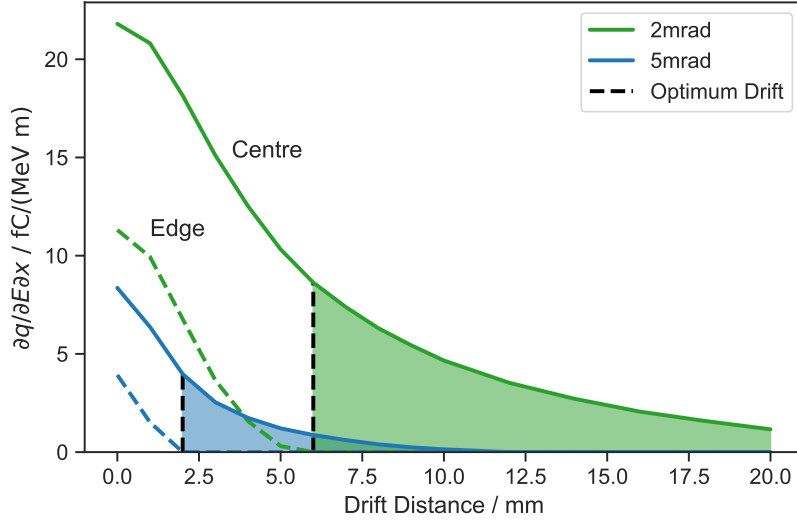
Figure 4.13: Adjusted signal S_{adj} at the centre (solid line) and edge (dashed) for $2\,\mathrm{mrad}$ (green) and $5\,\mathrm{mrad}$ (blue) "Narrow GeV" beams. The optimum occurs when the edge signal drops to zero, i.e. falls below the detector limit. Shaded regions indicate drift distances where successful measurements can be made. Optimum drift $d_{\mathrm{opt}}(2\,\mathrm{mrad}) = 6\,\mathrm{mm}$; $d_{\mathrm{opt}}(5\,\mathrm{mrad}) = 2\,\mathrm{mm}$.

4.3.4 Optimising Signal

Naturally, we are interested in maximising the signal of radiation reaction in our experiments to make definitive measurements. The existence of a detector limit is a double-edged sword in this case. On the one hand, we may find it difficult to measure signal at low electron energies. On the other, we need not reduce the edge signal to zero in order to recover the original spectrum. It is sufficient for level to be below the detector limit to ensure the post-interaction signal is practically indistinguishable from the original. This means we can get away with a shorter drift distance, which in turn boosts our signal in the centre of the bunch. To quantify this we compare the signal levels, S, that is the difference between the 'test' bunch and the 'control', to the detector limit, L_{detector}, to obtain an adjusted signal level $S_{adj} = S - L_{detector}$ in units of charge. For values of $S \leq L_{\mathrm{detector}}$, $S_{adj} = 0$, thus a non-zero value of S_{adj} represents a detectable signal, and vice-versa. The optimum drift is the minimum distance such that $S_{adj}(\mathrm{edge}) = 0$.

In Figure 4.13 the value of S_{adj} is plotted for the centre and edges of both the $2\,\mathrm{mrad}$ and $5\,\mathrm{mrad}$ "Narrow GeV" beams. The shaded areas indicate the range of drifts where measurements can be made, with the optimum marked by the black dashed line.

It can be seen that although the optimum drift occurs sooner for the more divergent
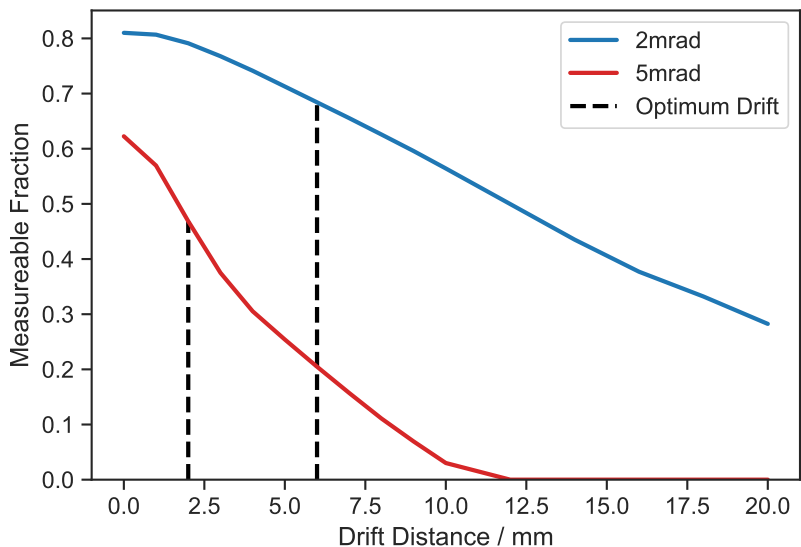
Figure 4.14: Measurable fraction of the spectrum as a function of drift distance, $f(d)$. Measurements can be made at $d \geq d_{\mathrm{opt}}$ (black dashed line). Obtained values of $f(d_{\mathrm{opt}})$ are 0.68 (2 mrad, blue), and 0.47 (5 mrad, red).

beam (2 mm as opposed to 6 mm), the 2 mrad case offers approximately twice the signal at the optimum. In addition to the optimum drift distance, we can calculate a figure of merit which takes into account the energy dependence of our detector limit. Considering S and S_{adj} for the central region, we find the ratio f as a function of the drift distance d,

$$
f(d) = \frac{\displaystyle\int |S_{adj}|\, dE}{\displaystyle\int |S|\, dE}, \tag{4.2}
$$

where E is the electron energy, and the integrals are evaluated over the whole spectrum. This quantity can be thought of as the measurable fraction of the spectrum. The relationship between $f(d)$ and the drift d is illustrated in Figure 4.14. At the optimum drift the 2 mrad and 5 mrad beams have $f(6\mathrm{mm}) = 0.68$ and $f(2\mathrm{mm}) = 0.47$, respectively.

4.3.5 Broadband Electron Beams

Now that we have established some criteria for optimising the RR signal, we can extend the previous analysis to other electron beam configurations. In the following, we will discuss the results from electron bunches with broadband spectra, specifically the "Tail GeV" and "Broad 500MeV" cases outlined in Table 4.1.
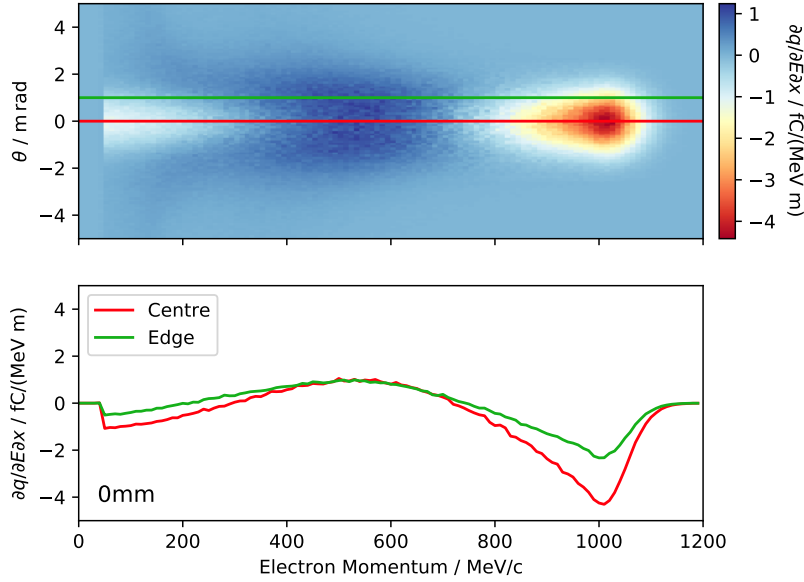
Figure 4.15: Test vs. control for "Tail GeV" beam at $d = 0\,\mathrm{mm}$. Downshifted electrons predominantly lose forward momentum, and so $\theta_{\mathrm{div}} \simeq p_x/p_z$ increases. Displaced electrons contribute to signal level at the edge, particularly around $500\,\mathrm{MeV}$.

Long-tailed GeV Beam

The 2D intensity map in Figure 4.15 (top) is, as before, the difference between the post-interaction and pre-interaction beams after a $1\,\mathrm{m}$ propagation to the synthetic spectrometer screen (no pre-interaction drift). Some interesting features are immediately apparent: Electrons have been shifted down in energy, but also laterally, increasing the divergence at lower energies. This also occurred for the previous case, but was less obvious on account of there being less charge in this region of the spectrum.

The degree of angular spread increases towards the lower energy regions. This is expected since the recoil force is directed against the propagation axis, and so electrons lose momentum predominantly in p_z. The transverse components, p_x and p_y, remain largely unaffected by this recoil, thus the propagation angle $\theta_{div} \simeq p_x/p_z$ increases. Based on the results in the previous section, it is unlikely that the spectral features in the low energy regions will be detectable, however.

We see also that the edge signal in the 500 to $600\,\mathrm{MeV}$ region is of comparable magnitude to that in the centre. Since our aim is to maximise signal in the centre, while minimising signal at the edge, this may prevent useful measurements in that spectral region.

With a pre-interaction drift (Figure 4.16), the edge signal drops to zero as before
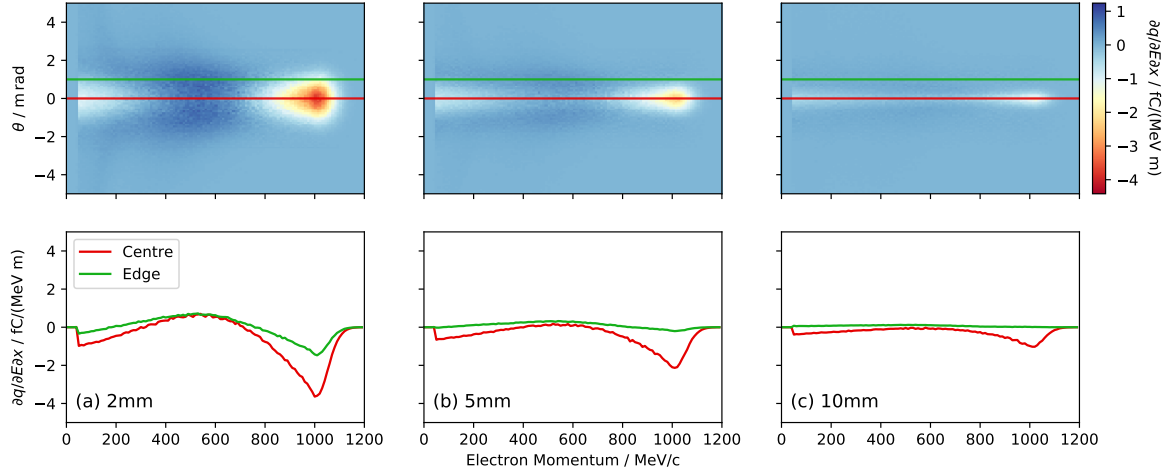
Figure 4.16: Test vs. control for (a) $d = 2\,\text{mm}$, (b) $d = 5\,\text{mm}$, (c) $d = 10\,\text{mm}$. $S(\text{edge}) \to 0$ as d increases.
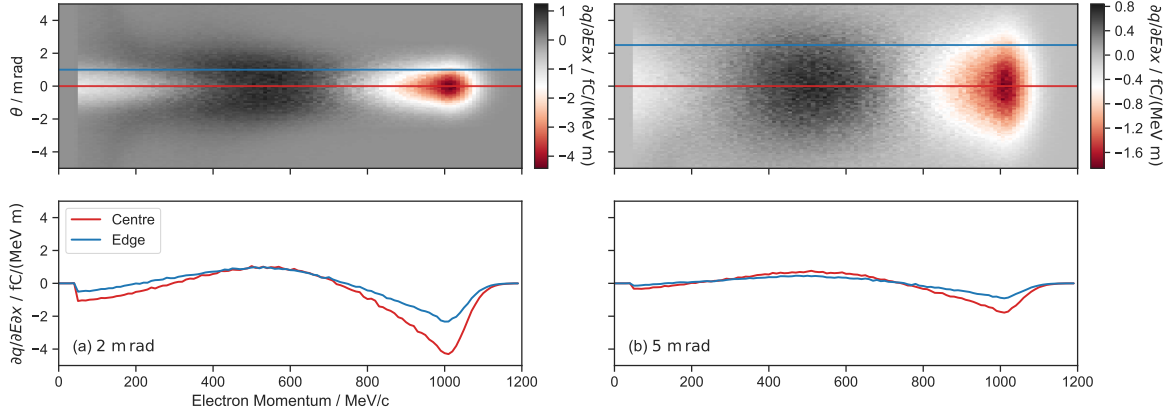
Figure 4.17: Comparison of (a) $2\,\text{mrad}$ and (b) $5\,\text{mrad}$ for the "Tail GeV" bunch. Sampling regions at $\theta = 1\,\text{mrad}$ and $\theta = 2.5\,\text{mrad}$ as before.

with the centre retaining a non-zero signature at both the $1\,\text{GeV}$ and the $100\,\text{MeV}$ scales. As expected, the middle of the spectrum displays a much lower signal. A comparison between the 2 and $5\,\text{mrad}$ cases yields a familiar result: The reduced charge density in the divergent beam suppresses the signal across the bunch (Figure 4.17). Plotting the edge signal at each drift distance in Figure 4.18, and overlaying the detector limit indicates the optimum drift lies between 2 and $5\,\text{mm}$ at $2\,\text{mrad}$, and is around zero for $5\,\text{mrad}$.

We use the peak values of the centre and edge signal to determine the optimum drift distance, shown in Figure 4.19 (left), which are found to be $4\,\text{mm}$ and $1\,\text{mm}$ for $2\,\text{mrad}$ and $5\,\text{mrad}$, respectively. The measureable fraction, f, is shown in Figure 4.19 (right) for the two values of θ_{div}. At around $30\,\%$ for the $2\,\text{mrad}$ beam, this is significantly

85
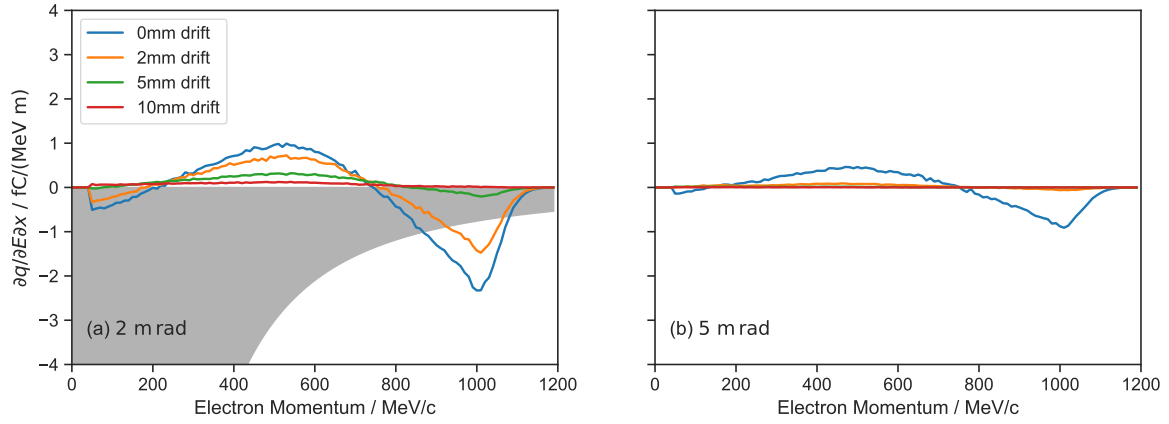
Figure 4.18: $S(\text{edge})$ for "Tail GeV". All but the high energy part of the spectrum is above the detection threshold for both 2 mrad and 5 mrad.
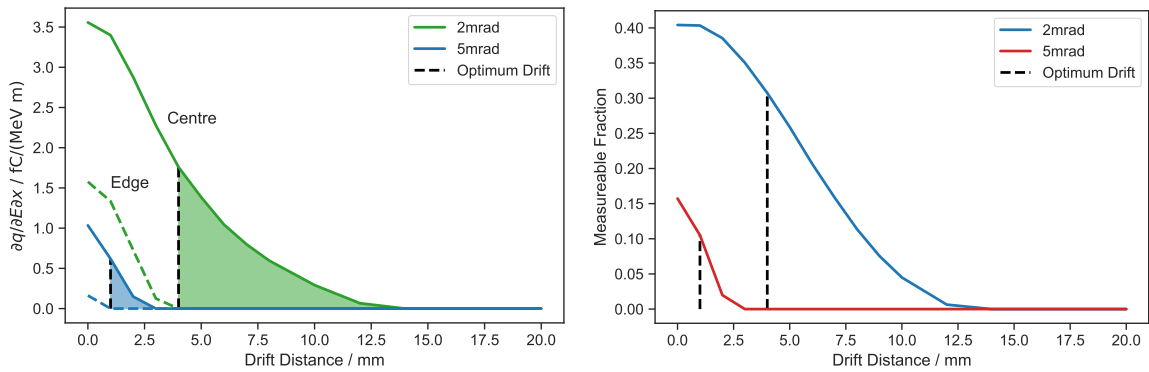
Figure 4.19: Optimum drift for "Tail GeV". Left: S_{adj} as a function of d. Optimum drift occurs at $d = 4\,\text{mm}$ (2 mrad); $d = 1\,\text{mm}$ (5 mrad). Right: Measurable fraction f for both divergence values. $f(d_{\text{opt}}) = 0.31$ (2 mrad); $f(d_{\text{opt}}) = 0.11$ (5 mrad).
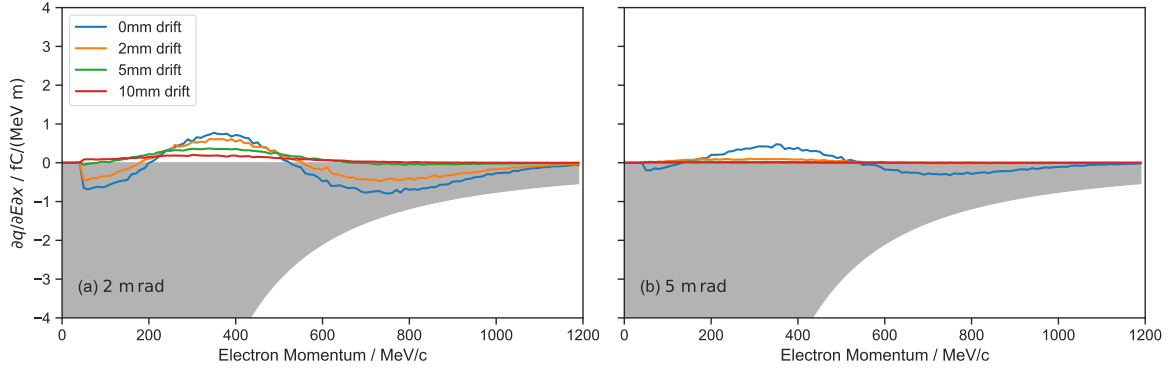
Figure 4.20: $S(\text{edge})$ for "Broad 500 MeV". The signal is entirely below the detection threshold, even for $d = 0$ mm.

poorer than the 68 % for the corresponding "Narrow GeV" case. Given that the total charge is the same in both cases, this result is not surprising.

We are beginning to see a pattern to the results here. Electron beams with higher charge density, either due to lower divergence, or narrower energy spread, appear to retain signatures of RR more readily.

Broadband 500 MeV

Next on the list of electron beams is the "Broad 500 MeV" case. The following results are abridged, on account of their similarity to the previous section. The key figures of merit are included for completeness. Shifting the spectral peak down from 1 GeV in the previous case to 500 MeV has the unsurprising result of further reducing the detectable signal. Figure 4.20 indicates that the optimum drift is 0 mm, which is simply a consequence of the signal being below the detection threshold at all values of d. The figures of merit are shown in Figure 4.21. Even with no drift, we find a measurable fraction of 2 % at 2 mrad, and ~ 0 % at 5 mrad.

Despite the unremarkable nature of this result, it is nevertheless a useful data point for experimental planning. We need to know what electron beam parameters are appropriate for our measurement, but it is also important to know what configurations are *not* useful, so that we do not waste time and effort.
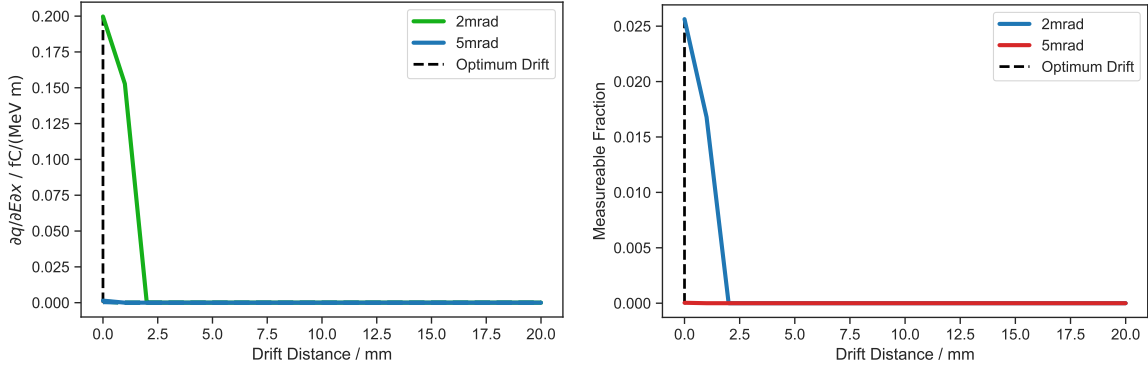
Figure 4.21: Calculated optimum values for "Broad 500 MeV". Although the optimum drift is found to be $d_{\mathrm{opt}} = 0\,\mathrm{mm}$, the measurable fraction, $f(d_{\mathrm{opt}})$, is $2.6\,\%$ for $2\,\mathrm{mrad}$ and $0\,\%$ for $5\,\mathrm{mrad}$. It is unlikely that this configuration would be useful for RR measurements.

4.3.6 Effect of Charge on Signal Level

We have seen several examples of how the charge density affects our ability to measure RR. The broadband electron beams from the last section are inferior to the narrowband case, as they contain insufficient charge. If we are not able to engineer narrowband beams experimentally, we may still be able to achieve our goal with high-charge, broadband bunches. Such characteristics are common when using ionisation injection, for example, and are typically less sensitive to fluctuations in laser conditions.

To see the effect of charge, the conditions of the "Tail GeV" bunch have been replicated below, with $75\,\mathrm{pC}$ total charge instead of $15\,\mathrm{pC}$. Comparing Figure 4.22 with its counterpart above (Fig. 4.16), the post-interaction spectrum is qualitatively similar with the amplitude of the signal approximately 3 times larger in the $75\,\mathrm{pC}$ case.

In Figure 4.23, the detection threshold has been included for our imaginary spectrometer described above (Sec. 4.3.2). We see that in comparison with the low-charge case (Fig. 4.18 (a)), the edge signal in the $\sim$500 MeV region of the spectrum is slightly above the detector limit for no initial drift, and is detectable at the GeV level until around $5\,\mathrm{mm}$ of drift.

With a higher charge in the bunch, we expect that a greater drift distance is required to reduce the edge signal below the detection threshold, and thus the optimum value is higher than in the $15\,\mathrm{pC}$ case. By directly comparing the two bunch charges in Figure 4.24 (left), we can see this is indeed the case with around $7\,\mathrm{mm}$ being the optimum as
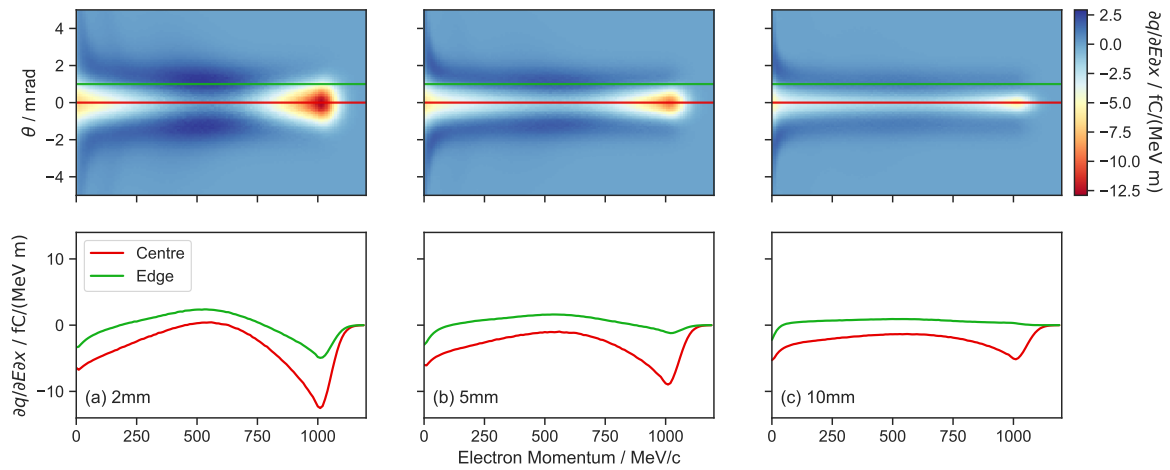
Figure 4.22: Test vs. control for the 75 pC "Tail GeV" bunch. Shape is qualitatively similar to the 15 pC case above, although with higher charge density overall. There is also a noticeable distinction between the centre and edge regions in the mid-energy range, which was not present in the lower charge case.
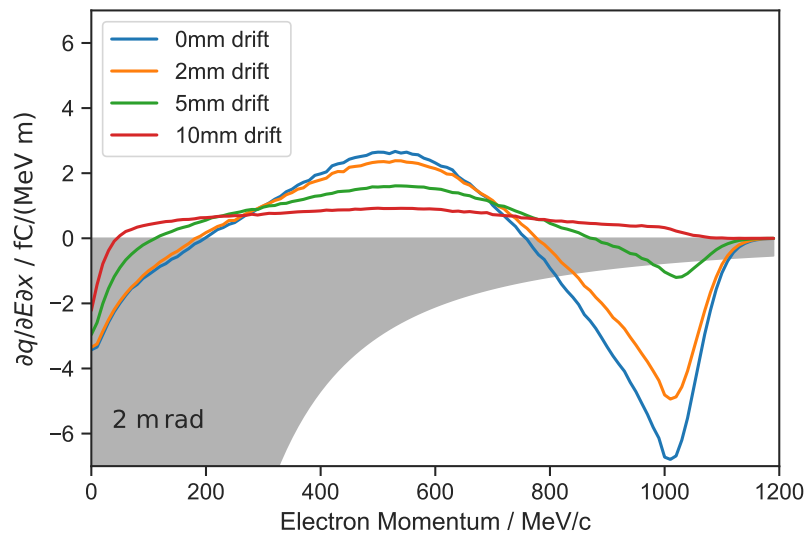
Figure 4.23: Edge profiles for $d = 0, 2, 5, 10$ mm. As in the 15 pC case, the detectable signal is primarily in the high energy, 800 MeV to 1000 MeV range, although in this case there is a marginal signal at around 500 MeV for 0 and 2 mm.
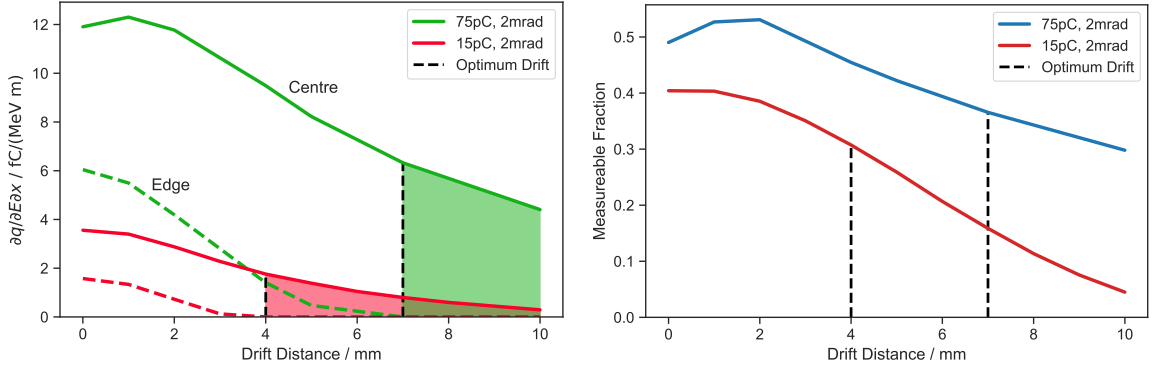
Figure 4.24: Left: Comparison of optimum drift for 15 pC (red) and 75 pC (green) "Tail GeV" bunches. The higher charge beam requires a larger drift of 7 mm to bring the edge signal to zero, compared to 4 mm for the lower charge. Right: Measurable fraction for both cases. The increase in charge by a factor of 5 yields an increase in $f(d_{\mathrm{opt}})$ from 30 % to 37 %.

opposed to 3 mm before.

Looking at our figure of merit, the measurable spectral fraction, in Figure 4.24 (right), we see that we have made a only a slight improvement in absolute terms with the increase in charge; from 30 % to 37 %. This is entirely due to the contribution from signal above 800 MeV, on account of the lower detection limit at higher energy.

4.3.7 High Energy Bunch

We saw earlier that keeping the overall spread of the bunch constant, but shifting the peak to lower energy ("Tail GeV" vs. "Broad 500MeV") made measurement more challenging since most of the signal was in the lower energy regions of the spectrum. We expect this effect to be analogous if we increase the charge, so it would likely not be useful to test the "Broad 500MeV" case here. Instead we note that the improvement between low and high charge bunches for the "Tail GeV" case was due to greater signal at the high energy regions.

The next test case therefore incorporates both an increase in total bunch charge and an increase in the average energy from 500 MeV to 1 GeV as shown in Figure 4.4 (h). We find an optimum drift distance (Fig. 4.25 (a)) of 7 mm with this bunch and a marked improvement in the measurable spectral fraction over the previous case; 70 % as opposed to 37 %. Again we attribute this improvement to the signal in the high-energy region of the spectrum, which now extends to 1.75 GeV.
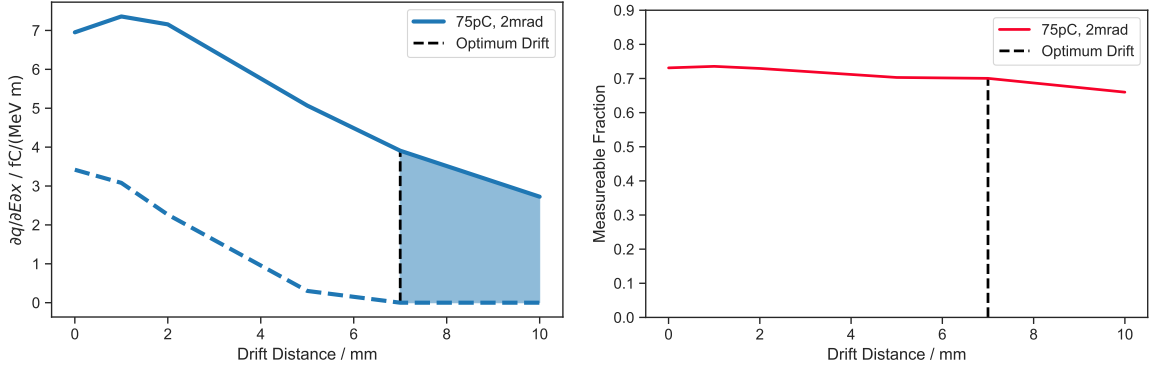
Figure 4.25: Optimum drift for the "Broad GeV" (75 pC) bunch is found to be 7 mm, with a measurable fraction $f = 0.7$. Notably the rate of change, $\partial f/\partial d$, is much lower than in previous configurations, on account of the large amount of charge at high energy.

4.4   Summary of Results

In the previous section we saw the results of eight electron beam configurations which varied in spectral composition, divergence angle, and total charge. By altering the pre-interaction drift distance, the divergence angle of the electrons within the interaction zone can be controlled, enabling preservation of RR signatures over a long distance (i.e. to a spectrometer screen). The optimum drift distance is defined as the point where the signal at the edge of the bunch is indistinguishable from the original spectrum due to the finite detection limit. At this distance, we use the fraction of the spectrum at the centre which retains measurable signal as the key figure of merit. The measurable fraction for each of the bunch types investigated is shown in Figure 4.26. We observe that the "Narrow GeV" and "Broad GeV" configurations offer the highest merit: 68 % and 70 %, respectively. For the two 75 pC cases, $f = 0.7$ for the broadband beam is better by almost a factor of two than the "Tail GeV" beam ($f = 0.37$). This is due to the geometry of our simulated electron spectrometer, which is far more sensitive to higher energy electrons.

We see by contrast that the "Broad 500MeV" configuration offers the lowest detectability, due to both the low charge contained in the bunch and the large fraction of charge below 500 MeV.

With the goal of measuring radiation reaction effects in mind, the results above highlight some key principles to maximise the likelihood of achieving this experimentally: First, we should aim to generate electron beams with as much charge as possible
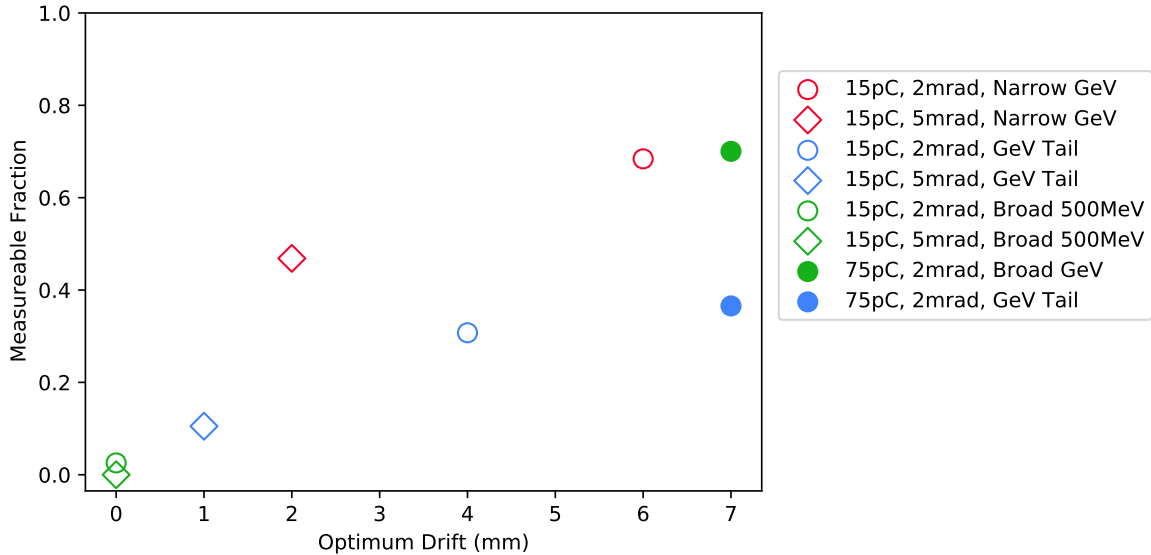
Figure 4.26: Summary of results. Bunch characteristics are linked by marker styles. For example, "Narrow GeV" results use red markers; divergence is marked by the shape, circles for 2 mrad and diamonds for 5 mrad; charge is indicated by the fill. The "Narrow GeV" at 2 mrad and "Broad GeV 75 pC (also 2 mrad) bunches have the highest measurable fraction of all those tested. An increase in divergence reliably hinders measurement, as does a large fraction of low energy electrons.

at high energy, as this will allow us to overcome the detector limit. Since the divergence is clearly an important factor, we should also seek to control the injection process in order to achieve ideal conditions. In particular, shock injection methods have been shown to produce narrow energy spread with low divergence [24, 137], while ionisation injection boosts the total charge [75]. It has been shown that it is possible to combine the benefits of both of these techniques [138, 139].

Secondly, spectrometer geometry matters. Naturally the detector limit is a function of the dispersion of the electrons on the scintillating screen. Adjusting the position and angle of the screen changes how the electrons are distributed, and allows for optimisation of signal in a particular energy range. The simulated spectrometer we have used above is unfavourable for detecting signal at low energy. Despite this, we have shown that RR signatures are detectable using typical electron configurations. Optimisation of the spectrometer geometry should therefore only improve the signal measured experimentally.
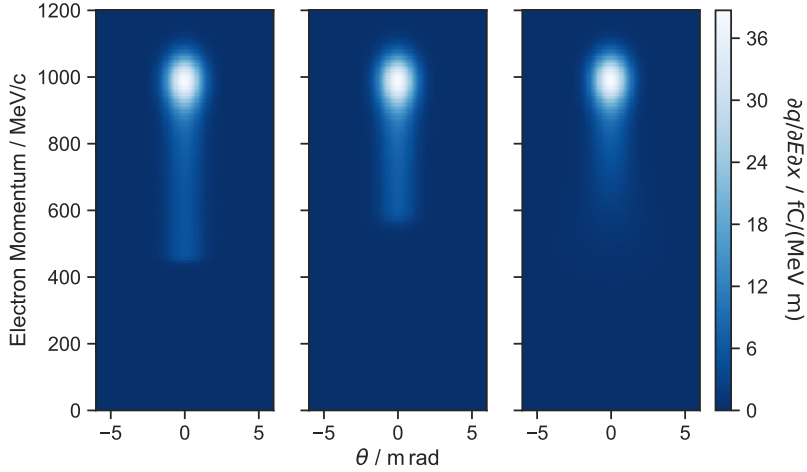
Figure 4.27: Result of laser collision with quasi-monoenergetic $1\,\text{GeV}$ electron beam in (a) Classical (LL), (b) Semi-Classical, (c) QED frameworks. The hard edge present in the (semi-)classical case is a key experimental indicator.

4.5 Discussion

4.5.1 Comparison of Classical and Quantum Effects

Among the reasons to study radiation reaction, the fact that it remains one of the few untested areas of quantum electrodynamics is a particularly strong one. The quantum non-linearity parameter, η determines the degree to which stochastic effects dominate a laser-electron interaction. Interestingly, in the range accessible to current laser systems, i.e. $\eta \lesssim 0.1$ is where QED, classical (Landau-Lifshitz), and semi-classical models all claim validity, and yet disagree substantially. This disagreement is seen most clearly in the 1D example shown in Figure 2.9. Both the classical (LL) and semi-classical (SC) predictions are characterised by a reduction in energy spread as well as an overall reduction in energy. The SC case predicts the same final mean energy as the QED model, but fails to match the spread. The SC emission model simply incorporates a correction factor $g(\eta)$ to the classical power emitted (see Sec. 2.6.2) which explains this limitation.

Using the "Narrow GeV" electron bunch from the previous section, we can see the different model predictions in 3D in Figure 4.27. The differences are not as clear-cut as in the 1D case due to the spatial variation of laser intensity, (and therefore η). Nevertheless there are some crucial differences which, in principle, would be identifiable experimentally. The presence of a hard edge at the minimum energy in the LL

93
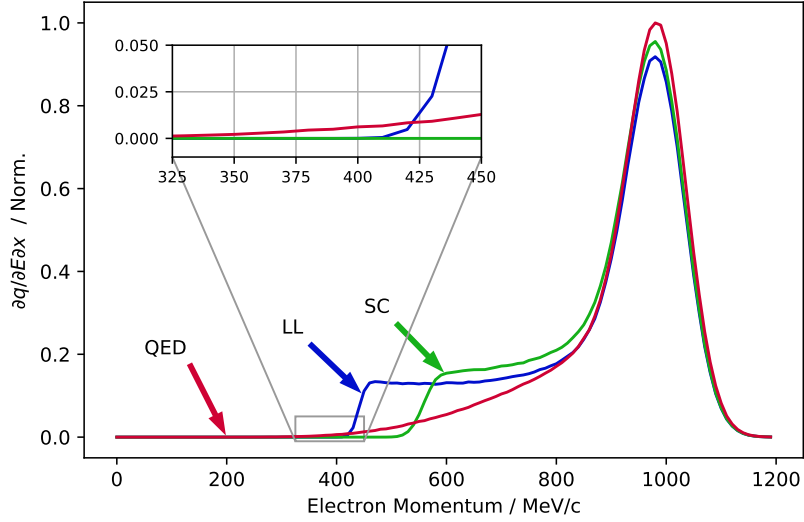
Figure 4.28: Central lineouts of post-interaction Narrow GeV bunch for three emission models. The classical and semi-classical results show a steep edge, whereas the QED model predicts a gradual slope. The inset shows how the lowest energy for the QED emission model is lower than both the classical and semi-classical.

(420 MeV) and SC (550 MeV) cases clearly distinguishes them from the QED result, which shows a spread in angle as electrons lose energy.

The central regions of each case are shown in Figure 4.28. In the QED case, the presence of electrons below the lowest energy in the classical case is a consequence of the 'straggling' effect, where electrons can reach the highest intensity region of the laser pulse before emission, thus increasing the maximum η of the interaction. Assuming the laser intensity can be well characterised, the presence of electrons below the classical limit would definitively demonstrate quantum effects in an experiment [140].

Applying the same detector threshold to each of these cases (Fig. 4.29), again highlights the importance of our electron beam characteristics. For comparison of classical models with QED, the lowest energy regions are critical, and this is exactly the region that is most difficult to measure. As we discussed above, however, this is not insurmountable. As a final consideration, we note that the precise experimental parameters can also influence whether the laser-electron interaction exhibits classical or quantum behaviour. Although outwith the scope of this work, we refer the reader to publications by Ridgers *et al.* [141] and Arran *et al.* [142] for a detailed discussion.
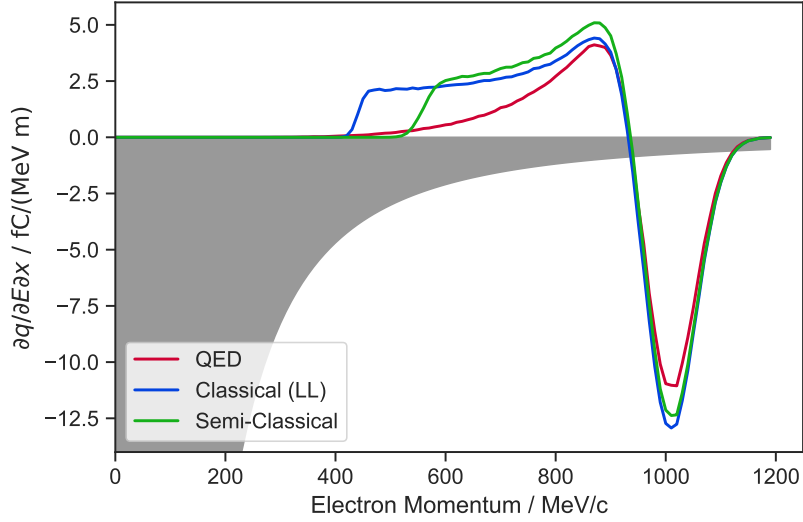
Figure 4.29: Difference plots for the three emission models. For the electron beam configuration used, the prominent features of RR are below the detection threshold, highlighting a potential difficulty of obtaining this measurement experimentally.

4.5.2 Accuracy of Simulations

With any computational work, it is crucial to verify that the results are physically sensible. EPOCH has been fully benchmarked against other codes [120]; however the old adage, 'Garbage In, Garbage Out', still applies. The input parameters, specifically those of the laser pulse and the electron bunch are the first points of consideration.

It can be seen from Fig. 4.3 (b) that the intensity of the pulse does not reach zero. Since the electric field oscillates between positive and negative values, it must cross the time axis during each cycle, meaning the intensity should also be zero at those points. This is an aliasing effect caused by insufficient resolution of the electric field in the simulation domain.

For a grid resolution of 10 cells per micrometer, a single laser pulse cycle is only 8 cells in length, which introduces sharp field gradients and can affect the motion of the electrons in unphysical ways. This effect is mitigated, however, by spline interpolation of the fields in the particle grid.

The results from EPOCH were compared to that of the code developed by T. G. Blackburn, which employs an exact, analytical solution of Maxwell's equations for the incident laser field. A comparison of the RR effect on the electron beam in the two codes is shown in Fig. 4.30. Despite the poor resolution in the EPOCH field grid, the effect on the particles is sufficiently close to that of a continuous field that this can be
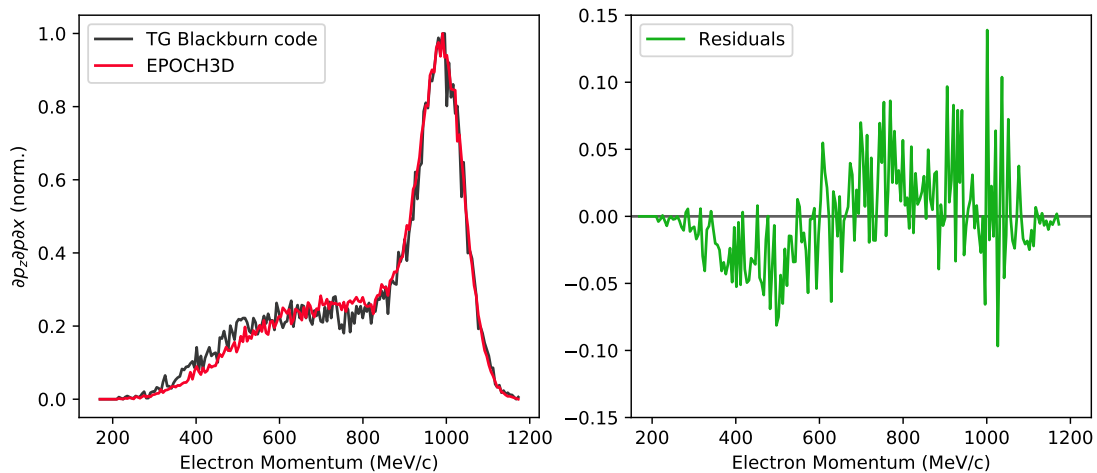
Figure 4.30: Comparison of electron energy loss between EPOCH3D and analytical field solutions. Both codes use the same Monte-Carlo algorithm for emission.

neglected as a source of error.

4.5.3 Energy-Dependent Electron Divergence

It has been assumed thusfar that the transverse momentum, $p_{x,y}$ of electrons is independent of the forward momentum, p_z. The divergence angle of the electrons is calculated from the ratio of these quantities (i.e. p_x/p_z), and as such the divergence angle of a particular electron has an implicit dependence on the forward momentum. Consequently the spectral characteristics at the edges of the electron bunch are not identical to those at the centre. To illustrate this, consider two electrons with forward momentum p_z, and $p_z + \delta$, respectively. If they happen to have the same transverse momentum, the first electron will propagate at a wider angle than the second.

Theoretical calculations [143, 144] indicate a weak coupling between the forward and transverse components of electron momentum in LWFA. The transverse (x) momentum gained by an electron in a wakefield scales as

$$\frac{p_{xf}}{p_{xi}} \propto \left(\frac{p_{zf}}{p_{zi}}\right)^{1/4},\tag{4.3}$$

where the subscripts i and f indicate the initial (i.e. at injection) and final values of the momentum.

Taking this into account in a test simulation, we see a variation in the electron spectrum when measured at different transverse positions. Figure 4.31 (a, b) demon-
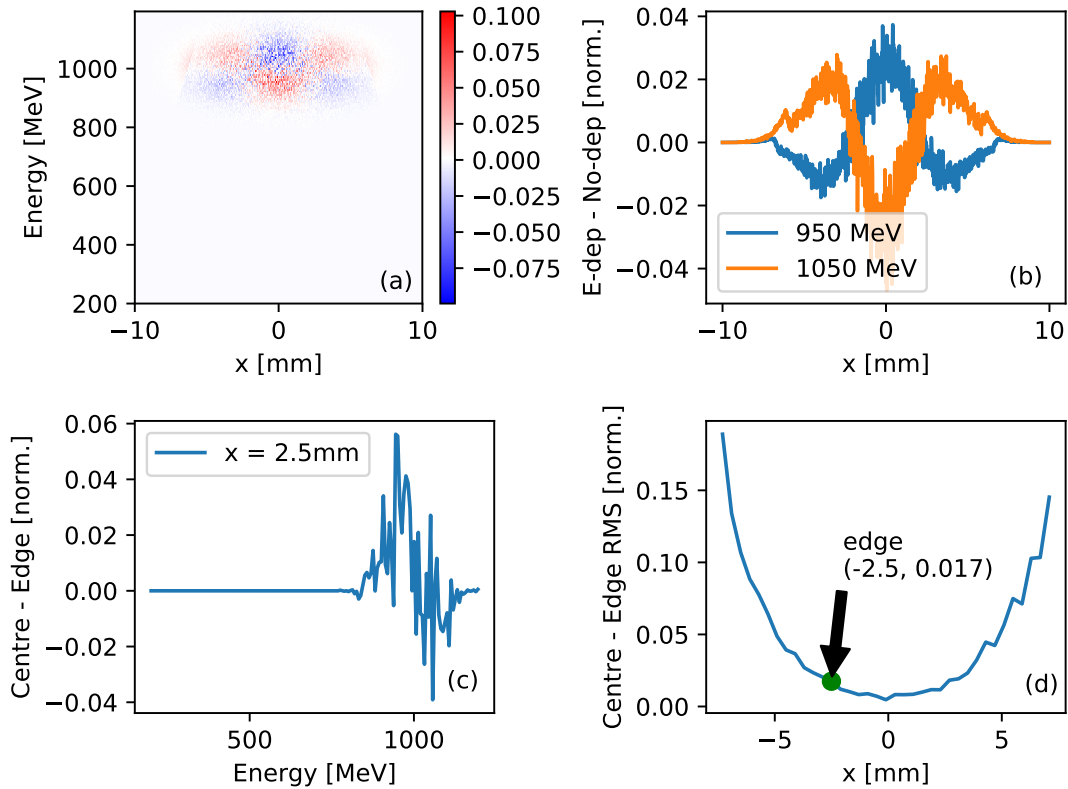
Figure 4.31: Effect of momentum coupling on the transverse structure electron bunch. (a) Difference between electron bunches with / without coupling; (b) Lineouts of (a) at $\pm 1\sigma$ from the mean energy; (c) Deviation from central ($x = 0$) spectrum at a distance $x = 2.5\,\mathrm{mm}$, normalised to the centre; (d) RMS Deviation from centre as a function of x.

strates the effect of the momentum coupling on x-pz phase space. Where coupling occurs, there are relatively fewer electrons below the mean energy at the edges of the bunch. The result of this is that the spectrum measured at the edge will not be the same as the spectrum measured at the centre. Figure 4.31 (d) shows the variation with sampling position, and indicates that at $2.5\,\mathrm{mm}$ the spectral peak is $1.7\,\%$ lower than at the centre. This is therefore a small effect which could easily be compensated during analysis.

4.5.4 Space Charge Effects

A key assumption made in the results presented here is that space charge effects in the electron beam are negligible. Using the ASTRA code, we can simulate bunch propagation and test this. Each ASTRA simulation was initialised with 1×10^5 macro-particles representing a total charge of $75\,\mathrm{pC}$. A quasi-monoenergetic energy spectrum identical

97
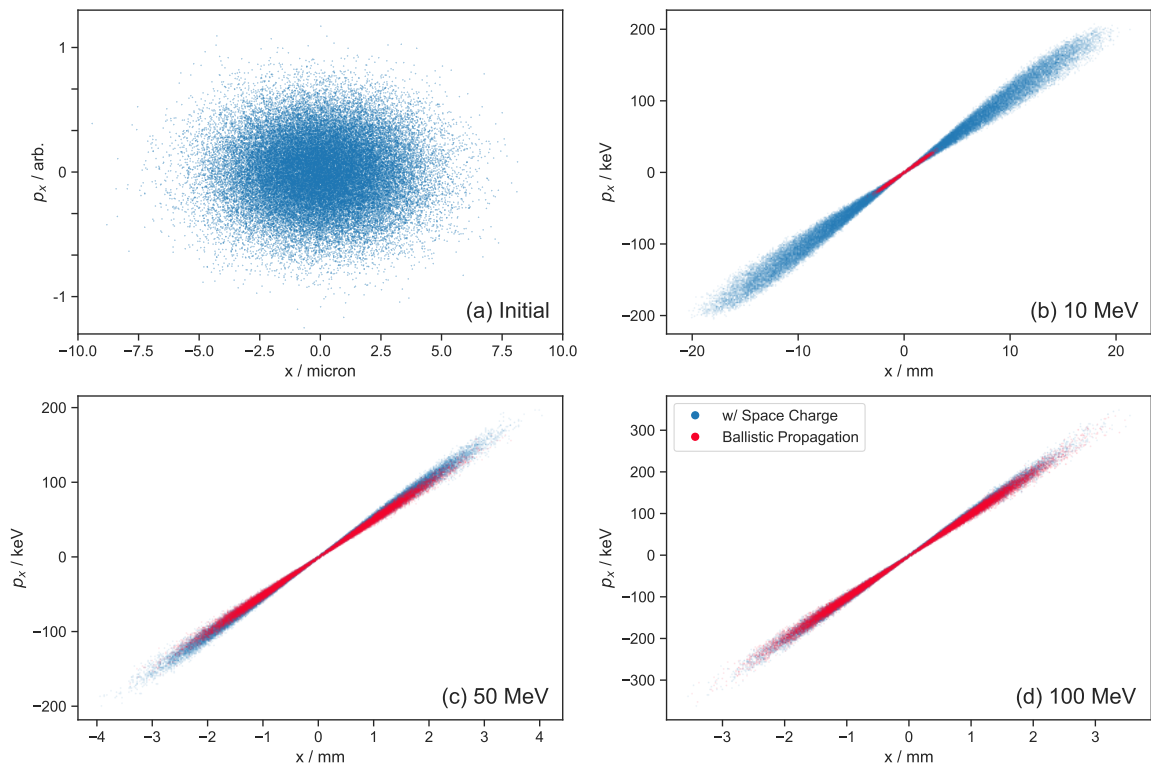
Figure 4.32: Effect of space charge effects on x-p_x phase space over a 1 m propagation. (a) Initial distribution, p_x values are scaled with p_z to maintain bunch properties. (b) Phase space for 10 MeV bunch propagated with space charge (blue) and without (red). (c) 50 MeV, (d) 100 MeV.

to the 'Narrow GeV' was used initially. The forward momentum was then varied to observe how space charge effects depend on energy. For each case, the transverse momentum, and energy spread were scaled according to the forward momentum, in order to preserve $\Delta E/E$ and the divergence angle.

Figure 4.32 shows the results for some low energy electron beams. We see that space charge effects are significant in the 10 MeV case, with the electrons spreading by almost a factor of 10 in both x and p_x. The effect is greatly reduced at 50 MeV, and almost indistinguishable at 100 MeV however.
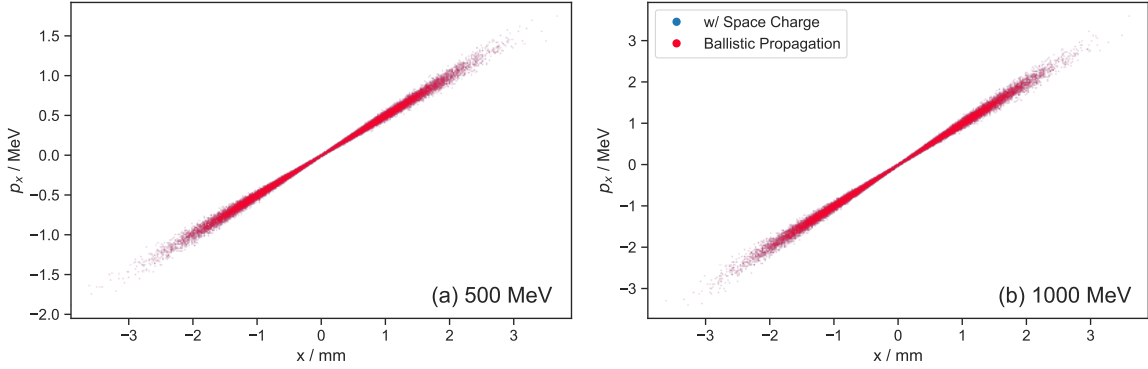
Figure 4.33: Phase space for (a) 500 MeV and (b) 1 GeV bunch with space charge (blue) and without space charge (red). The final distributions are indistinguishable, hence the blue points are obscured.

At 500 MeV and above (Figure 4.33), the phase space distribution is unchanged by the inclusion of space charge. Based on this, we can confidently say that our initial assumption is valid, with the caveat that propagation of electrons of around 100 MeV and below would require the consideration of space charge effects.

4.5.5 Additional Diagnostics

Although we have focussed on electron spectrometry as the tool of choice to measure RR effects, it is not sufficient in isolation. The X-rays generated by the laser-electron collision are crucial to corroborate our electron beam measurements, as they indicate when a 'hit' has occurred.

To successfully collide a laser with an electron bunch as we have simulated requires that a 2 μm, 40 fs laser pulse and a ~ 10 μm electron bunch occupy the same space at the same time. This is experimentally achievable, as demonstrated by Cole *et al.* [42] and Poder *et al.* [43], however it is not without its challenges. Both the laser pulse and
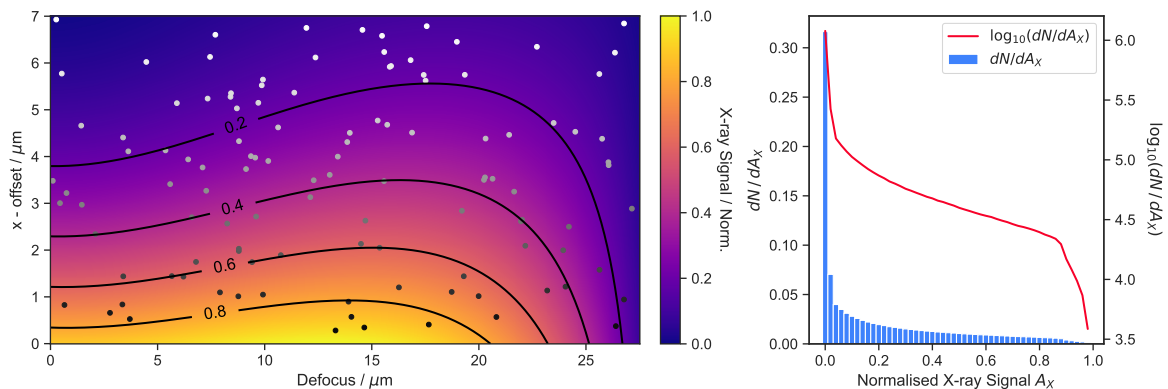
Figure 4.34: Heatmap showing the signal obtained where the electron bunch and the laser pulse are temporally and spatially offset. The scatter points indicate random samples from a 2D normal distribution, intended to replicate a series of shots where 'jitter' is incorporated.

electron bunch are susceptible to spatial and temporal 'jitter', not least due to thermal fluctuations and vibrations in the environment.

These random fluctuations are the primary reason for the small number of shots in the dataset published by Cole *et al.* Despite several hundred shots, only four were considered 'good hits' on account of the strong X-ray signal detected. Using the measured fluctuations for both the laser and electron bunch, we can estimate the probability of a successful collision, and the magnitude of the X-ray signal we expect.

Figure 4.34 shows the effects of random fluctuations in timing and pointing on the measured X-ray signal. A total of 500 shots are superimposed on a heatmap of the expected X-ray signal. Defining the region where the X-ray signal is above 80 % of the maximum as a 'good hit', we see that only around 1 % of shots occur here.

Some techniques for detecting the X-rays and measuring the spectral content, which can also yield information about radiation reaction effects, will be discussed in Chapter 6.

4.6 Conclusion

The results presented in this chapter aim to address the problem of direct experimental measurement of radiation reaction in laser-plasma interactions. Laser systems available at the time of writing are capable of reaching the RR regime, but only just. Precise measurements are therefore essential.

The scheme described here serves to mitigate the uncertainties from shot-to-shot variation by enabling a single-shot measurement technique which captures the electron spectra before and after the interaction with a high-intensity laser pulse. A millimeter-scale drift before collision facilitates a correlation between transverse momentum and position in an electron bunch, which preserves the original spectrum in regions unaffected by the laser.

A crucial consideration, however, is that of detection efficiency. For a given electron beam configuration, i.e. spectral shape, divergence, peak energy, and charge, an optimum drift distance exists, beyond which the spectral shift becomes too diffuse to be detected by conventional means. Even with an optimum drift, it may be necessary to employ high sensitivity detectors with close to single particle efficiency. The exact value of the optimum drift also depends on the geometry of the electron spectrometer, as this also influences the detection limit significantly.

As we have seen, the electron beam configuration is important, and so an experimental realisation of this technique may require careful design. Employing alternative mechanisms such as shock injection may be necessary to achieve reliable results, however this is well within the capabilities of modern facilities.

Despite some potential challenges in detection, the results in this chapter show that measurement of radiation reaction is achievable with currently available means, and provide key insights into the design of future experiments.

Chapter 5

Bremsstrahlung Imaging of Industrial Materials

5.1 Motivation

The first laser, invented in 1960, was little more than a scientific curiosity. Famously called "A solution seeking a problem", applications of the new technology took several years to realise. Now, lasers are ubiquitous in modern society and so thoroughly integrated into our way of life as to be indispensible.

High-power, petawatt-class lasers are at the forefront of modern technology and, much like their ancestors, presently have few applications outside the scientific domain. In recent years however, there has been a strong push from within the laser-plasma community towards collaboration with private industry with a view to reducing the typical 'lag time' between scientific discovery and societal applications. One such application, and the focus of this work, is that of hard X-ray sources.

In industrial manufacturing, the ability to characterise the internal structure of materials and components is crucial for quality control. For this purpose, a linac-driven X-ray source is often the tool of choice, and for good reason: The sources themselves are easily tuned, and can operate at repetition rates of several MHz, enabling rapid raster scanning, or efficient tomographic reconstruction. However, the energy of the X-ray source is limited by the length of the accelerator, with longer accelerators being required for imaging denser materials. In addition, the source size of a linac-generated X-ray beam on the order of millimetres [145], which confines the imaging resolution.

These two limitations can be overcome by employing a laser-driven source.

X-ray sources driven by laser-wakefield accelerators are capable of producing high-energy photons, and small source sizes, within a compact facility. In addition, the characteristics of LWFA electrons, and thus the X-rays, can be controlled by only a few key parameters.

In the following, we present results of a 3-week development project at the Central Laser Facility, where the suitability of an LWFA-driven bremsstrahlung source for imaging of industrially-relevant materials was explored.

Why Bremsstrahlung?

Not all X-ray photons are created equal. A source driven by LWFA can be generated by three[1] different mechanisms which strongly influence the characteristics of the X-rays.

Betatron oscillations inside the wakefield, for example, produce highly coherent, broadband sources in the 10s to 100s of keV range [45, 146, 147]. Betatron X-rays have small source sizes of a few microns, making them excellent for high resolution imaging [148]. The coherence also allows for phase-enhanced (phase-contrast) imaging [46, 49].

An inverse Compton source can be generated by scattering laser light from an accelerated electron bunch, either by direct illumination with a secondary beam [56, 149], or by reflecting the driver beam back into the electron beam [55]. In a counterpropagating geometry with $a_0 \ll 1$, the scattered photons are shifted in energy by a factor of $4\gamma_e^2$, where γ_e is the electron Lorentz factor. The resulting photon characteristics are thus determined by the electrons. A narrowband electron spectrum will result in a similarly narrow photon spectrum. As a_0 approaches 1, harmonics of the fundamental frequency will appear in the photon spectrum [150, 151] due to multi-photon scattering. For higher intensities, the spectrum becomes broadband.

Bremsstrahlung driven by LWFA is generated by colliding the electron beam with a converter material, e.g. aluminium. The resulting photon spectrum is broadband, with a cutoff energy corresponding to the maximum electron energy. Increasing the

---

[1]Here we mean betatron, bremsstrahlung, and inverse Compton scattering (ICS). Thomson scattering is often considered a separate mechanism, but is simply the low energy limit of ICS. Similarly, wigglers and undulators used in XFELs perform the same function as wakefield buckets, albeit on a larger scale. We thus include XFELs in the same category as LWFA betatron.

thickness or density of the converter yields higher photon numbers (for thicknesses much less than the radiation length of the material), but at the price of increased source size due to additional scattering of electrons.

For imaging purposes, as the size and density of the object increases, we require more and more energetic X-rays to penetrate the sample and reach our detector. Both ICS and bremsstrahlung can in principle drive such sources, but ICS sources produce much lower photon energy for the same electron beam.

As an illustrative example, consider a monoenergetic electron beam of energy 500 MeV. A linear ICS source would produce a beam of 4 MeV, whereas bremsstrahlung produces photons of up to 500 MeV. To generate a similar ICS source would require an electron beam of 5 GeV. While this is possible [26], it is logistically far more challenging than a 500 MeV electron beam. In addition, an ICS source using a secondary beam requires precise spatial and temporal alignment of the electrons and scattering pulse. A bremsstrahlung converter is a barn door in comparison[1].

Bremsstrahlung sources trade precise control over spectral characteristics for ease of implementation. Lower electron energies are required, and the spectral shape of the electrons has little effect on the X-rays. By using bremsstrahlung, we lower the barrier to entry for industrial imaging applications since smaller, less expensive laser systems can be used.

5.2   Experimental Layout

The South beam of the Gemini laser was focussed, using an $f/40$ parabolic mirror, into a gas cell with 11 mm between entrance and exit cones[2]. After leaving the gas cell, the remaining laser energy was dumped by a section of polyimide tape which acted as a plasma mirror. LWFA electrons produced were then either diagnosed by a magnetic spectrometer, or used to drive bremsstrahlung by placing a converter target in the path of the emitted beam. Laser parameters were kept constant throughout the experiment. Nominal laser conditions are given in Table 5.1. An array of caesium iodide crystals (Fig. 5.2) was placed outside the target chamber to collect the emitted X-ray beam for

---

[1]A literal barn door would be an effective source of bremsstrahlung, too.
[2]The gas cell has a variable length, but was set to 11 mm for all shots relating to the results presented here.
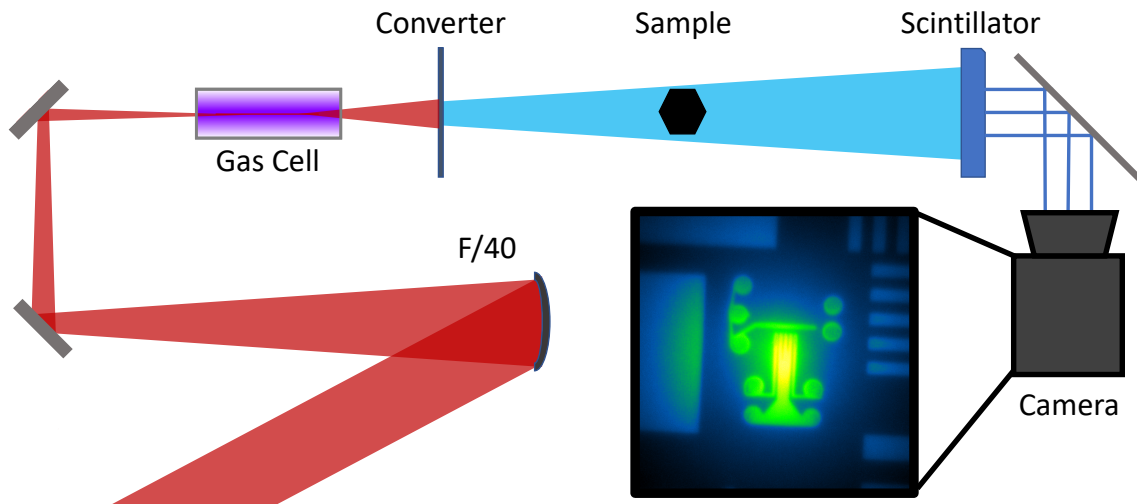
Figure 5.1: Schematic of the experiment carried out using the Gemini laser at the CLF. Figure adapted from [61].

Pulse Energy (Uncompressed)	10 J
Pulse Energy (On Target)	6 J
Pulse Width	49 fs
Focal Spot Diameter	50 μm × 40 μm
Strength Parameter (a_0)	1.3

Table 5.1: Experimental laser parameters for Gemini.

characterisation of the spectrum. Information from the array was collected using an Andor NEO 5.5 sCMOS camera with a Navitar adjustable focus TV lens. The X-ray signal was varied by adjusting the electron density in the gas cell (by changing the backing pressure), and by selecting from a range of converter targets.

After comparing the signal produced for a range of converters and densities, a subset of converters was chosen to generate a source appropriate for imaging. The caesium iodide stack was then replaced with a LYSO crystal, which captured the incident X-ray beam on-axis, and relayed the image via a mirror to a camera (Andor NEO 5.5 sCMOS). Each of the samples was placed at one of 3 locations along the path of the X-ray beam, designated M1, M2, and M3 (Fig. 5.3). Since there is a trade-off between magnification and the field of view in choosing an imaging position, small, highly-detailed objects were placed at M1[1], and larger objects with coarser features were placed at M2 and M3.

---

[1]Samples placed at position M1, which was closest to the source and offered the highest magnification, were imaged exclusively with betatron X-rays. This data is covered in a separate publication [47] and will not be discussed here.
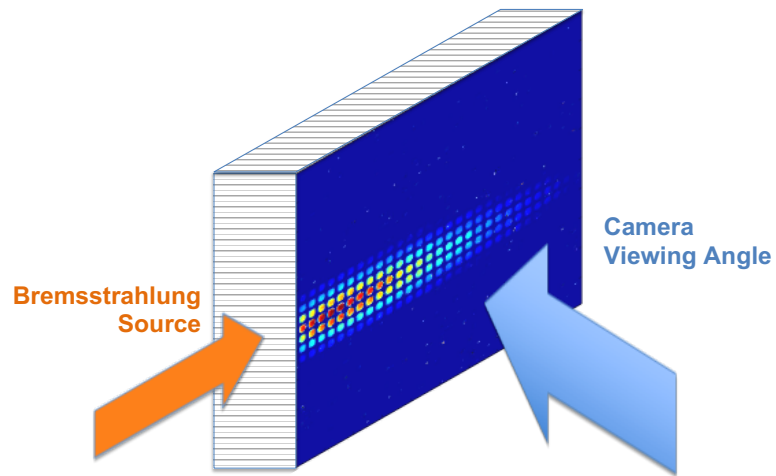
Figure 5.2: Caesium Iodide scintillator array. Crystals are arranged in a grid formation and placed on the X-ray beam axis. Light output from the crystals is measured and used to infer the spectral characteristics of the X-rays. Figure adapted from [61].

Figure 5.3: Schematic of three imaging positions. The distance from the source S of each position is indicated in mm. The magnifications for each position are: $M1 = 17$, $M2 = 2.5$, $M3 = 1.6$.
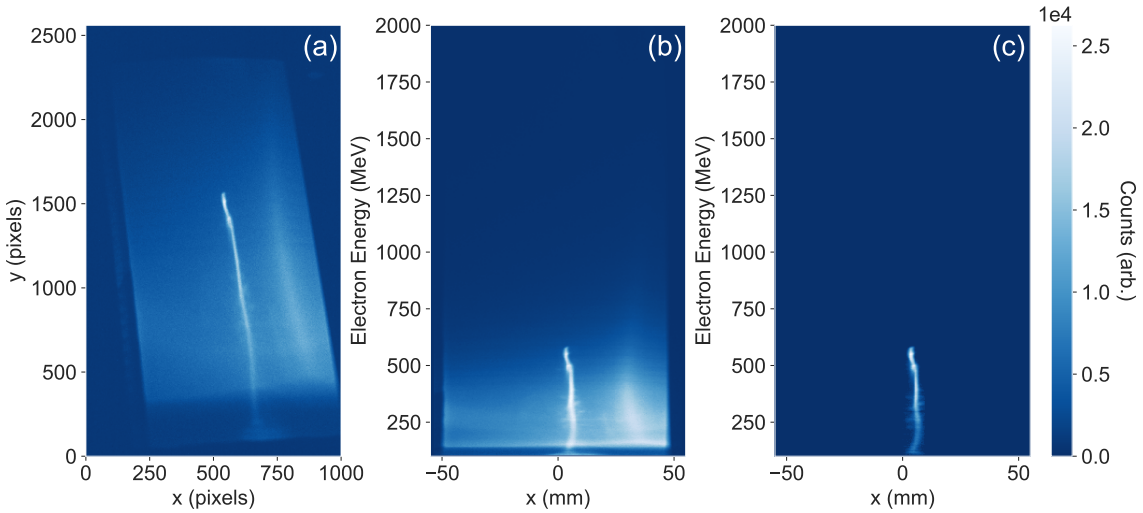
Figure 5.4: Projective transform and background subtraction. (a) Raw image of electron beam. (b) transformed and calibrated image showing spatial extent and energy. (c) Background light removed.

5.3 Experimental Results

Results obtained from the experiment described above are laid out in the following section. The process of analysis of the data will also be discussed, albeit briefly. Where appropriate, the reader will be referred to Chapter 3 for further details of the analysis employed here.

This section is structured as follows: First, a characterisation of the wakefield-accelerated electron beams, followed by an analysis of bremsstrahlung X-ray properties as measured by the CsI stack, and then by the LYSO crystal, including a comparative discussion of the two scintillator types. We then compare the measured X-ray source properties to predictions made by Monte-Carlo simulations based on the electron beams. Finally, the validity and implications of the results for future research and applications will be discussed.

5.3.1 Electron Spectra

To fully characterise the X-ray source, it is important to understand the properties of the electron beam. In general, it is not possible to measure the electron spectrum and the X-ray beam simultaneously, as the interaction with the converter target scatters the electrons (although a thin target may allow some post-converter analysis). We are nonetheless interested in the driving electron beam, in particular because it is more
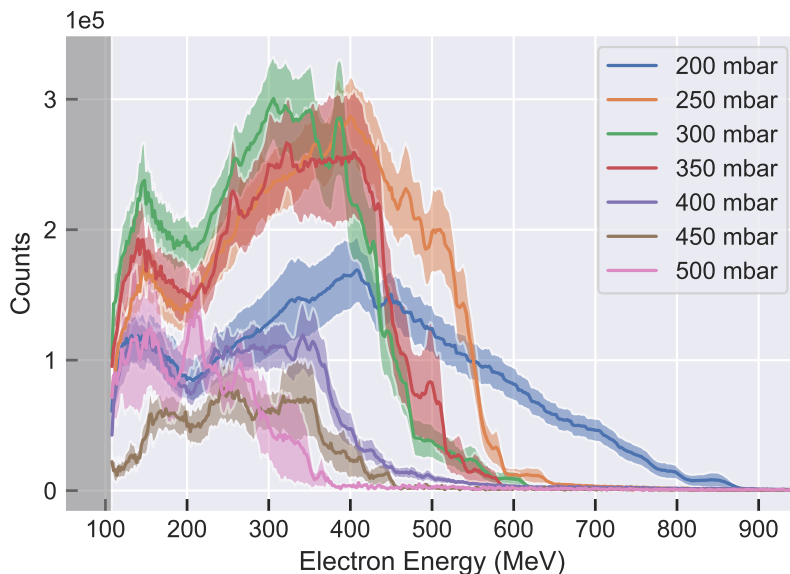
Figure 5.5: Average electron spectrum for each pressure setting. Shaded regions indicate the standard error in the mean. Electrons below 104 MeV were not measured.

straightforward to measure the electron spectrum and infer the X-ray spectrum via computational methods, than it is to measure the X-ray spectrum directly. Therefore we first measure the electron beam in isolation to determine the response to input parameters. By characterising the electrons in this way, we can make a reasonable assumption about the electron spectrum when a converter is in place.

The electron spectrum was measured by first dispersing the beam through a magnetic field, and then imaging the response of a Lanex screen (Sec. 3.2.1) using an Andor Neo sCMOS camera. To extract the spectrum, a projective transform is used to correct for the angle of the camera, and a spatial calibration is applied to map the pixel coordinates to the appropriate energy and spatial coordinates. An image of a typical dispersed electron beam and its corresponding calibrated transform is shown in Fig. 5.4. Analysis of the electron data was complicated by the presence of scattered laser light on the lanex due to insufficient filtering in the imaging system (Fig. 5.4). The level and structure of the background varied from shot-to-shot, and also with the electron density in the gas cell, and so could not be perfectly subtracted from the signal. The pressure of the gas cell was varied between 200 and 500 mbar, in increments of 50 mbar. The electron density for each setting was measured using a transverse optical probe and a Mach-Zender interferometer. Figure 5.8 (inset) shows the variation in the retrieved density, which varies linearly with P_{cell}. Over the course of several days, the
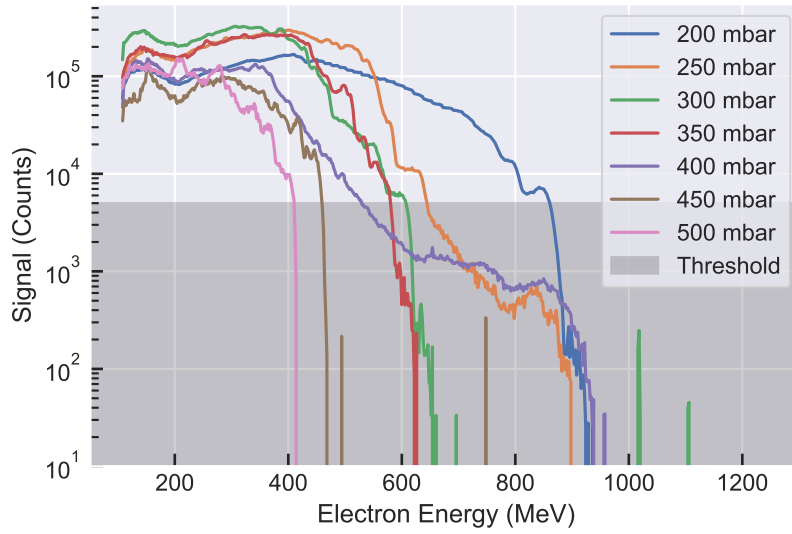
Figure 5.6: Average signal on electron spectrometer as a function of energy. The shaded region represents the noise threshold.
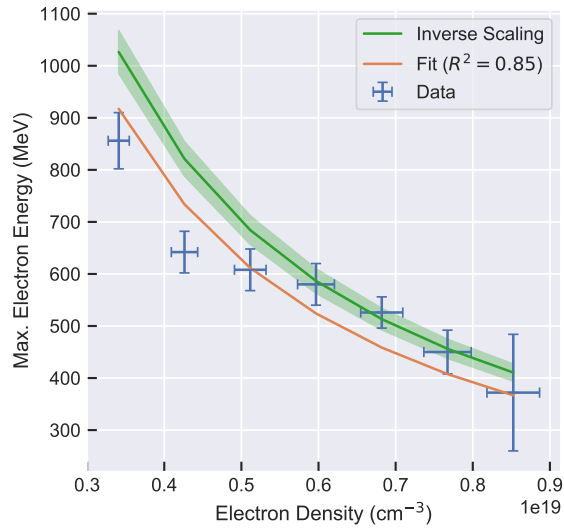
Figure 5.7: Maximum electron energy as a function of electron density ($n_e \propto$ backing pressure). Green line is the predicted maximum energy in the linear wakefield regime.

Pressure	Shots
200 mbar	28
250 mbar	42
300 mbar	23
350 mbar	11
400 mbar	32
450 mbar	7
500 mbar	5

Table 5.2: Electron characterisation shots for each pressure setting.
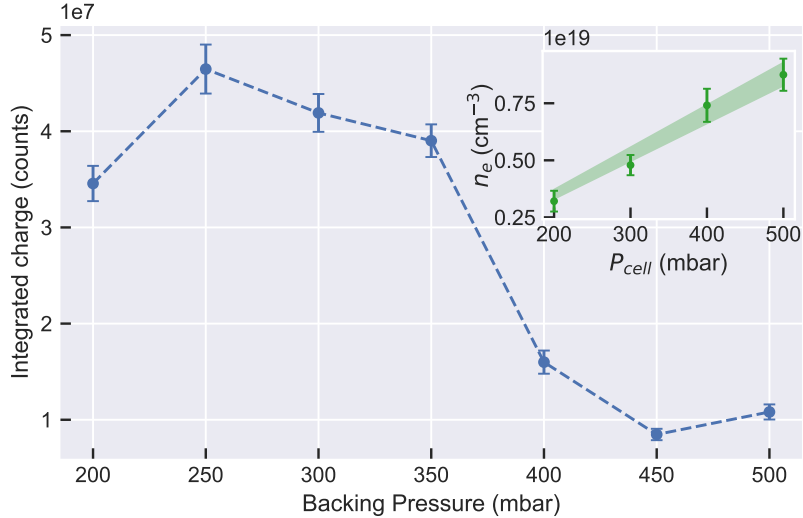
Figure 5.8: Total (uncalibrated) electron charge for each backing pressure. Inset: Relation between pressure and electron density from optical probe measurements.

probe data indicated a decrease in the density for a given pressure due to degradation of the exit nozzle of the gas cell. When this was replaced the measured density increased again. This effect is described in more detail in a CLF Annual Report by Finlay [152]. The electron and X-ray data presented here was taken over two consecutive days, and the daily variation in density was taken into account when analysing the results. A total of 280 shots were taken to commission and characterise the electron beam, with 148 selected for analysis. Shots for which the laser or gas system failed, or with no measurable electron signal, were not analysed. Table 5.2 shows the number of shots taken for each pressure setting. For each of the pressure settings, the electron spectra were averaged to obtain an estimate for a 'typical' profile for a given pressure. These spectra are shown in Fig. 5.5, with the standard error represented by the shaded regions.

A change in electron density affects both the maximum energy obtained and the
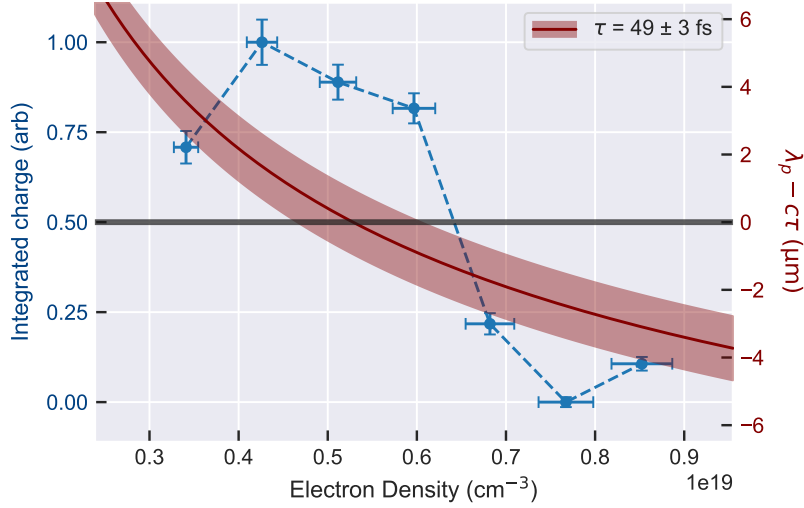
Figure 5.9: Variation in measured electron charge with density. The quantity $\lambda_p - c\tau_{las}$ is shown in red.

total charge in the bunch. The maximum energy is obtained by finding the highest energy electrons which are above a predetermined signal threshold, which in this case is $5\,\%$ of the peak signal. Fig. 5.6 illustrates the noise threshold for the mean electron spectra.

In this regime of LWFA, i.e. $a_0 \sim 1$, the maximum energy gain for an electron in the wake is given by $W_{max}(\mathrm{MeV}) \simeq 2m_e c^2 n_c/n_e$. As shown in Fig. 5.7, the maximum energy measured at each density agrees well with the prediction, although appears to fall short between $200\,\mathrm{mbar}$ and $350\,\mathrm{mbar}$.

We see a similar effect in the total charge in the electron beams. For density (pressure) between 200 and $350\,\mathrm{mbar}$ there is more charge than for 400 to $500\,\mathrm{mbar}$ (Fig. 5.8).

Both of these results indicate a change in the LWFA regime as we increase the electron density. All of the shots taken to characterise the electron beam were taken with the same laser parameters, i.e. focal spot profile, pulse length, and pulse energy (shot-to-shot fluctuations notwithstanding). We find that at a density of $n_e \simeq 5.3 \times 10^{18}\,\mathrm{cm}^{-3}$, the plasma wavelength λ_p corresponds to the pulse length $c\tau_{las}$. Plotting the difference $\lambda_p - c\tau_{las}$ in Fig. 5.9, indicates that the range of densities corresponding to the maximum charge, are also the values for which the laser pulse length is approximately equal to the plasma wavelength. In other words, at densities above $n_e \simeq 6.0 \times 10^{18}\,\mathrm{cm}^{-3}$, the pulse overfills the first wakefield period.

111

A consequence of this is that the pulse energy is split between the first two wake-field periods, reducing the electric field strength. The lower field strength causes fewer electrons to be injected due to wavebreaking and thus the accelerated charge is reduced. Moreover, the higher charge obtained from lower electron density suppresses the accelerating field, reducing the maximum energy. Deviation from the expected maximum energy for the low density shots may also be caused by insufficient acceleration length. Using the formula $L_{dph} \sim a_0(\lambda_p^3/\lambda_0^2)$ (Eq. 2.33), we find a dephasing length of $\sim 15\,\text{mm}$ at $200\,\text{mbar}$, and $\sim 11\,\text{mm}$ at $250\,\text{mbar}$. Electrons at these lower pressures would therefore not reach the maximum expected energy in an $11\,\text{mm}$ gas cell.

5.3.2 X-Ray Beam Characterisation

Here the basic characteristics of the X-ray beam are analysed and discussed. To fully describe the beam at the location of the sample, we require the spectrally-resolved photon flux and the divergence. Furthermore, we would also like to know the size of the beam at the source, which partly determines the maximum resolution of our imaging system (and also informs our divergence calculations).

The X-ray beam produced by various converters was measured using two scintillator materials which were placed in the beam path: An array of caesium iodide crystals arranged as shown in Fig. 5.2, and a flat LYSO crystal. Due to restrictions in the experimental geometry, it was not possible to operate the two scintillators simultaneously and so *direct* correlations between the measurements cannot be established. However, by aggregating the data from these diagnostics we may make useful, albeit less robust inferences about the character of the X-rays observed.

Additionally, as we shall see in Section 5.3.3, the respective pros and cons of the two detector types are to some degree complementary. That is to say one detector 'fills in the gaps' of the other.

Flux and Divergence

A pressure scan was conducted for each of the converter types under investigation, with 4 shots taken at each pressure setting. In the figures below, the data points represent the mean values of the shots and the error bars are the standard error in the mean.

The observed flux of X-rays (described in terms of counts due to lack of calibration)
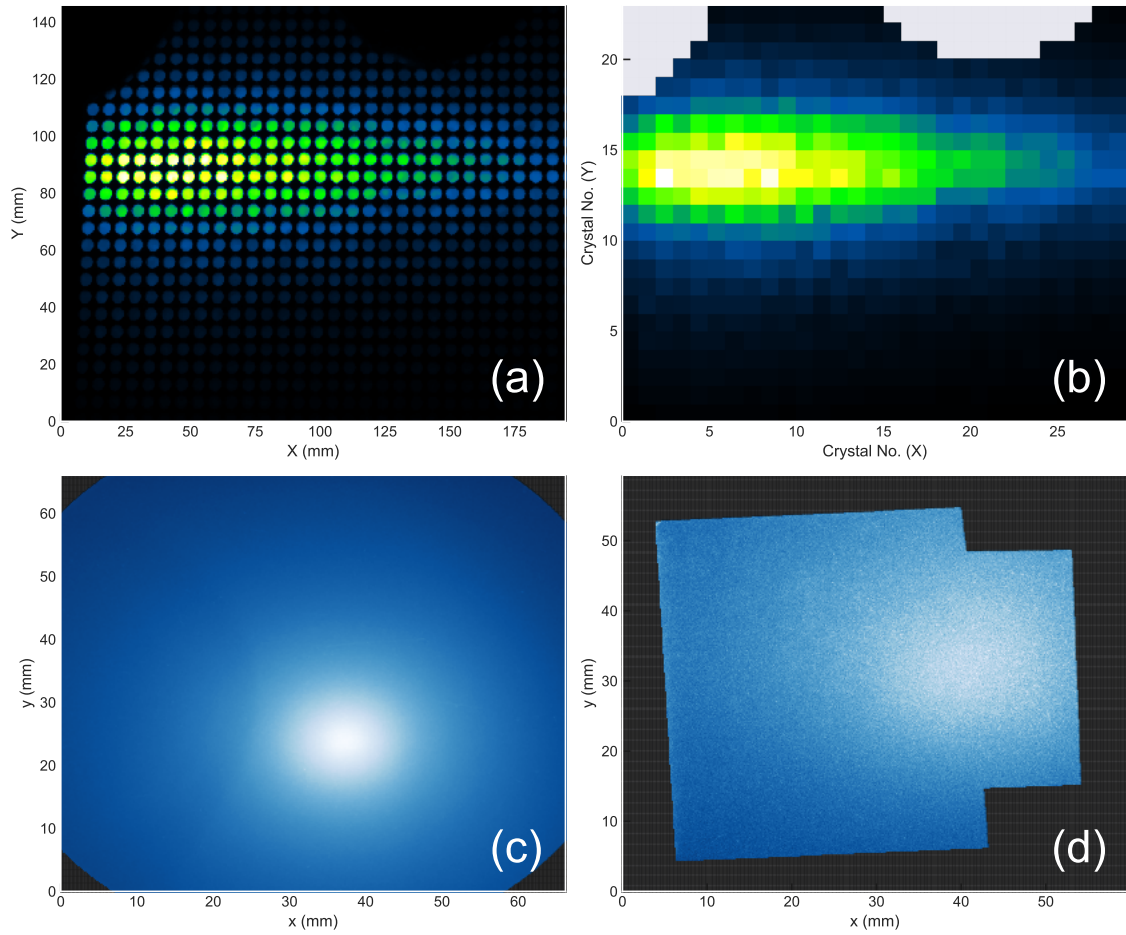
Figure 5.10: Images of X-ray beam incident on scintillators. (a) Transverse view of CsI stack showing attenuation of X-ray beam as it propagates through (left-to-right). (b) Processed image of (a). Each pixel represents the total signal in an individual crystal. (c) On-axis view of X-ray beam measured using 8 mm LYSO. (d) On-axis view using 2 mm LYSO.
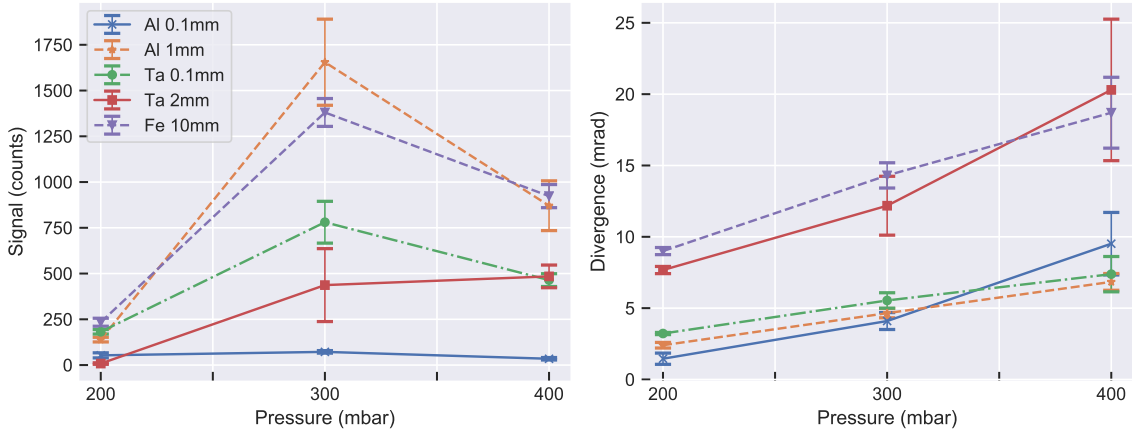
Figure 5.11: Observed characteristics of X-ray beam measured by CsI detector array. Left: Amplitude of signal as a function of gas cell pressure. Right: Divergence of X-ray beam, calculated from the FWHM of the signal.

is plotted against the backing pressure in Fig. 5.11 (Left). The behaviour here loosely follows that of the electron charge (Fig. 5.8), i.e. peaking at around 300 mbar, then dropping off slightly for higher pressures. We expect higher photon numbers with higher charge, simply due to a larger number of scattering events within the converter material. The results from iron and aluminium converters show a clear dependence of the width on the backing pressure (Fig. 5.11 Right). Incrementing the pressure appears to increase the observed divergence exponentially. An increase in backing pressure corresponds to an increased plasma density in the gas target, which is expected to produce higher numbers of low-energy electrons. In passing through the converter the emission angle of the low energy electrons is larger, resulting in a wider beam. Qualitatively, then, this increase in width with backing pressure is expected.

Monte-Carlo Simulations

The spectral characteristics of bremsstrahlung are determined by three factors: the areal density (ρR) of the material, its atomic number (Z), and the spectral shape of the incident electrons. As we cannot measure the electron beam directly while the converter target is in place, an estimate of the X-ray spectrum can be obtained by simulating the experimental conditions. Using the Monte-Carlo code GEANT4 [119], the average electron spectrum for each pressure setting was used to generate bremsstrahlung radiation from each of the converters.

Some illustrative results are shown in Figure 5.12. For a given converter type (e.g.

114
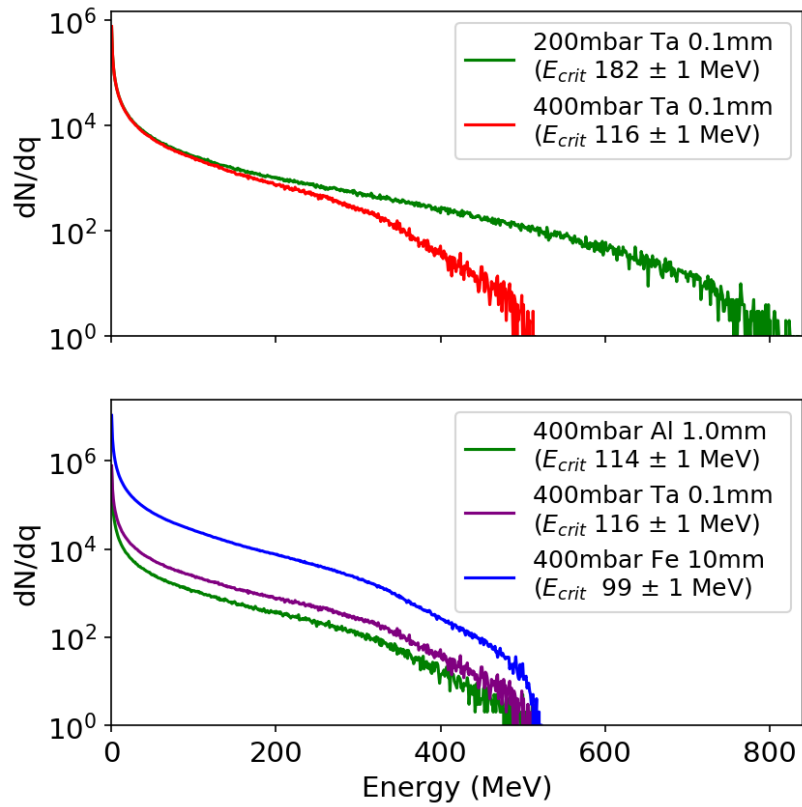
Figure 5.12: Simulation results from GEANT4. Top: Variation of backing pressure, and thus peak electron energy, corresponds to a change in the spectral shape of emitted X-ray beam. Bottom: Converters with higher $\rho R Z$ values produce higher flux for the same electron beam.

0.1 mm Ta), higher backing pressure reduces the maximum photon energy, since it is directly related to the electron energy. The vertical axis of Figure 5.12 is the number of photons per unit charge. As discussed above (Sec. 5.3.1), the backing pressure in combination with the pulse length influences the total electron charge produced, as well as the spectral shape.

A convenient metric for the bremsstrahlung spectrum is the critical energy, E_{crit}, defined as the photon energy below which 50 % of the total X-ray energy is emitted. An increase in ρR corresponds to an increased number of scattering events inside the material, which decreases the relative fraction of higher energy photons, and thus reduces E_{crit}.

5.3.3 X-Ray Detector Comparsion

The LYSO scintillator plate used in the experiment is conveniently shaped for sample imaging as it can capture the beam on-axis, which can then be relayed to a camera via a mirror (the camera is kept out of the beam path to avoid damage to the electronics). This is also useful for characterising the spatial properties of the beam, such as the source size, and the divergence angle.

One disadvantage of this arrangement, however, is that the spectral information is largely obscured. The scintillation probability of the LYSO is of course dependent on the energy of the incident X-ray photons, but the emitted photon is always in the same wavelength range. The energy of the original photon can *in principle* be determined if all the light is collected and the detector calibrated. In practice however, there are many photons incident on the detector in a short time period and the response becomes degenerate, i.e. the same light yield can be acheived by different X-ray spectral shapes.

It is possible to make some broad statements about the spectrum based on the emitted light, however. Scintillation occurs more readily for lower energy photons, with the majority of high energy (> 1 MeV) photons passing through undetected. We can therefore infer that the measured signal level is most indicative of the lower-energy portion of the spectrum.

By attentuating part of the beam with one or more filters, we can estimate the flux in higher-energy regions as well. However, it should be noted that this measurement may be confounded by the emission of electron-positron pairs or additional photons
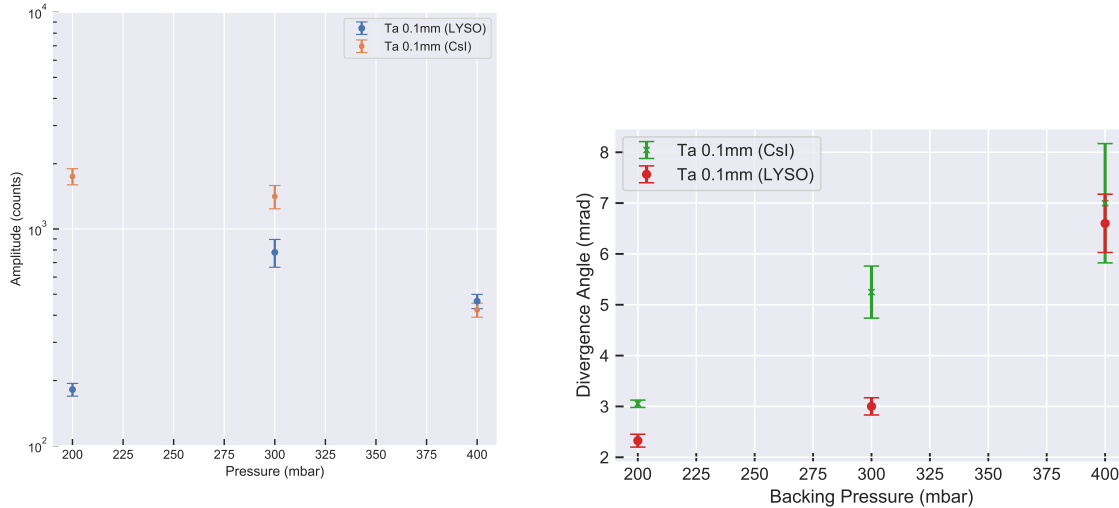
Figure 5.13: Comparison measured X-ray beam divergence between CsI and LYSO scintillators for 100 µm tantalum target.

produced in the interaction with the filter itself.

An improved spectral measurement can be made by observing the attenuation of the beam as it propagates through the detector. This is acheived with a stack of CsI crystals arranged in a grid formation. Each crystal is isolated from its neighbours by 1 mm of aluminium to prevent light leaking between crystals.

The caesium iodide stack is placed such that the incident beam interacts with each row of crystals in turn, and is thus attenuated at each stage. This offers more insight into the spectral components of the beam as the large volume of scintillator material is capable of stopping much higher energy photons than the thin LYSO crystal. In addition, the light emitted from each layer of the stack is related to the energy deposited. For details of the spectral retrieval for this experiment, see Underwood *et al.* [61].

A notable difference between the two detector types is the measurement of beam amplitude, and beam divergence, shown in Fig. 5.13. The CsI detector measures a larger signal and divergence than the LYSO, particularly at lower pressures. This is likely due to the construction of the detector, which contains aluminium spacers between each crystal. X-ray photons interacting with the aluminium will produce charged particles which induce further scintillation. The lower pressure settings tend to produce higher energy electrons, and thus X-rays, which will trigger particle cascades more readily in the aluminium.

117
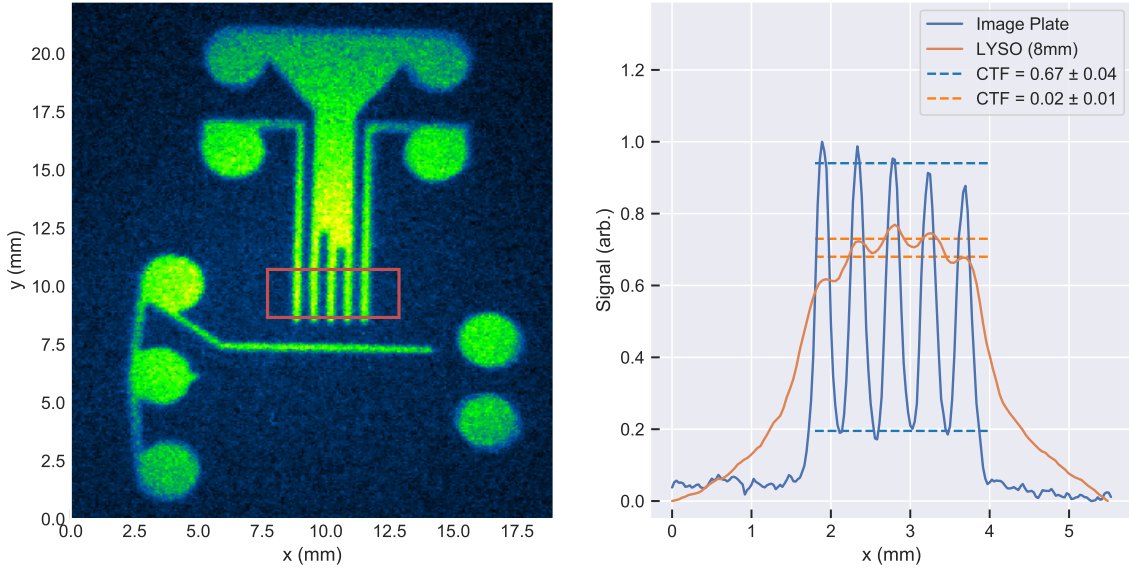
Figure 5.14: Comparison between image plate and LYSO. Left: X-ray image of tungsten resolution target on image plate. The features in the highlighted region are 200 µm wide. Right: Contrast values obtained using image plate (blue), and 8 mm LYSO (orange).

5.4 X-ray Imaging

A comparison between image plate, and two LYSO crystals of different thickness (8 mm and 2 mm) was carried out to assess the imaging capability of the source. A tungsten resolution grid was placed in the beam at position M2 ($M = 1.6$), with features of interest placed in the centre. Figure 5.14 shows an image of some coarse features of the grid taken using image plate. Each of the 'spikes' in the highlighted region is 200 µm wide, with 200 µm spacing between them. Since the image plate is typically sensitive to low energy X-rays in the range of several keV [153], the tungsten strongly attenuates the signal, producing a high contrast image with a CTF of $(67 \pm 4)\%$.

The thick LYSO crystal did not perform well here. Although the features are detectable, there was significant blurring, resulting in a contrast ratio of $(2 \pm 1)\%$. There are two reasons for this difference: The first is that the LYSO is sensitive to much higher energy photons (>100 MeV) than the image plate [118]. A larger proportion of these photons pass through the tungsten grid, and are detected by the LYSO. The second effect is that of scintillation light scattering inside the crystal. This creates a 'frosted glass' effect, whereby the image of the resolution grid is blurred out. Blurring from the crystal can be mitigated by reducing the thickness, however a thinner crystal
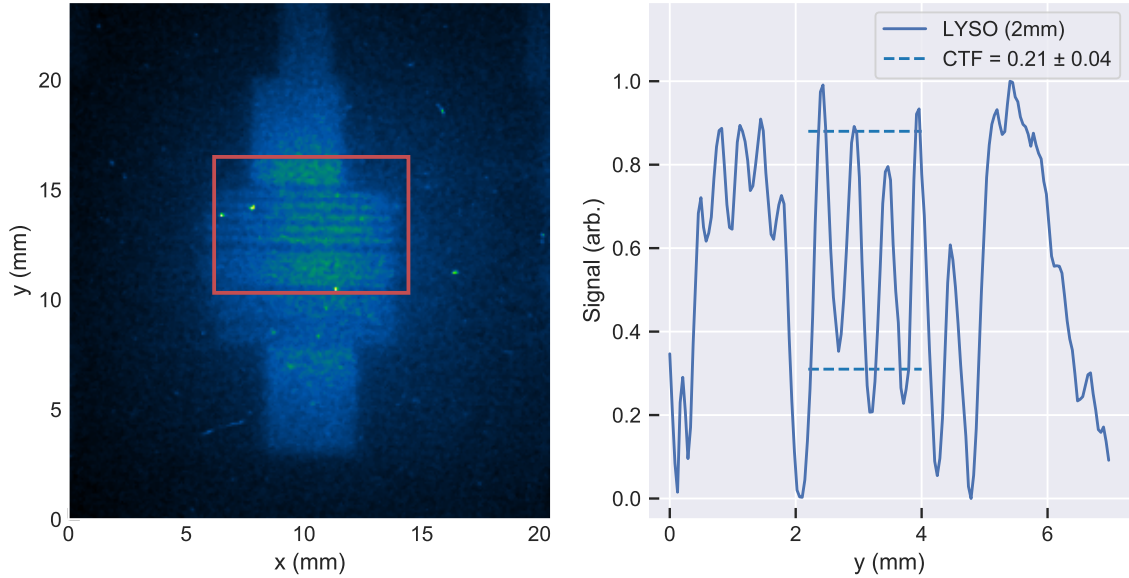
Figure 5.15: Fine features imaged on 2 mm LYSO. Left: Image of foil stack on resolution grid. Largest features in highlighted area are ~150 µm. Right: Contrast measured for 150 µm foils.

means photons have a lower probability to interact, which consequently reduces the signal. An image of some finer features of the resolution grid is shown in Figure 5.15. The largest of these is 150 µm, which was imaged with a contrast of $(21 \pm 4)\,\%$.

5.4.1 Industrial Sample Imaging

The development project was carried out in collaboration with a number of industrial partners, who provided samples of material to be imaged. One of these, supplied by the Manufacturing Technology Centre (MTC) is an additively-manufactured star-shaped object composed of inconel (nickel alloy). A photograph is shown in Figure 5.16. The star was approximately 5 cm tall, with a diameter of 5 cm. We placed the star in position M2 ($M = 1.6$) and imaged it along the longitudinal axis with a 2 mm LYSO crystal. Figure 5.17 is a single-shot acquisition of the star. The signal in the attenuated region is higher than the background, as seen in Figure 5.18, indicating that the X-ray beam was able to penetrate the full 5 cm of material.

Towards the end of the project, the star was placed on a rotation stage and imaged at a range of different angles with the aim of creating a tomographic reconstruction. Some projections are displayed in Figure 5.19. It was necessary to use the larger-diameter, 8 mm thick LYSO crystal to capture the full extent of the object, which

Figure 5.16: Photograph of Inconel star provide by MTC.
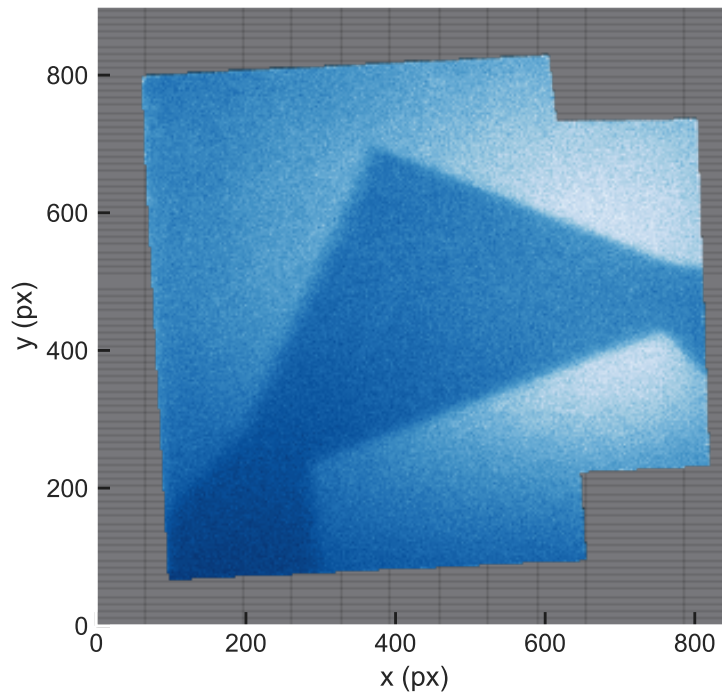
Figure 5.17: X-ray image of MTC star taken on 2 mm LYSO.
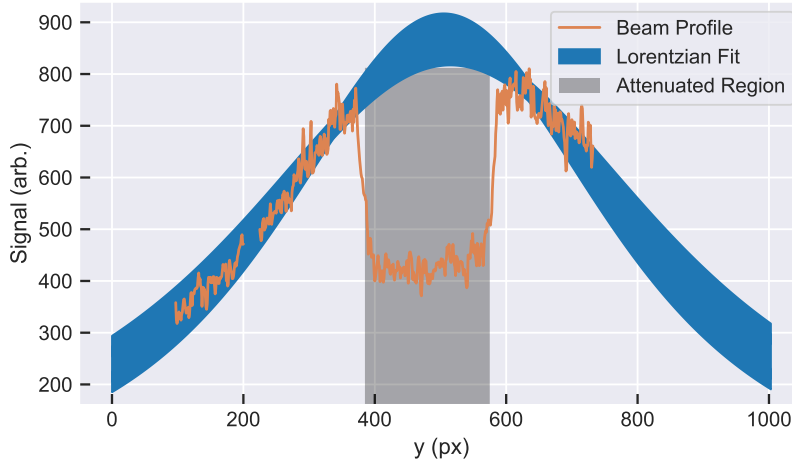
Figure 5.18: Attenuation of X-ray beam by MTC star. The centre profile of the beam is shown in orange. The blue line shows a fit to the beam profile to reconstruct the original shape.

sacrificed the resolution. Due to time constraints, we were unable to complete a full set of projections for a tomographic reconstruction, however the images in Figure 5.19 are promising, in that the X-rays are able to fully penetrate the object.

5.5 Discussion and Conclusion

The work presented here is based on data taken from a 3-week development-orientated experiment on Gemini. Unfortunately, due to the short timescale, some potentially useful measurements were not taken. It was not possible to properly calibrate the electron beam charge, nor the energy deposited in the scintillator diagnostics. Such measurements would have informed a more in-depth characterisation of the X-ray beams.

It is possible in principle to extract the X-ray spectrum from the caesium iodide stack [60] by simulating the detector response for monoenergetic photons and iteratively reconstructing the spectrum which produced the measured response. The results for this experiment are published by Underwood *et al.* [61].

Despite some incompleteness in the electron and X-ray characterisation, the results are promising from the perspective of industrial imaging. We were able to produce a source of high-energy bremsstrahlung X-rays which was able to penetrate a large volume of dense material. The imaging resolution was limited to around 150 µm by the choice of detector, but this is already a significant improvement on the industry standard of 1 mm. With improved detectors, it is not unrealistic to expect an order of
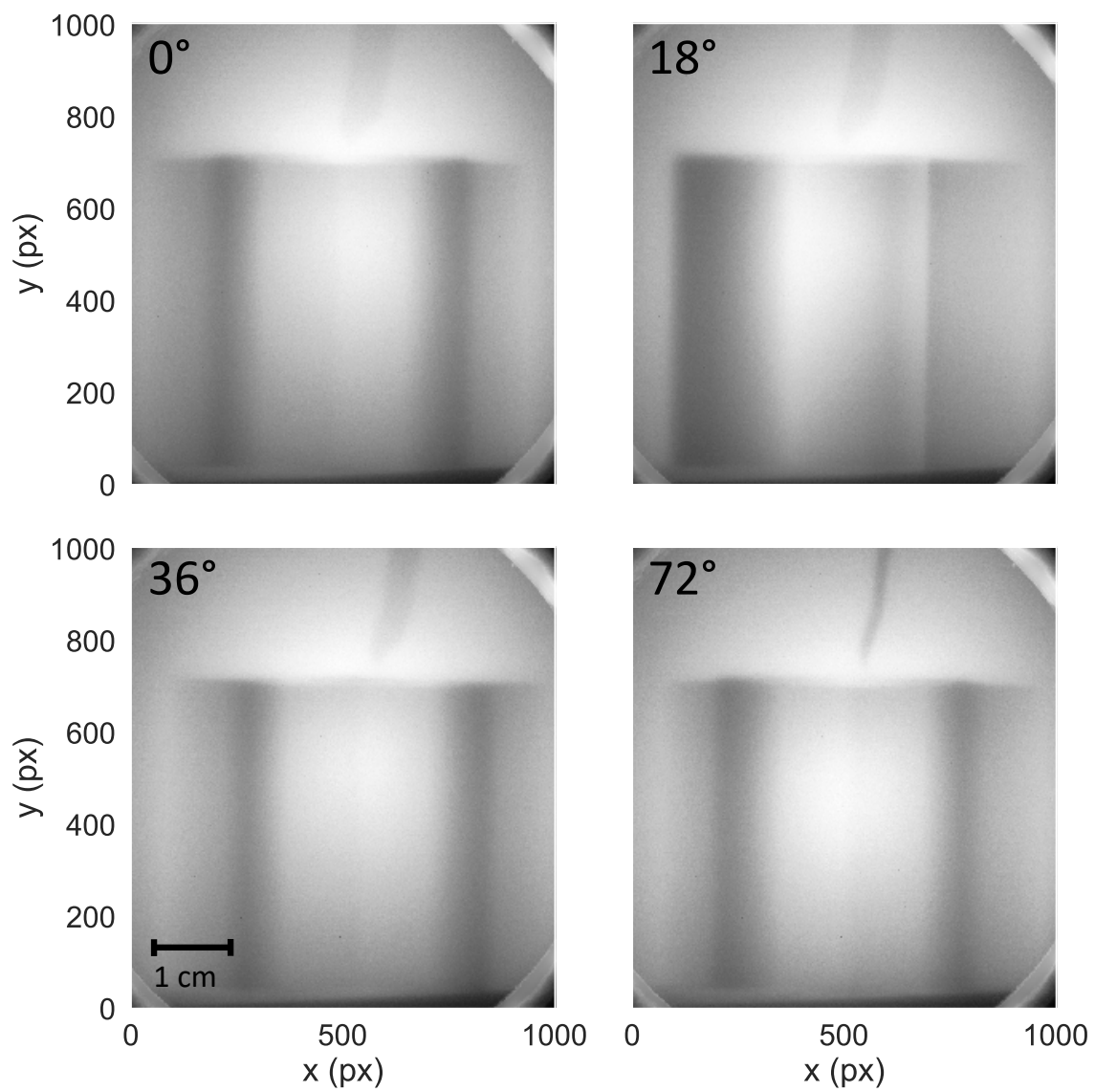
Figure 5.19: Projections of the star taken using 8 mm LYSO.

magnitude improvement on this result.

In addition to the high resolution, we have also demonstrated that the X-ray characteristics, i.e. photon number, divergence, and critical energy, can be manipulated by simply varying the pressure inside the gas cell, or changing the converter.

A limitation of Gemini for industrial use is its slow repetition rate. However, technological advances mean that facilities operating in the near future, such as ELI, and EPAC will be capable of $10\,$Hz repetition at significantly higher peak powers. Similar advances applied to smaller systems mean we can expect repetition rates approaching $1\,$kHz, which would enable efficient tomographic scanning. An X-ray source driven by such a system would be superior to a conventional source in almost every respect.

The work presented here demonstrates the utility of laser-driven X-ray sources for real-world applications. Furthermore, the simplicity of operation combined with high-quality imaging capabilities mean that laser-driven sources may rapidly become the industry standard.

5.6   Acknowledgements

Chapter 6

Scintillators as High-Energy X-ray Detectors

This chapter describes the development of X-ray detectors for applications to high-power laser experiments. Measurement of high-energy X-rays is critical for diagnosing X-ray sources like the one in Chapter 5, but also in cases such as the one described in chapter 4; Measuring radiation reaction effects in electron beams also requires information about the X-rays generated to corroborate the results.

The purpose of this chapter is not to present groundbreaking research, but rather to highlight the development process of experimental diagnostics. Each of the detectors described here is based on thallium-doped caesium iodide (CsI (Tl)) crystals.

6.1 Compact Scintillator Modules

The interaction of a laser with a solid target produces streams of hot electrons, energetic protons and ions, as well as hard X-rays via bremsstrahlung. In ion acceleration research, for example, the X-ray flux is a good indicator of how much laser energy has been coupled into the target. Maximising this parameter is important for optimising ion sources.

Emission from solid targets is also directional [154–156] with an angular distribution depending on the target geometry. The ability to measure X-rays at multiple points allows angular resolution of this emission, providing useful information about the interaction.
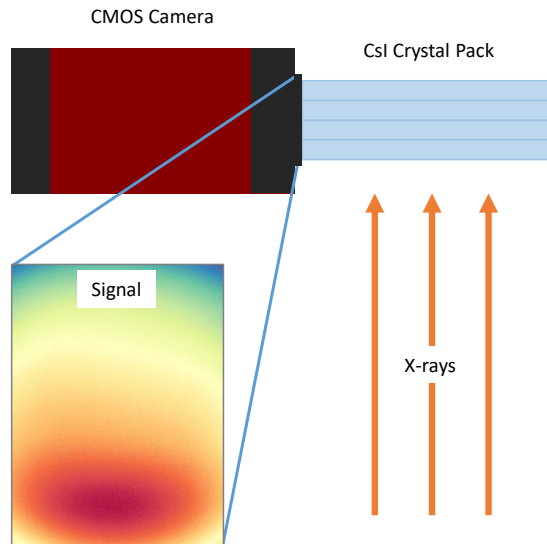
Figure 6.1: Schematic of the Mk. I scintillator module. A 4×3 array of CsI crystals is coupled to a camera sensor, enabling measurement of X-ray flux and directionality. Lack of imaging system prevents resolution of the individual crystals making spectral reconstruction impossible.

Some compact scintillator modules were designed for use on a Vulcan TAP experiment in 2017 to aid in the investigation of the effect of target micro-structure on the efficiency of proton sources. The results of this campaign are described by Jarrett *et al.* and Ebert *et al.* [157, 158].

The design was improved upon for a subsequent experiment, also on Vulcan TAP, which aimed to optimise hot-electron production using resistive guiding [159]. This technique is applicable to studies of hot dense matter, including the fast-ignition method of inertial fusion [160, 161].

6.1.1 Mk. I

A schematic of the first iteration of the compact modules is shown in figure 6.1. A small array of CsI crystals is placed in contact (or as close as possible) to the sensor of a camera. The unit is then light shielded and placed such that X-rays strike the crystals laterally.

To construct the crystal pack, 12 CsI crystals each measuring $5 \times 5 \times 50$ mm are individually wrapped in foil and assembled in a 4×3 array, as shown in figure 6.2. The foil around each crystal serves mainly to optically isolate each crystal, minimising cross-talk. It also internally reflects light produced inside the crystals, increasing the

Figure 6.2: Construction process of the Mk. I module. Left: The crystals are individually wrapped in foil, then assembled into the required shape. Middle: Crystal pack is mounted to the camera, as close to the sensor as possible. Right: Light shielding is added to minimise background noise.

light which reaches the end of the crystal.

The completed module is shown in figure 6.2. Here we used an AV Manta G-235B camera to capture the scintillator light. The camera is triggered 50 ms before the laser fires, and integrates for 100 ms. The long exposure time is not strictly required to capture the scintillator light, which decays in around 1 µs [162], but is chosen to account for uncertainty in the laser trigger timing. With adequate light shielding, background noise is minimised.

Experimental Data
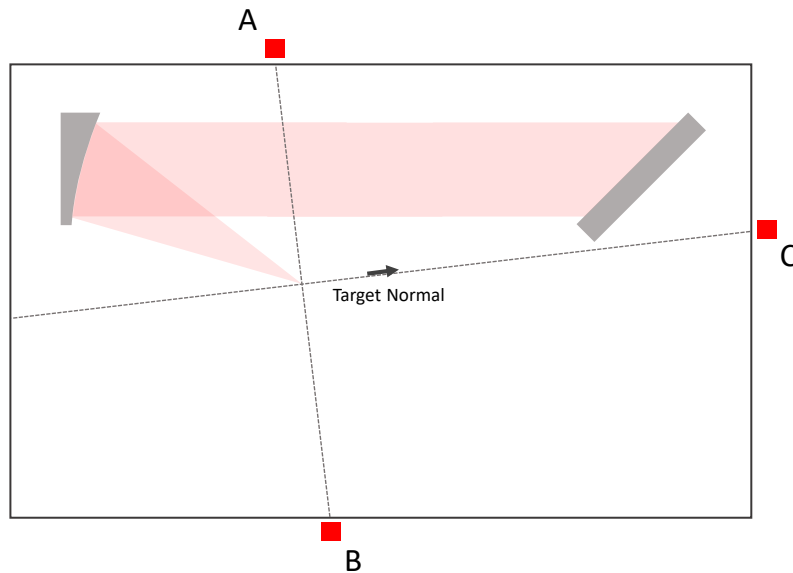
Figure 6.3: Placement of Mk. I scintillator modules on Vulcan TAP experiment. The positions were chosen to match the regions of highest flux expected from the interaction.

Three Mk. I scintillators were used for the duration of the experiment, placed
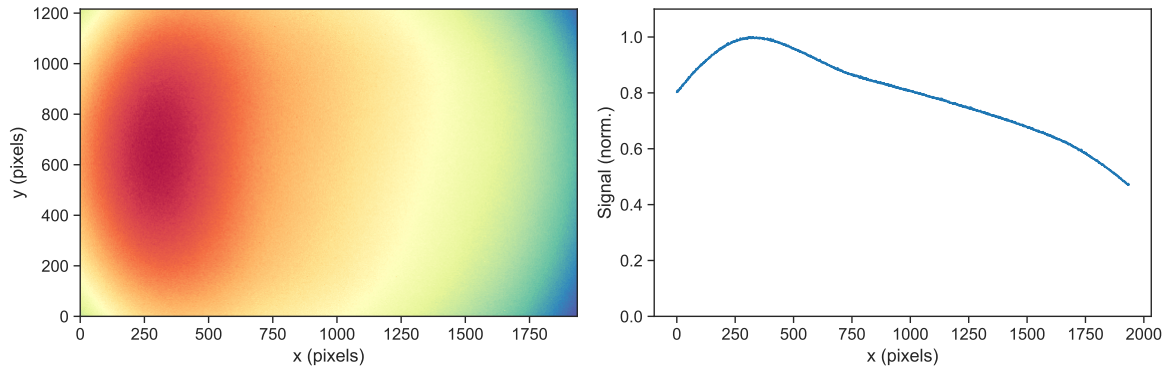
Figure 6.4: Example signal from Mk. I module. The direction of incoming xrays is evident, and the total signal can be integrated to give a measure of the flux. Left: Raw data from one module (filter applied to remove hard-hits). Some vignetting is apparent from the relative size of the crystal pack compared to the sensor. Right: Signal integrated along transverse axis (y).

around the outside of the interaction chamber in the arrangement in figure 6.3. The positioning was chosen to capture the highest X-ray flux, which is expected from the back (and front) surface of the foil, as well as the edges.

An example image from one of the scintillators is shown in figure 6.4. Despite the lack of an imaging system, the attenuation of the X-ray signal along the propagation axis is evident. There is too little information to reconstruct accurate spectral information here, but the total flux can be estimated by integrating the signal across the chip.

The aim of this experiment was to determine the effect of micro-structured targets on the efficiency of a proton source. These scintillators provided a measurement of X-ray flux, which although uncalibrated, facilitated comparison of the laser-target energy coupling for the different target types. Figure 6.5 shows the analysis of 13 shots comparing flat foils with structured targets. It can be seen from the top subplot that the scintillators 'A' and 'B' are largely consistent with each other, but 'C' shows very little signal until shot 71. This was found to be caused by a misplacement of the scintillator, rather than the interaction itself.

The lower three figures, representing scintillators 'A', 'B', and 'C' from top to bottom, show an overall increase in signal for the structured target shots compared to those with flat targets. This was consistent with results gathered from an X-ray crystal spectrometer, and the Thomson spectrometer [158].

The simplicity of construction and installation of the Mk. I module makes it useful
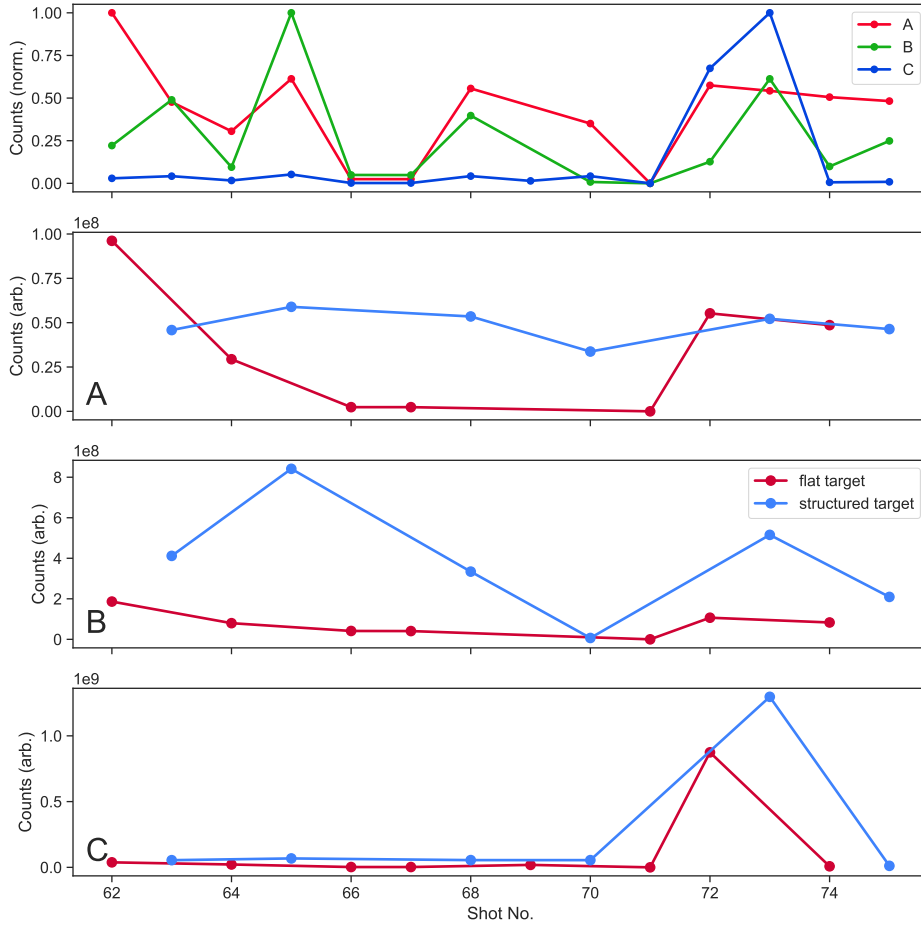
Figure 6.5: Summary of a dataset comparing flat foil targets with micro-structured targets. Top: Normalised signal level for all 3 scintillators for 13 shots. Scintillator 'C' underperforms until shot 71 due to misplacement. Bottom (3): Individual scintillator signals for flat vs. microstructured targets. Signal for the structured targets is generally higher than for non-structured, indicating improved energy coupling.

for a 'quick and dirty' measurement of X-ray flux, however there are some obvious improvements that could be made to the design.

6.1.2 Mk. II
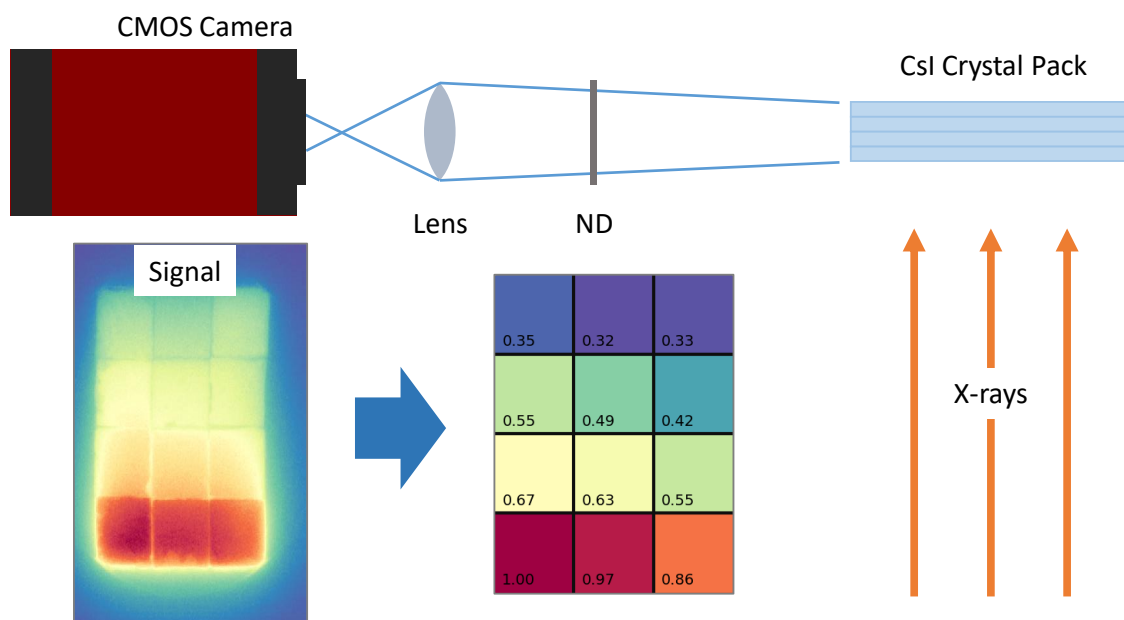
Figure 6.6: Mk. II scintillator module. The operating principle is similar to the Mk. I, but the inclusion of a single lens imaging system allows for resolution of the individual crystals.

An improved design, the Mk. II, uses a single lens to image the crystal pack onto the camera sensor. This enables resolution of the individual crystals in the array, and in principle allows for spectral information to be deduced by making use of tabulated attenuation values [118]. Figure 6.6 illustrates the operating principle. The addition of a lens increases the amount of light reaching the sensor, so an ND filter is included to prevent saturation. These extra components increase the size of the module to around 30 cm, but the design is still reasonably compact. The extra length also allows the camera to be placed behind shielding, reducing the number of hard-hits. Some photographs of the placement of the Mk. II units are shown in figure 6.7.

Experimental Data

Six of the Mk. II scintillators were tested on an electron transport experiment on Vulcan TAP in 2017. The aim was to assess their usefulness in measuring the angular

Figure 6.7: Photograph of some Mk. II scintillator modules in place outside Vulcan TAP interaction chamber.
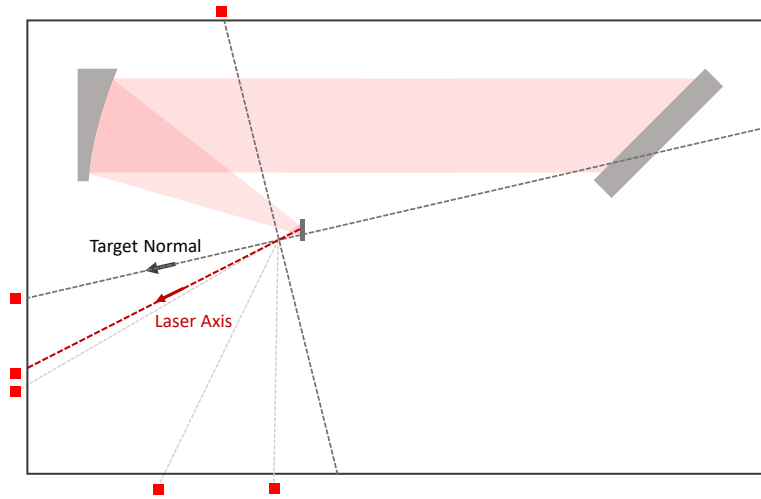
Figure 6.8: Placement of 6 Mk. II modules around the TAP interaction chamber.

distribution of X-rays from the main interaction. Figure 6.8 shows the location of each scintillator with respect to the interaction. One was placed along the target normal direction, one directly along the laser axis, with a second offset by 2°. Three more were placed at semi-regular intervals intersecting the axis perpendicular to the target. Placing the scintillators inside the interaction chamber was problematic due to EMP effects, so each scintillator was mounted on a convenient point outside the chamber. Each scintillator requires an unobstructed line-of-sight to the target to capture the X-ray emission, which in practice requires placement outside thin aluminium flanges (see figure 6.7) or fused silica windows in order to minimise attenuation.

An image taken from one of the scintillators is shown in figure 6.9. The left subplot is the raw data (after filtering hard-hits), and the right shows the normalised signal in each crystal. In principle, spectral information can be derived from this data by first calibrating the scintillators with a radioactive source, and then using a simulation package (e.g. GEANT4 [119]). However, this was not possible due in part to time
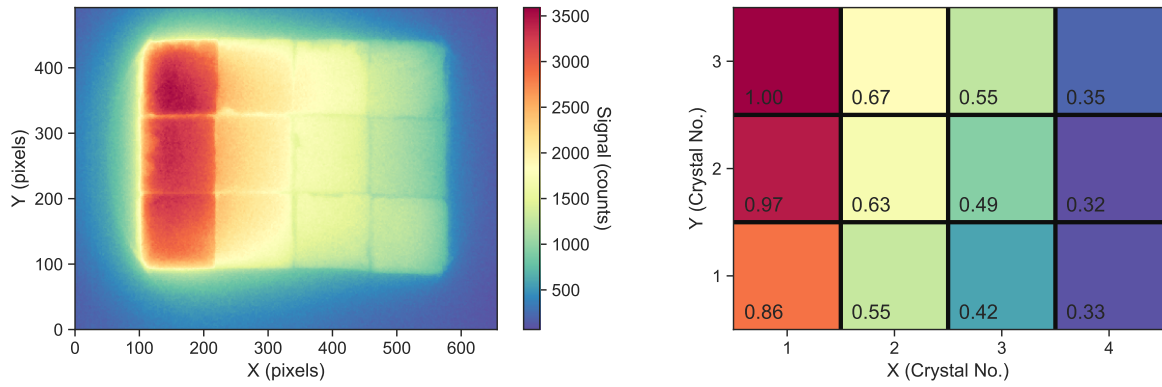
Figure 6.9: Example signal from a Mk. II scintillator. Left: Each crystal is clearly visible, and the attenuation across the columns is apparent. Right: Processed image showing relative signal level in each crystal.
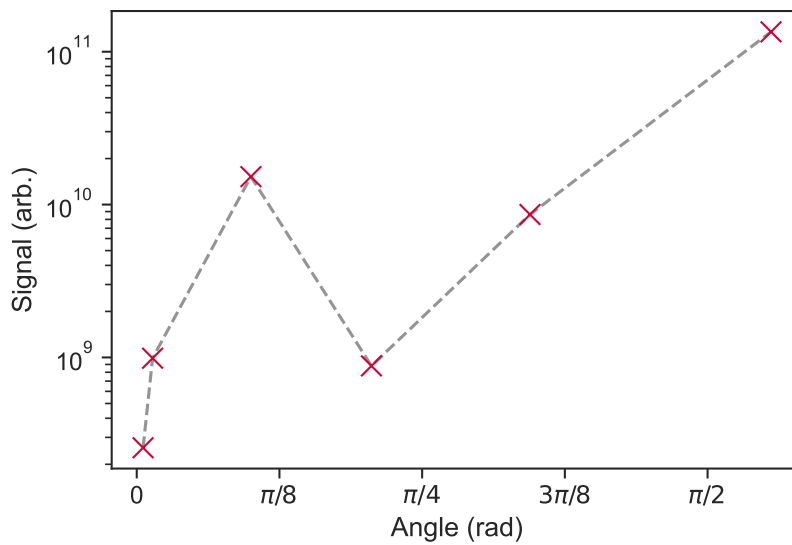
Figure 6.10: X-ray flux as a function of angular position around the interaction. 0° corresponds to the laser axis. The peak at 18° approximately matches the target angle of 13°; this is due to emission from the rear surface.

constraints, but also to limitations of the setup which are discussed in the next section. Despite the lack of calibration, the flux distribution shown in figure 6.10 indicates a clear angular dependence of the signal level. A peak occurs close to the target normal axis of 13°, and there is a high signal region at around 90°. There is not enough information here to resolve a second peak, but it is expected to occur at 103° from the laser axis, i.e. perpendicular to the target surface.

6.1.3 Limitations of Compact Scintillators

As we have seen, the compact scintillator units provide useful information for characterising X-ray emission. Their simplicity and small form-factor makes them suitable for installation in many experimental setups without imposing on primary diagnostic space.

The overall utility is somewhat limited, however. Retrieving spectral information is possible in principle with the Mk. II iteration, although with the configuration described analysis would be confounded by the emission of hot electrons. Without separating electrons from the X-ray beam, e.g. by use of a small dipole magnet, we cannot know what proportion of the scintillation light is due to electrons. That said, these modules could easily be modified include such a feature.

Since we rely on absorption of X-rays by the scintillator, spectral measurements with a crystal array of this size would be limited to X-rays of less than $0.5\,\mathrm{MeV}$. Above this energy, over $90\,\%$ of the incident X-rays are transmitted through the stack. This design could therefore be improved by lengthening the crystal array along one axis to increase absorption. A compact spectrometer of this form has been developed by Rusby *et al.* [59].

6.2 Large CsI Spectrometer

X-ray emission from solid target interactions has an angular distribution which extends to all angles around the target. For such interactions, a number of small scintillators placed around the target can allow reconstruction of the emission profile. Other experiment types require a different approach. In the previous two chapters we focused on applications of laser wakefield acceleration: Radiation reaction measurements, and bremsstrahlung sources. In both cases we expect bright X-ray beams directed along the laser axis, with an opening angle of a few tens of milliradians at most. In addition, these X-ray beams can reach hundreds of MeV in energy. To characterise this type of X-ray beam, we can use a single, large array of scintillating crystals with sufficient depth to attenuate high energy X-rays. A large CsI array, consisting of 1551 crystals (33×47) was developed at the Central Laser Facility for this purpose [60]. A schematic is shown in figure 6.11. The crystals, each $5 \times 5 \times 50\,\mathrm{mm}$ are held inside an aluminium
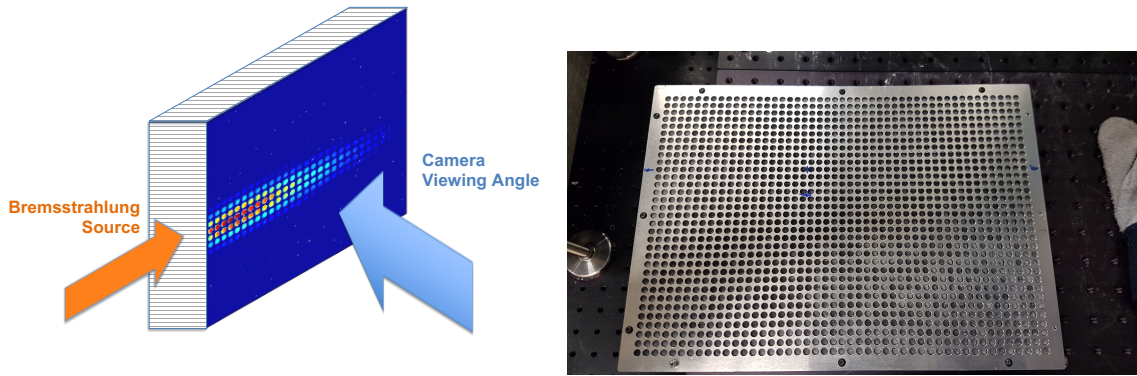
Figure 6.11: Large CsI array for high-energy X-ray diagnosis. Left: Schematic array of CsI. Right: Photograph of array in-situ.

array, with 1 mm of aluminium between each one to prevent light leakage.

This detector was used in the radiation reaction experiments described by Cole *et al.* [42], and also in the experiment discussed in Chapter 5. It operates in much the same way as the compact modules above; by progressively attenuating X-rays and capturing scintillation light with a camera. The large size means that X-rays of up to 500 MeV are stopped, which is sufficient for characterising bremsstrahlung sources and the high-energy X-rays emitted in strong field interactions.

Spectral retrieval requires modelling of the detector using a simulation package. The full process is described by Behm *et al.* , but is essentially an iterative fitting routine. First the expected X-ray spectrum is calculated using knowledge of the driving electron beam. The detector response is then modelled for monoenergetic photons in the expected range. Response for each energy bin is then combined in a weighted sum to generate an estimated response to the calculated spectrum.

The next step is to compare the calculated response to the experimental data. By perturbing the calculated spectrum and assessing the fit at each step, the measured spectrum can be extracted. As well as the results by Cole *et al.* , this method was also used to extract spectral characteristics of the bremsstrahlung source described in Chapter 5, and published by Underwood *et al.* [61].

6.3 Dual-Axis Spectrometer

For strong-field inverse Compton interactions as in Chapter 4, the scattered X-ray beam has a degree of ellipticity [163]. For a scattering laser polarised along the x-axis,
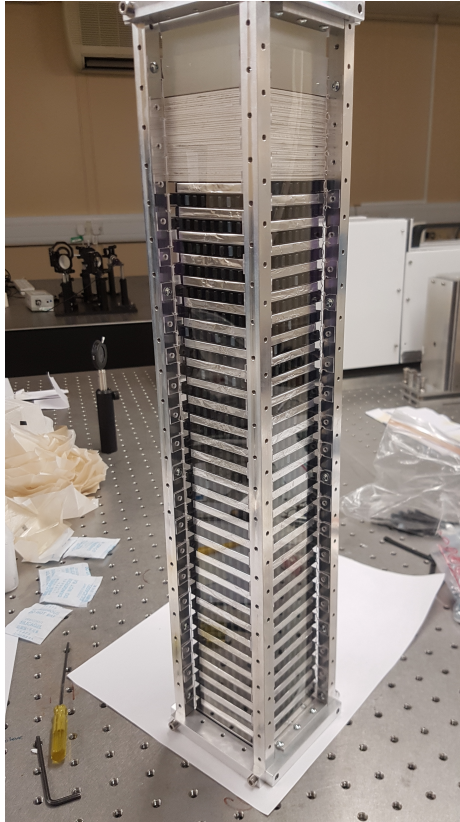
Figure 6.12: Completed dual-axis spectrometer.

the angular profile of the beam is expected to be larger in the y-axis by a factor of a_0. The ellipticity could be measured with a detector like the one described in the previous section, simply by rotating it by 90°. By modifying the design, however, we can obtain both the spectral information and the ellipticity with a single detector. Rather than having all the crystals in the same orientation, rotating every second row by 90° turns the detector into something resembling a Jenga tower (figure 6.12). This allows us to view the signal from four positions, and in principle to reconstruct the shape of the beam in three dimensions (two spatial and one energy).

Each layer of the detector consists of 10 CsI crystals separated by 1 mm polyethylene (PE) spacers for light-shielding. The layer is then wrapped in reflective aluminium foil (figure 6.13). Each layer is separated by 1 mm of rubber. Once constructed the layers are compressed, which pushes the protruding edges into the rubber creating a light-tight seal. The whole structure is held inside an aluminium frame with transparent polycarbonate sheets for viewing. The initial design used 60 layers of crystals, which should absorb approximately 90 % of 1 GeV photons. This makes it suitable for use in RR experiments.
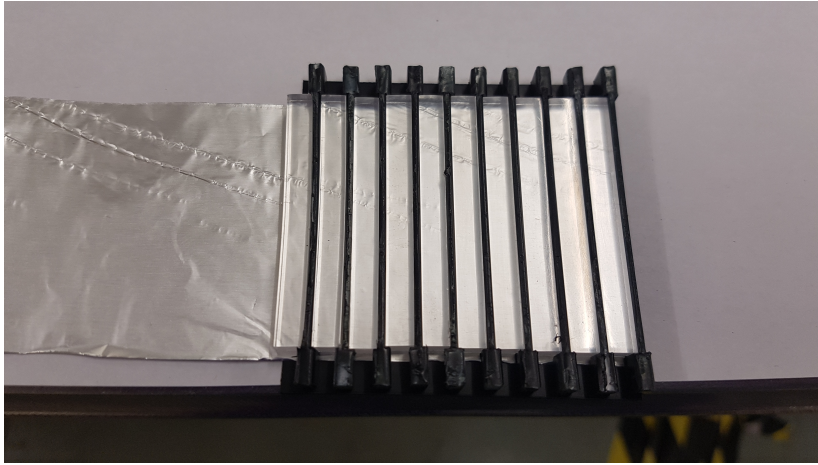
Figure 6.13: One layer of the spectrometer consisting of 10 crystals separated by PE spacers.

6.4 Summary and Outlook

In this chapter we have seen three designs of X-ray detector based on CsI (Tl) crystals. The first design is compact and simple to construct, making it useful for characterising X-ray flux on laser-solid target interactions, including measuring angular distributions. Some improvements are required to allow spectral information to be retrieved from this design, however this would be a straightforward modification to the design.

The larger, "2-dimensional" array for measuring high-brightness, directional X-ray sources, including those relevant to strong-field interactions is capable of detecting photons up to 500 MeV and characterising the angular shape in one dimension. For laser-driven X-ray sources, such as the one described in Chapter 5, this is sufficient since the source is radially symmetric.

The 2D CsI array is improved upon by rotating every second row of crystals by 90°. The stack can then be viewed from all four sides, allowing a full 3D reconstruction of an X-ray beam. This could prove extremely useful in the detection of quantum effects in radiation reaction experiments, since the resulting X-ray beam has a degree of ellipticity which is related to the laser a_0. At the time of writing, the dual-axis spectrometer is untested, so no verification of its properties yet exists. Modelling of the detector indicates that it should be capable of detecting photons of over 1 GeV with the 60 layers in the current design. The design is also easy to modify to include additional layers, potentially extending the detection capabilities even further.

Chapter 7

Conclusion and Outlook

The results presented in this thesis relate to the use of laser wakefield accelerators as an instrument of research in two seemingly unrelated fields of study. With the steady march of technological advancement, the available laser intensity will inevitably increase well into the QED regime, and so the understanding of the mechanisms at work is critical, not only for verifying theoretical calculations, but also for development of applications.

Single-Shot Measurements of Radiation Reaction

In Chapter 4 we saw that the geometry of inverse Compton scattering is useful for eliciting radiation reaction effects with currently available lasers. While this has been demonstrated experimentally, the results lacked the precision required to compare classical and quantum models of electron motion, in large part due to the shot-to-shot variation of LWFA electron beams.

This difficulty can be overcome by making single-shot measurements, i.e. by engineering electron beams such that only part of the bunch interacts with the scattering laser pulse, thus preserving the original spectrum. This is achieved by simply allowing the electron beam to propagate a short distance before interaction, which has the effect of establishing a phase-space correlation. Electrons inside and outside the interaction region therefore remain in the same relative position after the collision.

The effectiveness of this method depends strongly on the electron beam characteristics. The ideal electron beam is one which has high energy, i.e. above $1\,\mathrm{GeV}$, and low divergence. Due to the finite sensitivity of diagnostics, the geometry of the electron

spectrometer also plays a crucial role in detecting the radiation reaction signal.

Although this method has yet to be tested experimentally, the simulation results are promising, and have taken into account a range of experimental factors which could otherwise hinder the measurement.

Bremsstrahlung Imaging of Industrial Materials

Radiography is a crucial diagnostic for quality control in industry. Linac based X-ray sources are the current standard for non-destructive testing, but are limited by poor resolution and physical scale. Both of these limitations can be overcome by laser-driven sources, which offer order of magnitude improvement on both fronts. The results presented in Chapter 5 show how a LWFA electron source can be used as a bremsstrahlung radiography tool. Since the bremsstrahlung radiation spectrum is related to the electron beam parameters and the converter material, the source can be easily tuned for different materials. It was shown that the source is capable of resolving features smaller than $150\,\mu m$ at magnification $M < 2$. This simplicity of operation and high resolution is a key feature that will make laser-driven X-ray sources attractive to manufacturers. A commercial system built to the same specifications would also be significantly more compact than the current industry standard.

Scintillators as High-Energy X-ray Detectors

A key area of overlap between the results in Chapters 4 and 5 is the reliance on high-energy X-ray diagnostics. In order to keep up with the high repetition rate of current (and future) laser-driven sources, the development of fast, scintillator-based diagnostics is essential. Chapter 6 shows the development of CsI (Tl) scintillator diagnostics and the versatility with which they can be used. The same crystals can be used in a variety of configurations to observe the directionality of X-rays emitted from solid targets, measure the spectrum of bremsstrahlung sources, or to detect strong field QED effects.

Bibliography

[1] C. D. Baird, C. D. Murphy, T. G. Blackburn, A. Ilderton, S. P. D. Mangles, M. Marklund, and C. P. Ridgers. Realising single-shot measurements of quantum radiation reaction in high-intensity lasers. *New Journal of Physics*, 21(5):053030, 2019. ISSN 1367-2630. doi: 10.1088/1367-2630/ab1baf.

[2] T. Behnke, J. E. Brau, B. Foster, J. Fuster, M. Harrison, J. M. Paterson, M. Peskin, M. Stanitzki, N. Walker, and H. Yamamoto. The International Linear Collider Technical Design Report - Volume 1: Executive Summary. *arXiv*, jun 2013. URL http://arxiv.org/abs/1306.6327.

[3] JAHEP ILC Steering Panel. URL jahep-ilc.org.

[4] V. I. Veksler. Coherent principle of acceleration of charged particles. In *CERN Symposium on High Energy Accelerators and Pion Physics*, pages 80–83, 1956. doi: 10.5170/CERN-1956-025.80. URL http://cds.cern.ch/record/1241563.

[5] I. Blumenfeld, C. E. Clayton, F.-J. Decker, M. J. Hogan, C. Huang, R. Ischebeck, R. Iverson, C. Joshi, T. Katsouleas, N. Kirby, W. Lu, K. A. Marsh, W. B. Mori, P. Muggli, E. Oz, R. H. Siemann, D. Walz, and M. Zhou. Energy doubling of 42 GeV electrons in a metre-scale plasma wakefield accelerator. *Nature*, 445(7129): 741–744, 2007. ISSN 0028-0836. doi: 10.1038/nature05538.

[6] T. Tajima and J. M. Dawson. Laser electron accelerator. *Physical Review Letters*, 43(4):267–270, 1979. ISSN 00319007. doi: 10.1103/PhysRevLett.43.267.

[7] D. Strickland and G. Mourou. Compression of Ampified Chirped Optical Pulses. *Optics Communications*, 55(6):447–449, 1985. ISSN 00304018. doi: 10.1016/0030-4018(85)90151-8.

[8] C. E. Clayton, C. Joshi, C. Darrow, and D. Umstadter. Relativistic Plasma-Wave Excitation by Collinear Optical Mixing. *Physical Review Letters*, 54(21): 2343–2346, may 1985. ISSN 0031-9007. doi: 10.1103/PhysRevLett.54.2343. URL https://link.aps.org/doi/10.1103/PhysRevLett.54.2343.

[9] N. A. Ebrahim, F. Martin, P. Bordeur, E. A. Heighway, J. P. Matte, H. Pepin, and P. Lavigne. First observations of acceleration of injected electrons in a laser plasma beatwave experiment. In *Linear Accelerator Conference Proceedings*, 1986.

[10] M. N. Rosenbluth and C. S. Liu. Excitation of Plasma Waves by Two Laser Beams. *Physical Review Letters*, 29(11):701–705, sep 1972. ISSN 0031-9007. doi: 10.1103/PhysRevLett.29.701. URL https://link.aps.org/doi/10.1103/PhysRevLett.29.701.

[11] Y. Kitagawa, T. Matsumoto, T. Minamihata, K. Sawai, K. Matsuo, K. Mima, K. Nishihara, H. Azechi, K. Tanaka, H. Takabe, and S. Nakai. Beat-wave excitation of plasma wave and observation of accelerated electrons. *Physical Review Letters*, 68(1):48–51, 1992. ISSN 0031-9007. doi: 10.1103/PhysRevLett.68.48.

[12] C. E. Clayton, K. A. Marsh, A. Dyson, M. Everett, A. Lal, W. P. Leemans, R. Williams, and C Joshi. Ultrahigh-gradient acceleration of injected electrons by laser-excited relativistic electron plasma waves. *Physical Review Letters*, 70 (1):37–40, jan 1993. ISSN 0031-9007. doi: 10.1103/PhysRevLett.70.37. URL https://link.aps.org/doi/10.1103/PhysRevLett.70.37.

[13] M. Everett, A. Lal, D. Gordon, C. E. Clayton, K. A. Marsh, and C. Joshi. Trapped electron acceleration by a laser-driven relativistic plasma wave. *Nature*, 368(6471):527–529, apr 1994. ISSN 0028-0836. doi: 10.1038/368527a0. URL http://www.nature.com/articles/368527a0.

[14] J. Krall, A. Ting, E. Esarey, and P. Sprangle. Enhanced acceleration in a self-modulated-laser wake-field accelerator. *Physical Review E*, 48(3):2157–2161, sep 1993. ISSN 1063-651X. doi: 10.1103/PhysRevE.48.2157. URL https://link.aps.org/doi/10.1103/PhysRevE.48.2157.

[15] A. Modena, Z. Najmudin, A. E. Dangor, C. E. Clayton, K. A. Marsh, C. Joshi, V. Malka, C. B. Darrow, C. Danson, D. Neely, and F. N. Walsh. Electron acceleration from the breaking of relativistic plasma waves. *Nature*, 377(6550): 606–608, oct 1995. ISSN 0028-0836. doi: 10.1038/377606a0. URL http://www.nature.com/articles/377606a0.

[16] K. Nakajima, D. Fisher, T. Kawakubo, H. Nakanishi, A. Ogata, Y. Kato, Y. Kitagawa, R. Kodama, K. Mima, H. Shiraga, K. Suzuki, K. Yamakawa, T. Zhang, Y. Sakawa, T. Shoji, Y. Nishida, N. Yugami, M. Downer, and T. Tajima. Observation of Ultrahigh Gradient Electron Acceleration by a Self-Modulated Intense Short Laser Pulse. *Physical Review Letters*, 74(22):4428–4431, may 1995. ISSN 0031-9007. doi: 10.1103/PhysRevLett.74.4428. URL https://link.aps.org/doi/10.1103/PhysRevLett.74.4428.

[17] R. Wagner, S.-Y. Chen, A. Maksimchuk, and D. Umstadter. Electron Acceleration by a Laser Wakefield in a Relativistically Self-Guided Channel. *Physical Review Letters*, 78(16):3125–3128, 1997. ISSN 0031-9007. doi: 10.1103/PhysRevLett.78.3125.

[18] D. Gordon, K. C. Tzeng, C. E. Clayton, A. E. Dangor, V. Malka, K. A. Marsh, A. Modena, W. B. Mori, P. Muggli, Z. Najmudin, D. Neely, C. Danson, and C. Joshi. Observation of Electron Energies Beyond the Linear Dephasing Limit from a Laser-Excited Relativistic Plasma Wave. *Physical Review Letters*, 80(10): 2133–2136, mar 1998. ISSN 0031-9007. doi: 10.1103/PhysRevLett.80.2133. URL https://link.aps.org/doi/10.1103/PhysRevLett.80.2133.

[19] S. P. D. Mangles, C. D. Murphy, Z. Najmudin, A. G. R. Thomas, J. L. Collier, A. E. Dangor, E. J. Divall, P. S. Foster, J. G. Gallacher, C. J. Hooker, D. A. Jaroszynski, A. J. Langley, W. B. Mori, P. A. Norreys, F. S. Tsung, R. Viskup, B. R. Walton, and K. Krushelnick. Monoenergetic beams of relativistic electrons from intense laser-plasma interactions. *Nature*, 431(7008):535–538, 2004. ISSN 0028-0836. doi: 10.1038/nature02939.

[20] J. Faure, Y. Glinec, A. Pukhov, S. Kiselev, S. Gordienko, E. Lefebvre, J.-P. Rousseau, F. Burgy, and V. Malka. A laser–plasma accelerator producing

monoenergetic electron beams. *Nature*, 431(September):541–544, 2004. doi: 10.1038/nature02900.1.

[21] C. G. R. Geddes, C. S. Tóth, J. Van Tilborg, E. Esarey, C. B. Schroeder, D. Bruhwiler, C. Nieter, J. Cary, and W. P. Leemans. High-quality electron beams from a laser wakefield accelerator using plasma-channel guiding. *Nature*, 431(7008): 538–541, 2004. ISSN 0028-0836. doi: 10.1038/nature02900.

[22] S. P. D. Mangles, A. G. R. Thomas, M. C. Kaluza, O. Lundh, F. Lindau, A. Persson, F. S. Tsung, Z. Najmudin, W. B. Mori, C. G. Wahlstrom, and K. Krushelnick. Laser-wakefield acceleration of monoenergetic electron beams in the first plasma-wave period. *Physical Review Letters*, 96:215001, 2006. ISSN 00319007. doi: 10.1103/PhysRevLett.96.215001.

[23] C. McGuffey, A. G. R. Thomas, W. Schumaker, T. Matsuoka, V. Chvykov, F. J. Dollar, G. Kalintchenko, V. Yanovsky, A. Maksimchuk, K. Krushelnick, V. Yu Bychenkov, I. V. Glazyrin, and A. V. Karpeev. Ionization Induced Trapping in a Laser Wakefield Accelerator. *Physical Review Letters*, 104(2):025004, jan 2010. ISSN 0031-9007. doi: 10.1103/PhysRevLett.104.025004. URL https://link.aps.org/doi/10.1103/PhysRevLett.104.025004.

[24] K. Schmid, A. Buck, C. M. S. Sears, J. M. Mikhailova, R. Tautz, D. Herrmann, M. Geissler, F. Krausz, and L. Veisz. Density-transition based electron injector for laser driven wakefield accelerators. *Physical Review Special Topics - Accelerators and Beams*, 13(9):1–5, 2010. ISSN 10984402. doi: 10.1103/PhysRevSTAB.13.091301.

[25] A. J. Gonsalves, K. Nakamura, C. Lin, D. Panasenko, S. Shiraishi, T. Sokollik, C. Benedetti, C. B. Schroeder, C. G. R. Geddes, J. van Tilborg, J. Osterhoff, E. Esarey, C. Toth, and W. P. Leemans. Tunable laser plasma accelerator based on longitudinal density tailoring. *Nature Physics*, 7(11):862–866, nov 2011. ISSN 1745-2473. doi: 10.1038/nphys2071. URL http://www.nature.com/articles/nphys2071.

[26] A. J. Gonsalves, K. Nakamura, J. Daniels, C. Benedetti, C. Pieronek, T. C. H. de Raadt, S. Steinke, J. H. Bin, S. S. Bulanov, J. van Tilborg, C. G. R. Geddes,

C. B. Schroeder, Cs. Tóth, E. Esarey, K. Swanson, L. Fan-Chiang, G. Bagdasarov, N. Bobrova, V. Gasilov, G. Korn, P. Sasorov, and W. P. Leemans. Petawatt Laser Guiding and Electron Beam Acceleration to 8 GeV in a Laser-Heated Capillary Discharge Waveguide. *Physical Review Letters*, 122(8):084801, feb 2019. ISSN 0031-9007. doi: 10.1103/PhysRevLett.122.084801. URL https://link.aps.org/doi/10.1103/PhysRevLett.122.084801.

[27] A. Radovic, M. Williams, D. Rousseau, M. Kagan, D. Bonacorsi, A. Himmel, A. Aurisano, K. Terao, and T. Wongjirad. Machine learning at the energy and intensity frontiers of particle physics. *Nature*, 560(7716):41–48, aug 2018. ISSN 0028-0836. doi: 10.1038/s41586-018-0361-2. URL http://www.nature.com/articles/s41586-018-0361-2.

[28] C. Emma, A. Edelen, M. J. Hogan, B. O'Shea, G. White, and V. Yakimenko. Machine learning-based longitudinal phase space prediction of particle accelerators. *Physical Review Accelerators and Beams*, 21(11):112802, nov 2018. ISSN 2469-9888. doi: 10.1103/PhysRevAccelBeams.21.112802. URL https://link.aps.org/doi/10.1103/PhysRevAccelBeams.21.112802.

[29] Z. H. He, B. Hou, V. Lebailly, J. A. Nees, K. Krushelnick, and A. G. R. Thomas. Coherent control of plasma dynamics. *Nature Communications*, 6(1):7156, nov 2015. ISSN 2041-1723. doi: 10.1038/ncomms8156. URL http://www.nature.com/articles/ncomms8156.

[30] S. J. D. Dann, C. D. Baird, N. Bourgeois, O. Chekhlov, S. Eardley, C. D. Gregory, J. N. Gruse, J. Hah, D. Hazra, S. J. Hawkes, C. J. Hooker, K. Krushelnick, S. P. D. Mangles, V. A. Marshall, C. D. Murphy, Z. Najmudin, J. A. Nees, J. Osterhoff, B. Parry, P. Pourmoussavi, S. V. Rahul, P. P. Rajeev, S. Rozario, J. D. E. Scott, R. A. Smith, E. Springate, Y. Tang, S. Tata, A. G. R. Thomas, C. Thornton, D. R. Symes, and M. J. V. Streeter. Laser wakefield acceleration with active feedback at 5 Hz. *Physical Review Accelerators and Beams*, 22(4): 041303, apr 2019. ISSN 2469-9888. doi: 10.1103/PhysRevAccelBeams.22.041303. URL https://link.aps.org/doi/10.1103/PhysRevAccelBeams.22.041303.

[31] R. J. Shalloo, S. J. D. Dann, J.-N. Gruse, C. I. D. Underwood, A. F. Antoine,

C. Arran, M. Backhouse, C. D. Baird, M. D. Balcazar, N. Bourgeois, J. A. Cardarelli, P. Hatfield, J. Kang, K. Krushelnick, S. P. D. Mangles, C. D. Murphy, N. Lu, J. Osterhoff, K. Põder, P. P. Rajeev, C. P. Ridgers, S. Rozario, M. P. Selwood, A. J. Shahani, D. R. Symes, A. G. R. Thomas, C. Thornton, Z. Najmudin, and M. J. V. Streeter. Automation and control of laser wakefield accelerators using Bayesian optimization. *Nature Communications*, 11 (1):6355, dec 2020. ISSN 2041-1723. doi: 10.1038/s41467-020-20245-6. URL http://www.nature.com/articles/s41467-020-20245-6.

[32] B. Hidding, S. Hooker, S. Jamison, B. Muratori, C. D. Murphy, Z. Najmudin, R. Pattathil, G. Sarri, M. J. V. Streeter, C. Welsch, M. Wing, and G. Xia. Plasma Wakefield Accelerator Research 2019 - 2040: A community-driven UK roadmap compiled by the Plasma Wakefield Accelerator Steering Committee (PWASC). *arXiv*, 2019. URL http://arxiv.org/abs/1904.09205.

[33] A. Di Piazza, C. Müller, K. Z. Hatsagortsyan, and C. H. Keitel. Extremely high-intensity laser interactions with fundamental quantum systems. *Reviews of Modern Physics*, 84(3):1177–1228, 2012. ISSN 00346861. doi: 10.1103/RevModPhys. 84.1177.

[34] L. D. Landau and E. M. Lifshitz. *The Classical Theory of Fields*. Elsevier, Oxford, 1975.

[35] T. C. Mo and C. H. Papas. New Equation of Motion for Classical Charged Particles. *Physical Review D*, 4(12):3566–3571, dec 1971. ISSN 0556-2821. doi: 10.1103/PhysRevD.4.3566. URL https://link.aps.org/doi/10.1103/PhysRevD.4.3566.

[36] I. V. Sokolov, N. M. Naumova, J. A. Nees, G. A. Mourou, and V. P. Yanovsky. Dynamics of emitting electrons in strong laser fields. *Physics of Plasmas*, 16, 2009. doi: 10.1063/1.3236748.

[37] G.W. Ford and R.F. O'Connell. Radiation reaction in electrodynamics and the elimination of runaway solutions. *Physics Letters A*, 157(4-5):217–220, jul 1991. ISSN 03759601. doi: 10.1016/0375-9601(91)90054-C. URL https://linkinghub.elsevier.com/retrieve/pii/037596019190054C.

[38] R. F. O'Connell. The equation of motion of an electron. *Physics Letters A*, 313(5-6):491–497, jul 2003. ISSN 03759601. doi: 10.1016/S0375-9601(03)00849-1. URL https://linkinghub.elsevier.com/retrieve/pii/S0375960103008491.

[39] F. Rohrlich. Dynamics of a charged particle. *Physical Review E*, 77(4):046609, apr 2008. ISSN 1539-3755. doi: 10.1103/PhysRevE.77.046609. URL https://link.aps.org/doi/10.1103/PhysRevE.77.046609.

[40] A. Ilderton and G. Torgrimsson. Radiation reaction in strong field QED. *Physics Letters B*, 725:481–486, 2013. ISSN 0370-2693. doi: 10.1016/j.physletb.2013.07.045. URL http://dx.doi.org/10.1016/j.physletb.2013.07.045.

[41] A. Di Piazza, M. Tamburini, S. Meuren, and C. H. Keitel. Implementing nonlinear Compton scattering beyond the local-constant-field approximation. *Physical Review A*, 98(1):012134, jul 2018. ISSN 2469-9926. doi: 10.1103/PhysRevA.98.012134. URL https://doi.org/10.1103/PhysRevA.98.012134https://link.aps.org/doi/10.1103/PhysRevA.98.012134.

[42] J. M. Cole, K. T. Behm, E. Gerstmayr, T. G. Blackburn, J. C. Wood, C. D. Baird, M. J. Duff, C. Harvey, A. Ilderton, A. S. Joglekar, K. Krushelnick, S. Kuschel, M. Marklund, P. McKenna, C. D. Murphy, K. Poder, C. P. Ridgers, G. M. Samarin, G. Sarri, D. R. Symes, A. G. R. Thomas, J. Warwick, M. Zepf, Z. Najmudin, and S. P. D. Mangles. Experimental evidence of radiation reaction in the collision of a high-intensity laser pulse with a laser-wakefield accelerated electron beam. *Physical Review X*, 8:011020, 2018. ISSN 2160-3308. doi: 10.1103/PhysRevX.8.011020. URL http://arxiv.org/abs/1707.06821.

[43] K. Poder, M. Tamburini, G. Sarri, A. Di Piazza, S. Kuschel, C.D. Baird, K. Behm, S. Bohlen, J.M. Cole, D.J. Corvan, M. Duff, E. Gerstmayr, C.H. Keitel, K. Krushelnick, S.P.D. Mangles, P. McKenna, C.D. Murphy, Z. Najmudin, C.P. Ridgers, G.M. Samarin, D.R. Symes, A.G.R. Thomas, J. Warwick, and M. Zepf. Experimental Signatures of the Quantum Nature of Radiation Reaction in the Field of an Ultraintense Laser. *Physical Review X*, 8(3):031004, jul 2018. ISSN 2160-3308. doi: 10.1103/PhysRevX.8.031004. URL https://link.aps.org/doi/10.1103/PhysRevX.8.031004.

[44] T. N. Wistisen, A. Di Piazza, H. V. Knudsen, and U. I. Uggerhøj. Experimental evidence of quantum radiation reaction in aligned crystals. *Nature Communications*, 9(1):2–7, 2018. ISSN 20411723. doi: 10.1038/s41467-018-03165-4. URL http://dx.doi.org/10.1038/s41467-018-03165-4.

[45] S. Kneip, S. R. Nagel, C. Bellei, N. Bourgeois, A. E. Dangor, A. Gopal, R. Heathcote, S. P. D. Mangles, J. R. Marquès, A. Maksimchuk, P. M. Nilson, K. Ta Phuoc, S. Reed, M. Tzoufras, F. S. Tsung, L. Willingale, W. B. Mori, A. Rousse, K. Krushelnick, and Z. Najmudin. Observation of Synchrotron Radiation from Electrons Accelerated in a Petawatt-Laser-Generated Plasma Cavity. *Physical Review Letters*, 100(10):105006, mar 2008. ISSN 0031-9007. doi: 10.1103/PhysRevLett.100.105006. URL https://link.aps.org/doi/10.1103/PhysRevLett.100.105006https://journals.aps.org/prl/abstract/10.1103/PhysRevLett.100.105006.

[46] J. M. Cole, D. R. Symes, N. C. Lopes, J. C. Wood, K. Poder, S. Alatabi, S. W. Botchway, P. S. Foster, S. Gratton, S. Johnson, C. Kamperidis, O. Kononenko, M. De Lazzari, C. A. J. Palmer, D. Rusby, J. Sanderson, M. Sandholzer, G. Sarri, Z. Szoke-Kovacs, L. Teboul, J. M. Thompson, J. R. Warwick, H. Westerberg, M. A. Hill, D. P. Norris, S. P. D. Mangles, and Z. Najmudin. High-resolution μCT of a mouse embryo using a compact laser-driven X-ray betatron source. *Proceedings of the National Academy of Sciences of the United States of America*, 115(25):6335–6340, 2018. ISSN 10916490. doi: 10.1073/pnas.1802314115.

[47] J. N. Gruse, M. J. V. Streeter, C. Thornton, C. D. Armstrong, C. D. Baird, N. Bourgeois, S. Cipiccia, O. J. Finlay, C. D. Gregory, Y. Katzir, N. C. Lopes, S. P. D. Mangles, Z. Najmudin, D. Neely, L. R. Pickard, K. D. Potter, P. P. Rajeev, D. R. Rusby, C. I. D. Underwood, J. M. Warnett, M. A. Williams, J. C. Wood, C. D. Murphy, C. M. Brenner, and D. R. Symes. Application of compact laser-driven accelerator X-ray sources for industrial imaging. *Nuclear Instruments and Methods in Physics Research Section A: Accelerators, Spectrometers, Detectors and Associated Equipment*, page 164369, jul 2020. ISSN 01689002. doi: 10.1016/j.nima.2020.164369. URL https://

www.sciencedirect.com/science/article/pii/S016890022030766Xhttps:
//linkinghub.elsevier.com/retrieve/pii/S016890022030766X.

[48] S. Kneip, C. McGuffey, F. Dollar, M. S. Bloom, V. Chvykov, G. Kalintchenko, K. Krushelnick, A. Maksimchuk, S. P. D. Mangles, T. Matsuoka, Z. Najmudin, C. A. J. Palmer, J. Schreiber, W. Schumaker, A. G. R. Thomas, and V. Yanovsky. X-ray phase contrast imaging of biological specimens with femtosecond pulses of betatron radiation from a compact laser plasma wakefield accelerator. *Applied Physics Letters*, 99(9):1–4, 2011. ISSN 00036951. doi: 10.1063/1.3627216.

[49] S. Fourmaux, S. Corde, K. Ta Phuoc, P. Lassonde, G. Lebrun, S. Payeur, F. Martin, S. Sebban, V. Malka, A. Rousse, and J. C. Kieffer. Single shot phase contrast imaging using laser-produced Betatron x-ray beams. *Optics letters*, 36(13): 2426–8, 2011. ISSN 1539-4794. doi: 10.1364/OL.36.002426. URL http://www. osapublishing.org/viewmedia.cfm?uri=ol-36-13-2426&seq=0&html=true.

[50] J. Wenz, S. Schleede, K. Khrennikov, M. Bech, P. Thibault, M. Heigoldt, F. Pfeiffer, and S. Karsch. Quantitative X-ray phase-contrast microtomography from a compact laser-driven betatron source. *Nature Communications*, 6 (May):1–6, 2015. ISSN 20411723. doi: 10.1038/ncomms8568. URL http: //dx.doi.org/10.1038/ncomms8568.

[51] R. D. Edwards, M. A. Sinclair, T. J. Goldsack, K. Krushelnick, F. N. Beg, E. L. Clark, A. E. Dangor, Z. Najmudin, M. Tatarakis, B. Walton, M. Zepf, K. W. D. Ledingham, I. Spencer, P. A. Norreys, R. J. Clarke, R. Kodama, Y. Toyama, and M. Tampo. Characterization of a gamma-ray source based on a laser-plasma accelerator with applications to radiography. *Applied Physics Letters*, 80(12): 2129–2131, 2002. ISSN 0003-6951. doi: 10.1063/1.1464221.

[52] Y. Glinec, J. Faure, L. Le Dain, S. Darbon, T. Hosokai, J. J. Santos, E. Lefebvre, J.-P. Rousseau, F. Burgy, B. Mercier, and V. Malka. High-Resolution γ-Ray Radiography Produced by a Laser-Plasma Driven Electron Source. *Phys. Rev. Lett.*, 94:025003, 2005. doi: 10.1103/PhysRevLett.94.025003.

[53] A. Döpp, E. Guillaume, C. Thaury, A. Lifschitz, F. Sylla, J.-P. Goddet, A. Tafzi, G. Iaquanello, T. Lefrou, P. Rousseau, E. Conejero, C. Ruiz, K. Ta Phuoc,

and V. Malka. A bremsstrahlung gamma-ray source based on stable ionization injection of electrons into a laser wakefield accelerator. *Nuclear Inst. and Methods in Physics Research, A*, 830:515–519, 2016. ISSN 0168-9002. doi: 10.1016/j.nima. 2016.01.086. URL http://dx.doi.org/10.1016/j.nima.2016.01.086.

[54] K. Dong, T. Zhang, M. Yu, Y. Wu, B. Zhu, F. Tan, S. Wang, Y. Yan, J. Yang, Y. Yang, F. Lu, G. Li, W. Fan, W. Hong, Z. Zhao, W. Zhou, L. Cao, and Y. Gu. Micro-spot gamma-ray generation based on laser wakefield acceleration. *Journal of Applied Physics*, 123(July 2017):243301, 2018. doi: 10.1063/1.4997142.

[55] K. Ta Phuoc, S. Corde, C. Thaury, V. Malka, A. Tafzi, J. P. Goddet, R. C. Shah, S. Sebban, and A. Rousse. All-optical Compton gamma-ray source. *Nature Photonics*, 6(April):1–4, 2012. doi: 10.1038/NPHOTON.2012.82.

[56] S. Chen, N. D. Powers, I. Ghebregziabher, C. M. Maharjan, C. Liu, G. Golovin, S. Banerjee, J. Zhang, N. Cunningham, A. Moorti, S. Clarke, S. Pozzi, and D. P. Umstadter. MeV-Energy X Rays from Inverse Compton Scattering with Laser-Wakefield Accelerated Electrons. *Physical Review Letters*, 110(15):155003, 2013. doi: 10.1103/PhysRevLett.110.155003.

[57] N. D. Powers, I. Ghebregziabher, G. Golovin, C. Liu, S. Chen, S. Banerjee, J. Zhang, and D. P. Umstadter. Quasi-monoenergetic and tunable X-rays from a laser-driven Compton light source. *Nature Photonics*, 8(1):28–31, 2013. ISSN 1749-4885. doi: 10.1038/nphoton.2013.314. URL http://dx.doi.org/10.1038/nphoton.2013.314.

[58] C. P. Ridgers, C. S. Brady, R. Duclous, J. G. Kirk, K. Bennett, T. D. Arber, and A. R. Bell. Dense electron-positron plasmas and bursts of gamma-rays from laser-generated quantum electrodynamic plasmas. *Physics of Plasmas*, 20(5): 056701, may 2013. ISSN 1070-664X. doi: 10.1063/1.4801513. URL http://aip.scitation.org/doi/10.1063/1.4801513.

[59] D. R. Rusby, C. D. Armstrong, C. M. Brenner, R. J. Clarke, P. McKenna, and D. Neely. Novel scintillator-based x-ray spectrometer for use on high repetition laser plasma interaction experiments. *Review of Scientific Instruments*, 89(7),

2018. ISSN 10897623. doi: 10.1063/1.5019213. URL http://dx.doi.org/10.1063/1.5019213.

[60] K. T. Behm, J. M. Cole, A. S. Joglekar, E. Gerstmayr, J. C. Wood, C. D. Baird, T. G. Blackburn, M. Duff, C. Harvey, A. Ilderton, S. Kuschel, S. P. D. Mangles, M. Marklund, P. McKenna, C. D. Murphy, Z. Najmudin, K. Poder, C. P. Ridgers, G. Sarri, G. M. Samarin, D. Symes, J. Warwick, M. Zepf, K. Krushelnick, and A. G. R. Thomas. A spectrometer for ultrashort gamma-ray pulses with photon energies greater than 10 MeV. *Review of Scientific Instruments*, 89(11):113303, nov 2018. ISSN 0034-6748. doi: 10.1063/1.5056248. URL http://aip.scitation.org/doi/10.1063/1.5056248.

[61] C. I. D. Underwood, C. D. Baird, C. D. Murphy, C. D. Armstrong, C. Thornton, O. J. Finlay, M. J. V. Streeter, M. P. Selwood, N. Brierley, S. Cipiccia, J. N. Gruse, P. McKenna, Z. Najmudin, D. Neely, D. Rusby, D. R. Symes, and C. M. Brenner. Development of control mechanisms for a laser wakefield accelerator-driven bremsstrahlung x-ray source for advanced radiographic imaging. *Plasma Physics and Controlled Fusion*, 62(12), 2020. ISSN 13616587. doi: 10.1088/1361-6587/abbebe.

[62] G. A. Mourou, C. L. Labaune, M. Dunne, N. Naumova, and V. T. Tikhonchuk. Relativistic laser-matter interaction: From attosecond pulse generation to fast ignition. *Plasma Physics and Controlled Fusion*, 49(12 B), 2007. ISSN 07413335. doi: 10.1088/0741-3335/49/12B/S61.

[63] M. C. Asplund, J. A. Johnson, and J. E. Patterson. The 2018 Nobel Prize in Physics: optical tweezers and chirped pulse amplification. *Analytical and Bioanalytical Chemistry*, 411(20):5001–5005, aug 2019. ISSN 16182650. doi: 10.1007/s00216-019-01913-z. URL http://link.springer.com/10.1007/s00216-019-01913-z.

[64] L. D. Landau and E. M. Lifshitz. *Mechanics*. Pergamon Press, 2 edition, 1969. ISBN 978-0-201-04146-0.

[65] P. Gibbon. Short Pulse Laser Interactions with Matter, 2005.

[66] C. J. McKinstrie and D. F. DuBois. A covariant formalism for wave propagation applied to stimulated Raman scattering. *Physics of Fluids*, 31:278, 1988. ISSN 00319171. doi: 10.1063/1.866858.

[67] A. J. W. Reitsma. *Electron bunch quality in laser wakefield acceleration*. PhD thesis, 2002.

[68] J. M. Dawson. Nonlinear Electron Oscillations in a Cold Plasma. *Phys. Rev. Lett.*, 113(2):383–387, 1959.

[69] T. Katsouleas and W. B. Mori. Wave-Breaking Amplitude of Relativistic Oscillations in a Thermal Plasma. *Phys. Rev. Lett.*, 61(1):90–93, 1988. ISSN 1528-1159. doi: 10.1097/BRS.0000000000000032.

[70] P. Sprangle, E. Esarey, and A. Ting. Nonlinear Interaction of Intense Laser Pulses in Plasmas. *Physical Review A*, 41(8), 1990.

[71] C. E. Max, J. Aronst, and A. B. Langdon. Self-Modulation and Self-Focusing of Electromagnetic Waves in Plasma. *Phys. Rev. Lett.*, 33(4):209–212, 1974.

[72] E. Esarey, C. B. Schroeder, and W. P. Leemans. Physics of laser-driven plasma-based electron accelerators. *Reviews of Modern Physics*, 81(3):1229–1285, 2009. ISSN 00346861. doi: 10.1103/RevModPhys.81.1229.

[73] M. Chen, Z.-M. Sheng, Y.-Y. Ma, and J. Zhang. Electron injection and trapping in a laser wakefield by field ionization to high-charge states of gases. *Journal of Applied Physics*, 99(5):056109, mar 2006. ISSN 0021-8979. doi: 10.1063/1.2179194. URL http://aip.scitation.org/doi/10.1063/1.2179194.

[74] C. E. Clayton, J. E. Ralph, F. Albert, R. A. Fonseca, S. H. Glenzer, C. Joshi, W. Lu, K. A. Marsh, S. F. Martins, W. B. Mori, A. Pak, F. S. Tsung, B. B. Pollock, J. S. Ross, L. O. Silva, and D. H. Froula. Self-guided laser wakefield acceleration beyond 1 GeV using ionization-induced injection. *Physical Review Letters*, 105(10):105003, 2010. ISSN 00319007. doi: 10.1103/PhysRevLett.105.105003.

[75] A. Pak, K. A. Marsh, S. F. Martins, W. Lu, W. B. Mori, and C. Joshi. Injection and Trapping of Tunnel-Ionized Electrons into Laser-Produced Wakes.

Physical Review Letters, 104(2):025003, jan 2010. ISSN 0031-9007. doi: 10.1103/PhysRevLett.104.025003. URL https://link.aps.org/doi/10.1103/PhysRevLett.104.025003.

[76] A. Buck, J. Wenz, J. Xu, K. Khrennikov, K. Schmid, M. Heigoldt, J. M. Mikhailova, M. Geissler, B. Shen, F. Krausz, S. Karsch, and L. Veisz. Shock-front injector for high-quality laser-plasma acceleration. *Physical Review Letters*, 110 (18):1–5, 2013. ISSN 00319007. doi: 10.1103/PhysRevLett.110.185006.

[77] J. A. Cardarelli, M. J. V. Streeter, C. Colgan, D. Hollatz, A. Alejo, C. Arran, C. D. Baird, M. D. Balcazar, E. Gerstmayr, H. Harsh, B. Kettle, E. Los, C. Roedel, F. Salgodo, G. M. Samarin, G. Sarri, A. G. R. Thomas, C. I. D. Underwood, M. Zepf, and S. P. D. Mangles. Shock injection producing narrow energy spread, GeV electron beams from a laser wakefield accelerator. In *APS Division of Plasma Physics Meeting Abstracts*, 2019.

[78] B. Hidding, G. Pretzler, J. B. Rosenzweig, T. Königstein, D. Schiller, and D. L. Bruhwiler. Ultracold Electron Bunch Generation via Plasma Photocathode Emission and Acceleration in a Beam-Driven Plasma Blowout. *Physical Review Letters*, 108(3):035001, jan 2012. ISSN 0031-9007. doi: 10.1103/PhysRevLett.108.035001. URL https://link.aps.org/doi/10.1103/PhysRevLett.108.035001.

[79] E. Esarey, B. A. Shadwick, C. B. Schroeder, and W. P. Leemans. Nonlinear Pump Depletion and Electron Dephasing in Laser Wakefield Accelerators. In *AIP Conference Proceedings*, pages 578–584, 2004. ISBN 0735402205. doi: 10.1063/1.1842594.

[80] J. D. Jackson. *Classical Electrodynamics*. Wiley, 1999.

[81] G. B. Rybicki and A. P. Lightman. *Radiative Processes in Astrophysics*. Wiley-VCH, 1986. ISBN ISBN 0-471-82759-2.

[82] V. B. Berestetskii, E. M. Lifshitz, and L. P. Pitaevskii. *Quantum Electrodynamics*. Butterworth-Heinemann, 1982.

[83] D. D. Meyerhofer. High-intensity-laser-electron scattering. *IEEE Journal of Quantum Electronics*, 33(11):1935–1941, 1997. ISSN 00189197. doi: 10.1109/3.641308. URL http://ieeexplore.ieee.org/document/641308/.

[84] F. V. Hartemann, A. L. Troha, N. C. Luhmann, and Z. Toffano. Spectral analysis of the nonlinear relativistic Doppler shift in ultrahigh intensity Compton scattering. *Physical Review E*, 54(3):2956–2962, sep 1996. ISSN 1063-651X. doi: 10.1103/PhysRevE.54.2956. URL https://link.aps.org/doi/10.1103/PhysRevE.54.2956.

[85] F. Mackenroth and A. Di Piazza. Nonlinear Compton scattering in ultrashort laser pulses. *Physical Review A*, 83(3):032106, mar 2011. ISSN 1050-2947. doi: 10.1103/PhysRevA.83.032106. URL https://link.aps.org/doi/10.1103/PhysRevA.83.032106.

[86] A. H. Compton. A Quantum Theory of the Scattering of X-rays by Light Elements. *Physical Review*, 21(5):483–502, 1923. ISSN 0031899X. doi: 10.1103/PhysRev.21.483.

[87] O. Klein and Y. Nishina. The scattering of light by free electrons according to Dirac's new relativistic dynamics. *Nature*, 122(3072):398, 1928.

[88] W. Heitler. *The Quantum Theory of Radiation*. Oxford University Press, 1954.

[89] J. Schwinger. On the Classical Radiation of Accelerated Electrons. *Physical Review*, 75(12):1912–1925, 1949. doi: 10.1103/PhysRev.75.1912.

[90] P. A. M. Dirac. Classical theory of radiating electrons. *Proceedings of the Royal Society of London. Series A. Mathematical and Physical Sciences*, 167(929):148–169, aug 1938. ISSN 2053-9169. doi: 10.1098/rspa.1938.0124. URL http://www.royalsocietypublishing.org/doi/10.1098/rspa.1938.0124.

[91] R. T. Hammond. Relativistic particle motion and radiation reaction in electrodynamics. *Electronic Journal of Theoretical Physics*, 7(23):221–258, 2010. ISSN 17295254.

[92] A. G. R. Thomas, C. P. Ridgers, S. S. Bulanov, B. J. Griffin, and S. P. D. Mangles. Strong Radiation-Damping Effects in a Gamma-Ray Source Generated by

the Interaction of a High-Intensity Laser with a Wakefield-Accelerated Electron Beam. *Physical Review X*, 2:041004, 2012. doi: 10.1103/PhysRevX.2.041004.

[93] J. G. Kirk, A. R. Bell, and I. Arka. Pair production in counter-propagating laser beams. *Plasma Physics and Controlled Fusion*, 51(8): 085008, aug 2009. ISSN 0741-3335. doi: 10.1088/0741-3335/51/8/085008. URL http://stacks.iop.org/0741-3335/51/i=8/a=085008?key=crossref.6461053203b8669f6568cb804921a22e.

[94] J. Schwinger. On Gauge Invariance and Vacuum Polarization. *Physical Review*, 82(5):664–679, 1951. ISSN 0031899X. doi: 10.1103/PhysRev.82.664.

[95] V. I. Ritus. Quantum Effects of the Interaction of Elementary Particles with an Intense Electromagnetic Field. *Journal of Soviet Laser Research*, 6(5):497–617, 1985. ISSN 02702010. doi: 10.1007/BF01120220.

[96] A. R. Bell and John G. Kirk. Possibility of prolific pair production with high-power lasers. *Physical Review Letters*, 101(20):200403, 2008. ISSN 00319007. doi: 10.1103/PhysRevLett.101.200403.

[97] T. Erber. High-energy electromagnetic conversion processes in intense magnetic fields. *Reviews of Modern Physics*, 38(4):626–659, 1966. ISSN 00346861. doi: 10.1103/RevModPhys.38.626.

[98] C. S. Shen and D. White. Energy straggling and radiation reaction for magnetic bremsstrahlung. *Physical Review Letters*, 28(7):455–459, 1972. ISSN 0031-9007. doi: 10.1103/PhysRevLett.28.455.

[99] S. V. Bulanov, T. Zh Esirkepov, J. Koga, and T. Tajima. Interaction of electro-magnetic waves with plasma in the radiation-dominated regime. *Plasma Physics Reports*, 30(3):196–213, mar 2004. ISSN 1063-780X. doi: 10.1134/1.1687021. URL http://link.springer.com/10.1134/1.1687021.

[100] J. Koga, T. Zh. Esirkepov, and S. V. Bulanov. Nonlinear Thomson scattering in the strong radiation damping regime. *Physics of Plasmas*, 12(9):093106, sep 2005. ISSN 1070-664X. doi: 10.1063/1.2013067. URL http://aip.scitation.org/doi/10.1063/1.2013067.

[101] S. J. Hawkes. *Private Communication.*

[102] C. J. Hooker, S. Blake, O. Chekhlov, R. J. Clarke, J. L. Collier, E. J. Divall, K. Ertel, P. S. Foster, S. J. Hawkes, P. Holligan, B. Landowski, W. J. Lester, D. Neely, B. Parry, R. Pattathil, M. Streeter, and B. E. Wyborn. Commissioning the Astra Gemini petawatt Ti:sapphire laser system. *2008 Conference on Quantum Electronics and Laser Science Conference on Lasers and Electro-Optics, CLEO/QELS*, pages 2–3, 2008. doi: 10.1109/CLEO.2008.4552106.

[103] P. Tournois. Acousto-optic programmable dispersive filter for adaptive compensation of group delay time dispersion in laser systems. *Optics Communications*, 140(4-6):245–249, aug 1997. ISSN 00304018. doi: 10.1016/S0030-4018(97)00153-3. URL https://linkinghub.elsevier.com/retrieve/pii/S0030401897001533.

[104] F. Salin, P. Georges, G. Roger, and A. Brun. Single-shot measurement of a 52-fs pulse. *Applied Optics*, 26(21):4528, 1987. ISSN 0003-6935. doi: 10.1364/ao.26.004528.

[105] R. Trebino. *Frequency-Resolved Optical Gating: The Measurement of Ultrashort Laser Pulses.* Springer US, Boston, MA, 2000. ISBN 978-1-4613-5432-1. doi: 10.1007/978-1-4615-1181-6. URL http://link.springer.com/10.1007/978-1-4615-1181-6.

[106] M. J. V. Streeter. *Ultrafast Dynamics of Relativistic Laser Plasma Interactions.* PhD thesis, Imperial College London, 2013.

[107] A. Buck, K. Zeil, A. Popp, K. Schmid, A. Jochmann, S. D. Kraft, B. Hidding, T. Kudyakov, C. M. S. Sears, L. Veisz, S. Karsch, J. Pawelke, R. Sauerbrey, T. Cowan, F. Krausz, and U. Schramm. Absolute charge calibration of scintillating screens for relativistic electron detection. *Review of Scientific Instruments*, 81(3):033301, mar 2010. ISSN 0034-6748. doi: 10.1063/1.3310275. URL http://aip.scitation.org/doi/10.1063/1.3310275.

[108] Y. Glinec, J. Faure, A. Guemnie-Tafo, V. Malka, H. Monard, J. P. Larbre, V. De Waele, J. L. Marignier, and M. Mostafavi. Absolute calibration for a broad

range single shot electron spectrometer. *Review of Scientific Instruments*, 77 (10):103301, oct 2006. ISSN 0034-6748. doi: 10.1063/1.2360988. URL http://aip.scitation.org/doi/10.1063/1.2360988.

[109] S. Masuda, E. Miura, K. Koyama, and S. Kato. Absolute calibration of an electron spectrometer using high energy electrons produced by the laser-plasma interaction. *Review of Scientific Instruments*, 79(8), 2008. ISSN 00346748. doi: 10.1063/1.2969655.

[110] B. Hidding, G. Pretzler, M. Clever, F. Brandl, F. Zamponi, A. Lübcke, T. Kämpfer, I. Uschmann, E. Förster, U. Schramm, R. Sauerbrey, E. Kroupp, L. Veisz, K. Schmid, S. Benavides, and S. Karsch. Novel method for characterizing relativistic electron beams in a harsh laser-plasma environment. *Review of Scientific Instruments*, 78(8), 2007. ISSN 00346748. doi: 10.1063/1.2775668.

[111] K. A. Tanaka, T. Yabuuchi, T. Sato, R. Kodama, Y. Kitagawa, T. Takahashi, T. Ikeda, Y. Honda, and S. Okuda. Calibration of imaging plate for high energy electron spectrometer. *Review of Scientific Instruments*, 76(1):013507, 2005. ISSN 0034-6748. doi: 10.1063/1.1824371.

[112] J. M. Cole. *Diagnosis and Application of Laser Wakefield Accelerators*. PhD thesis, Imperial College London, 2016.

[113] I. H. Hutchinson. *Principles of Plasma Diagnostics*. Cambridge University Press, 2002.

[114] M. Sonoda, M. Takano, J. Miyahara, and H. Kato. Computed radiography utilizing scanning laser stimulated luminescence. *Radiology*, 148(3):833–838, sep 1983. ISSN 0033-8419. doi: 10.1148/radiology.148.3.6878707. URL http://pubs.rsna.org/doi/10.1148/radiology.148.3.6878707.

[115] S. G. Gales and C. D. Bentley. Image plates as x-ray detectors in plasma physics experiments. *Review of Scientific Instruments*, 75(10):4001–4003, oct 2004. ISSN 0034-6748. doi: 10.1063/1.1789256. URL http://aip.scitation.org/doi/10.1063/1.1789256.

[116] A. L. Meadowcroft, C. D. Bentley, and E. N. Stott. Evaluation of the sensitivity and fading characteristics of an image plate system for x-ray diagnostics. *Review of Scientific Instruments*, 79(11):113102, nov 2008. ISSN 0034-6748. doi: 10.1063/1.3013123. URL http://aip.scitation.org/doi/10.1063/1.3013123.

[117] V. Nagirnyi, S. Zazubovich, V. Zepelin, M. Nikl, and G.P. Pazzi. A new model for the visible emission of the CsI: Tl crystal. *Chemical Physics Letters*, 227(4-5): 533–538, sep 1994. ISSN 00092614. doi: 10.1016/0009-2614(94)00857-4. URL https://linkinghub.elsevier.com/retrieve/pii/0009261494008574.

[118] M. J. Berger, J. H. Hubbell, S. M. Seltzer, J. Chang, J. S. Coursey, R. Sukumar, and D. S. Zucker. XCOM: photon cross sections database. Technical report, 1998. URL https://www.nist.gov/pml/xcom-photon-cross-sections-database.

[119] S. Agostinelli, J. Allison, K. Amako, J. Apostolakis, H. Araujo, P. Arce, M. Asai, D. Axen, S. Banerjee, G. Barrand, F. Behner, L. Bellagamba, J. Boudreau, L. Broglia, A. Brunengo, H. Burkhardt, S. Chauvie, J. Chuma, R. Chytracek, G. Cooperman, G. Cosmo, P. Degtyarenko, A. Dell'Acqua, G. Depaola, D. Dietrich, R. Enami, A. Feliciello, C. Ferguson, H. Fesefeldt, G. Folger, F. Foppiano, A. Forti, S. Garelli, S. Giani, R. Giannitrapani, D. Gibin, J.J. Gómez Cadenas, I. González, G. Gracia Abril, G. Greeniaus, W. Greiner, V. Grichine, A. Grossheim, S. Guatelli, P. Gumplinger, R. Hamatsu, K. Hashimoto, H. Hasui, A. Heikkinen, A. Howard, V. Ivanchenko, A. Johnson, F.W. Jones, J. Kallenbach, N. Kanaya, M. Kawabata, Y. Kawabata, M. Kawaguti, S. Kelner, P. Kent, A. Kimura, T. Kodama, R. Kokoulin, M. Kossov, H. Kurashige, E. Lamanna, T. Lampén, V. Lara, V. Lefebure, F. Lei, M. Liendl, W. Lockman, F. Longo, S. Magni, M. Maire, E. Medernach, K. Minamimoto, P. Mora de Freitas, Y. Morita, K. Murakami, M. Nagamatu, R. Nartallo, P. Nieminen, T. Nishimura, K. Ohtsubo, M. Okamura, S. O'Neale, Y. Oohata, K. Paech, J. Perl, A. Pfeiffer, M.G. Pia, F. Ranjard, A. Rybin, S. Sadilov, E. Di Salvo, G. Santin, T. Sasaki, N. Savvas, Y. Sawada, S. Scherer, S. Sei, V. Sirotenko, D. Smith, N. Starkov, H. Stoecker, J. Sulkimo, M. Takahata, S. Tanaka, E. Tcherniaev, E. Safai Tehrani, M. Tropeano, P. Truscott, H. Uno, L. Urban, P. Urban, M. Verderi, A. Walkden, W. Wander, H. Weber, J.P. Wellisch, T. Wenaus, D.C.

Williams, D. Wright, T. Yamada, H. Yoshida, and D. Zschiesche. Geant4—a simulation toolkit. *Nuclear Instruments and Methods in Physics Research Section A: Accelerators, Spectrometers, Detectors and Associated Equipment*, 506(3): 250–303, jul 2003. ISSN 01689002. doi: 10.1016/S0168-9002(03)01368-8. URL https://linkinghub.elsevier.com/retrieve/pii/S0168900203013688.

[120] T. D. Arber, K. Bennett, C. S. Brady, A. Lawrence-Douglas, M. G. Ramsay, N. J. Sircombe, P. Gillies, R. G. Evans, H. Schmitz, A. R. Bell, and C. P. Ridgers. Contemporary particle-in-cell approach to laser-plasma modelling. *Plasma Physics and Controlled Fusion*, 57(11):113001, 2015. ISSN 0741-3335. doi: 10.1088/0741-3335/57/11/113001. URL http://stacks.iop.org/0741-3335/57/i=11/a=113001?key=crossref.907aa156b73b99b125b1a0ae886c4c22.

[121] J. P. Boris and R. A. Shanny. Relativistic Plasma Simulation-Optimization of a Hybrid Code. In *Fourth Conference on Numerical Simulation of Plasmas, November 2, 3, 1970*, 1970.

[122] K. S. Yee. Numerical solution of initial boundary value problems involving maxwell's equations in isotropic media. *IEEE Transactions on Antennas and Propagation*, 14(3):302–307, 1966. ISSN 0018-926X. doi: 10.1109/tap.1966.1138693.

[123] R. Courant, K. Friedrichs, and H. Lewy. Über die partiellen Differenzengleichungen der mathematischen Physik. *Mathematische Annalen*, 100(1):32–74, dec 1928. ISSN 0025-5831. doi: 10.1007/BF01448839. URL http://link.springer.com/10.1007/BF01448839.

[124] A. Taflove. Review of the formulation and applications of the finite-difference time-domain method for numerical modeling of electromagnetic wave interactions with arbitrary structures. *Wave Motion*, 10(6):547–582, dec 1988. ISSN 01652125. doi: 10.1016/0165-2125(88)90012-1. URL https://linkinghub.elsevier.com/retrieve/pii/0165212588900121.

[125] EPOCH User Manual. URL https://cfsa-pmw.warwick.ac.uk/mediawiki/index.php/EPOCH:Landing_Page.

[126] T. G. Blackburn. Measuring quantum radiation reaction in laser – electron-beam collisions. *Plasma Physics and Controlled Fusion*, 57:075012, 2015. doi: 10.1088/0741-3335/57/7/075012.

[127] R. Duclous, J. G. Kirk, and A. R. Bell. Monte Carlo calculations of pair production in high-intensity laser–plasma interactions. *Plasma Physics and Controlled Fusion*, 53(1):015009, 2011. ISSN 0741-3335. doi: 10.1088/0741-3335/53/1/015009. URL http://stacks.iop.org/0741-3335/53/i=1/a=015009?key=crossref.a8a8821fd000c941572db8818a245120.

[128] C. P. Ridgers, J. G. Kirk, R. Duclous, T. G. Blackburn, C. S. Brady, K. Bennett, T. D. Arber, and A. R. Bell. Modelling gamma-ray photon emission and pair production in high-intensity laser – matter interactions. *Journal of Computational Physics*, 260:273–285, 2014. ISSN 0021-9991. doi: 10.1016/j.jcp.2013.12.007. URL http://dx.doi.org/10.1016/j.jcp.2013.12.007.

[129] S. Gales, D. L. Balabanski, F. Negoita, O. Tesileanu, C. A. Ur, D. Ursescu, and N. V. Zamfir. New frontiers in nuclear physics with high-power lasers and brilliant monochromatic gamma beams. *Physica Scripta*, 91 (9):093004, 2016. ISSN 0031-8949. doi: 10.1088/0031-8949/91/9/093004. URL http://stacks.iop.org/1402-4896/91/i=9/a=093004?key=crossref.26bed6a03d238438a137078ac19e7d6e.

[130] K. A. Tanaka, K. M. Spohr, D. L. Balabanski, S. Balascuta, L. Capponi, M. O. Cernaianu, M. Cuciuc, A. Cucoanes, I. Dancus, A. Dhal, B. Diaconescu, D. Doria, P. Ghenuche, D. G. Ghita, S. Kisyov, V. Nastasa, J. F. Ong, F. Rotaru, D. Sangwan, P.-A. Söderström, D. Stutman, G. Suliman, O. Tesileanu, L. Tudor, N. Tsoneva, C. A. Ur, D. Ursescu, and N. V. Zamfir. Current status and highlights of the ELI-NP research program. *Matter and Radiation at Extremes*, 5(2):024402, mar 2020. ISSN 2468-2047. doi: 10.1063/1.5093535. URL http://aip.scitation.org/doi/10.1063/1.5093535.

[131] G. Chériaux, F. Giambruno, A. Fréneaux, F. Leconte, L. P. Ramirez, P. Georges, F. Druon, D. N. Papadopoulos, A. Pellegrina, C. Le Blanc, I. Doyen, L. Legat, J. M. Boudenne, G. Mennerat, P. Audebert, G. Mourou, F. Mathieu, and J. P.

Chambaret. Apollon-10P: Status and implementation. *AIP Conference Proceedings*, 1462:78–83, 2012. ISSN 0094243X. doi: 10.1063/1.4736764.

[132] J. P. Zou, C. Le Blanc, D. N. Papadopoulos, G. Chériaux, P. Georges, G. Mennerat, F. Druon, L. Lecherbourg, A. Pellegrina, P. Ramirez, F. Giambruno, A. Fréneaux, F. Leconte, D. Badarau, J. M. Boudenne, D. Fournet, T. Valloton, J. L. Paillard, J. L. Veray, M. Pina, P. Monot, J. P. Chambaret, P. Martin, F. Mathieu, P. Audebert, and F. Amiranoff. Design and current progress of the Apollon 10 PW project. *High Power Laser Science and Engineering*, 3:15–18, 2015. ISSN 20523289. doi: 10.1017/hpl.2014.41.

[133] C. P. Ridgers, C. S. Brady, R. Duclous, J. G. Kirk, K. Bennett, T. D. Arber, A. P. L. Robinson, and A. R. Bell. Dense Electron-Positron Plasmas and Ultraintense ¡math display="inline"¿ ¡mi¿γ¡/mi¿ ¡/math¿ rays from Laser-Irradiated Solids. *Physical Review Letters*, 108(16):165006, apr 2012. ISSN 0031-9007. doi: 10.1103/PhysRevLett.108.165006. URL https://link.aps.org/doi/10.1103/PhysRevLett.108.165006.

[134] D. Del Sorbo, D. R. Blackman, R. Capdessus, K. Small, C. Slade-Lowther, W. Luo, M. J. Duff, A. P. L. Robinson, P. McKenna, Z. M. Sheng, J. Pasley, and C. P. Ridgers. Efficient ion acceleration and dense electron-positron plasma creation in ultra-high intensity laser-solid interactions. *arXiv*, 1706(04153):1–5, 2017. URL http://arxiv.org/abs/1706.04153.

[135] M. J. Duff, R. Capdessus, D. Del Sorbo, C. P. Ridgers, M. King, and P. McKenna. Modelling the effects of the radiation reaction force on the interaction of thin foils with ultra-intense laser fields. *Plasma Physics and Controlled Fusion*, 60 (6):064006, jun 2018. ISSN 0741-3335. doi: 10.1088/1361-6587/aab97d. URL https://iopscience.iop.org/article/10.1088/1361-6587/aab97d.

[136] H. Y. Wang, X. Q. Yan, and M. Zepf. Signatures of quantum radiation reaction in laser-electron-beam collisions. *Physics of Plasmas*, 22(9):093103, sep 2015. ISSN 1070-664X. doi: 10.1063/1.4929851. URL http://dx.doi.org/10.1063/1.4929851http://aip.scitation.org/doi/10.1063/1.4929851.

[137] S. K. Barber, J. van Tilborg, C. B. Schroeder, R. Lehe, H.-E. Tsai, K. K. Swanson, S. Steinke, K. Nakamura, C. G. R. Geddes, C. Benedetti, E. Esarey, and W. P. Leemans. Measured Emittance Dependence on the Injection Method in Laser Plasma Accelerators. *Physical Review Letters*, 119(10):104801, sep 2017. ISSN 0031-9007. doi: 10.1103/PhysRevLett.119.104801. URL https://link.aps.org/doi/10.1103/PhysRevLett.119.104801.

[138] C. Thaury, E. Guillaume, A. Lifschitz, K. Ta Phuoc, M. Hansson, G. Grittani, J. Gautier, J.-P. Goddet, A. Tafzi, O. Lundh, and V. Malka. Shock assisted ionization injection in laser-plasma accelerators. *Scientific Reports*, 5(1):16310, dec 2015. ISSN 2045-2322. doi: 10.1038/srep16310. URL http://www.nature.com/articles/srep16310.

[139] M. Mirzaie, S. Li, M. Zeng, N. A. M. Hafz, M. Chen, G. Y. Li, Q. J. Zhu, H. Liao, T. Sokollik, F. Liu, Y. Y. Ma, L. M. Chen, Z. M. Sheng, and J. Zhang. Demonstration of self-truncated ionization injection for GeV electron beams. *Scientific Reports*, 5(14659):1–9, 2015. doi: 10.1038/srep14659.

[140] T. G. Blackburn, C. P. Ridgers, J. G. Kirk, and A. R. Bell. Quantum radiation reaction in laser-electron-beam collisions. *Physical Review Letters*, 112:015001, 2014. ISSN 00319007. doi: 10.1103/PhysRevLett.112.015001.

[141] C. P. Ridgers, T. G. Blackburn, D. Del Sorbo, L. E. Bradley, C. D. Baird, S. P. D. Mangles, P. Mckenna, M. Marklund, C. D. Murphy, and A. G. R. Thomas. Signatures of quantum effects on radiation reaction in laser – electron-beam collisions. *arXiv:1708.04511*, pages 1–14, 2017.

[142] C. Arran, J. M. Cole, E. Gerstmayr, T. G. Blackburn, S. P. D. Mangles, and C. P. Ridgers. Optimal Parameters for Radiation Reaction Experiments. *arXiv*, 2019. ISSN 23318422.

[143] A. J. W. Reitsma and D. A. Jaroszynski. Coupling of longitudinal and transverse motion of accelerated electrons in laser wakefield acceleration. *Laser and Particle Beams*, 22:407–413, 2004.

[144] A. G. R. Thomas. Scalings for radiation from plasma bubbles. *Physics of Plasmas*, 17:056708, 2010. doi: 10.1063/1.3368678.

[145] C. Yeboaha. Characterization of linear accelerator X-ray source size using a laminated beam-spot camera. *Journal of Applied Clinical Medical Physics*, 12 (3):178–182, 2011. ISSN 15269914. doi: 10.1120/jacmp.v12i3.3463.

[146] S. Kiselev, A. Pukhov, and I. Kostyukov. X-ray generation in strongly nonlinear plasma waves. *Physical Review Letters*, 93(13):135004, sep 2004. ISSN 0031-9007. doi: 10.1103/PhysRevLett.93.135004. URL https://link.aps.org/doi/10.1103/PhysRevLett.93.135004.

[147] A. Rousse, K. Ta Phuoc, R. Shah, A. Pukhov, E. Lefebvre, V. Malka, S. Kiselev, F. Burgy, J.-P. Rousseau, D. Umstadter, and D. Hulin. Production of a keV X-ray beam from synchrotron radiation in relativistic laser-plasma interaction. *Physical Review Letters*, 93(13):1–4, 2004. ISSN 00319007. doi: 10.1103/PhysRevLett.93.135005.

[148] J. M. Cole, J. C. Wood, N. C. Lopes, K. Poder, R. L. Abel, S. Alatabi, J. S.J. Bryant, A. Jin, S. Kneip, K. Mecseki, D. R. Symes, S. P.D. Mangles, and Z. Najmudin. Laser-wakefield accelerators as hard x-ray sources for 3D medical imaging of human bone. *Scientific Reports*, 5:1–7, 2015. ISSN 20452322. doi: 10.1038/srep13244. URL http://dx.doi.org/10.1038/srep13244.

[149] G. Sarri, D. J. Corvan, W. Schumaker, J. M. Cole, A. Di Piazza, H. Ahmed, C. Harvey, C. H. Keitel, K. Krushelnick, S. P. D. Mangles, Z. Najmudin, D. Symes, A. G. R. Thomas, M. Yeung, Z. Zhao, and M. Zepf. Ultrahigh brilliance multi-MeV ??-ray beams from nonlinear relativistic thomson scattering. *Physical Review Letters*, 113(22):224801, 2014. ISSN 10797114. doi: 10.1103/PhysRevLett.113.224801.

[150] E. Esarey and P. Sprangle. Nonlinear Thomson Scattering of Intense Laser Pulses from Beams and Plasmas. *Physical Review E*, 48(4), 1993.

[151] S. Chen, A. Maksimchuk, and D. Umstadter. Experimental Observation of Relativistic Nonlinear Thomson Scattering. *Nature*, 396(December):653–655, 1998.

[152] O. J. Finlay, M. J. V. Streeter, A. G. R. Thomas, D. Symes, R. Allott, C. D. Armstrong, N. Bourgeois, C. Brenner, C. Gregory, Y. Katzir, D. Neely, R. Pattathil, D. Rusby, C. Thornton, S. Cipiccia, J. M. Cole, J. Gruse, N. C. Lopes,

S. P. D. Mangles, Z. Najmudin, J. C. Wood, C. D. Baird, C. D. Murphy, C. I. D. Underwood, L. R. Pickard, and K. D. Potter. Characterisation of a Laser Plasma Betatron Source for High Resolution X-ray Imaging. *CLF Annual Report*, pages 1–6, 2018.

[153] M. Thoms. The quantum efficiency of radiographic imaging with image plates. *Nuclear Instruments and Methods in Physics Research Section A: Accelerators, Spectrometers, Detectors and Associated Equipment*, 378(3):598–611, aug 1996. ISSN 01689002. doi: 10.1016/0168-9002(96)00530-X. URL https://linkinghub.elsevier.com/retrieve/pii/016890029600530X.

[154] P. A. Norreys, M. Santala, E. Clark, M. Zepf, I. Watts, F. N. Beg, K. Krushelnick, M. Tatarakis, A. E. Dangor, X. Fang, P. Graham, T. McCanny, R. P. Singhal, K. W. D. Ledingham, A. Creswell, D. C. W. Sanderson, J. Magill, A. Machacek, J. S. Wark, R. Allott, B. Kennedy, and D. Neely. Observation of a highly directional γ-ray beam from ultrashort, ultraintense laser pulse interactions with solids. *Physics of Plasmas*, 6(5):2150–2156, may 1999. ISSN 1070-664X. doi: 10.1063/1.873466. URL http://aip.scitation.org/doi/10.1063/1.873466.

[155] Z. M. Sheng, Y. Sentoku, K. Mima, J. Zhang, W. Yu, and J. Meyer-ter Vehn. Angular Distributions of Fast Electrons, Ions, and Bremsstrahlung x/ γ -Rays in Intense Laser Interaction with Solid Targets. *Physical Review Letters*, 85(25): 5340–5343, dec 2000. ISSN 0031-9007. doi: 10.1103/PhysRevLett.85.5340. URL https://link.aps.org/doi/10.1103/PhysRevLett.85.5340.

[156] S. Bastiani, A. Rousse, J. P. Geindre, P. Audebert, C. Quoix, G. Hamoniaux, A. Antonetti, and J. C. Gauthier. Experimental study of the interaction of subpicosecond laser pulses with solid targets of varying initial scale lengths. *Physical Review E - Statistical Physics, Plasmas, Fluids, and Related Interdisciplinary Topics*, 56(6):7179–7185, 1997. ISSN 1063651X. doi: 10.1103/PhysRevE.56.7179.

[157] J. Jarrett, M. King, R. J. Gray, N. Neumann, L. Döhl, C. D. Baird, T. Ebert, M. Hesse, A. Tebartz, D. R. Rusby, N. C. Woolsey, D. Neely, M. Roth, and P. McKenna. Reflection of intense laser light from microstructured targets as a

potential diagnostic of laser focus and plasma temperature. *High Power Laser Science and Engineering*, 7:1–7, 2019. ISSN 2095-4719. doi: 10.1017/hpl.2018.63.

[158] T. Ebert, N. W. Neumann, L. N. K. Döhl, J. Jarrett, C. D. Baird, R. Heathcote, M. Hesse, A. Hughes, P. McKenna, D. Neely, D. Rusby, G. Schaumann, C. Spindloe, A. Tebartz, N. Woolsey, and M. Roth. Enhanced brightness of a laser-driven x-ray and particle source by microstructured surfaces of silicon targets. *Physics of Plasmas*, 27(4):043106, apr 2020. ISSN 1070-664X. doi: 10.1063/1.5125775. URL http://aip.scitation.org/doi/10.1063/1.5125775.

[159] A. P. L. Robinson, H. Schmitz, J. S. Green, C. P. Ridgers, and N. Booth. Guiding of laser-generated fast electrons by exploiting the resistivity-gradients around a conical guide element. *Plasma Physics and Controlled Fusion*, 57(6), 2015. ISSN 13616587. doi: 10.1088/0741-3335/57/6/064004.

[160] A. J. Kemp, F. Fiuza, A. Debayle, T. Johzaki, W. B. Mori, P. K. Patel, Y. Sentoku, and L. O. Silva. Laser-plasma interactions for fast ignition. *Nuclear Fusion*, 54(5), 2014. ISSN 17414326. doi: 10.1088/0029-5515/54/5/054002.

[161] A. P. L. Robinson, D. J. Strozzi, J. R. Davies, L. Gremillet, J. J. Honrubia, T. Johzaki, R. J. Kingham, M. Sherlock, and A. A. Solodov. Theory of fast electron transport for fast ignition. *Nuclear Fusion*, 54(5), 2014. ISSN 17414326. doi: 10.1088/0029-5515/54/5/054003.

[162] V. B. Mikhailik, V. Kapustyanyk, V. Tsybulskyi, V. Rudyk, and H. Kraus. Luminescence and scintillation properties of CsI: A potential cryogenic scintillator. *Physica Status Solidi (b)*, 252(4):804–810, apr 2015. ISSN 03701972. doi: 10.1002/pssb.201451464. URL http://doi.wiley.com/10.1002/pssb.201451464.

[163] T. G. Blackburn, D. Seipt, S. S. Bulanov, and M. Marklund. Radiation beaming in the quantum regime. *Physical Review A*, 101(1):1–8, 2020. ISSN 24699934. doi: 10.1103/PhysRevA.101.012505.